UTILIZING SWITCHED LINEAR DYNAMICS OF INTERCONNECTED STATE TRANSITION DEVICES FOR APPROXIMATING CERTAIN GLOBAL FUNCTIONS

A Dissertation
Presented to
The Academic Faculty

By

ABHINAV PARIHAR

In Partial Fulfillment
of the Requirements for the Degree
Doctor of Philosophy in the
School of Electrical and Computer Engineering

Georgia Institute of Technology

May 2020

UTILIZING SWITCHED LINEAR DYNAMICS OF INTERCONNECTED STATE TRANSITION DEVICES FOR APPROXIMATING CERTAIN GLOBAL FUNCTIONS

Approved by:

Dr. Arijit Raychowdhury (Advisor)
School of Electrical and Computer Engineering
Georgia Institute of Technology

Dr. Justin Romberg
School of Electrical and Computer Engineering
Georgia Institute of Technology

Dr. Saibal Mukhopadhyay
School of Electrical and Computer Engineering
Georgia Institute of Technology

Dr. Magnus Egerstedt
School of Electrical and Computer Engineering
Georgia Institute of Technology

Dr. Suman Datta
Department of Electrical Engineering
University of Notre Dame

TABLE OF CONTENTS

LIST OF TABLES

LIST OF FIGURES

Chapter 1

INTRODUCTION AND MOTIVATION

Thinking is the most complex phenomenon known to man. We have tried for centuries to understand brain as a complex machine and thinking as a natural phenomenon which follows the laws of nature. The process of understanding, by synthesis, led to the creation of computer, albeit for other useful purposes. Yet, today's computing systems are hardly a match for the kind of information processing we can imagine. In fact, on many fronts, these systems are not adequate even for our present needs. Neither can they predict tornados, nor can they replace a broken limb. The challenge resides not only in engineering such systems, but also in the conceptual understanding behind their design. On the contrary, many computing-like phenomena found in nature, for example rythmic flashing of fireflies, or pattern formation in microbial systems, show processing of hard problems in a very easy and efficient manner. As such, it raises the question whether the problems themselves are hard or is it the style of computing that makes them hard, and whether other alternative computing systems can be designed which are more efficient in solving such systems.

1.1 ANATOMY OF A COMPUTING MACHINE

A *computing operation* involves transformation of information from a given, less useful, input form to another desired output form which is more useful. A *computing machine* is capable of performing a computing transformation by itself, i.e. the transformation results merely from the physics of its constitution without any external entity governing the process. As such, any computing process in a computing machine would essentially be a dynamical system governed by the physical processes in the machine. The current standard paradigm of computing is the *Turing machine* model and the *Von Neumann architecture*. In the Turing machine model, every computing operation is broken down into basic binary

arithmetic operations. And *Von Neumann* architecture dictates an implementation of such a system with a separate memory block, and a processor that stores and fetches data from the memory and performs binary arithmetic. The tremendous success of this paradigm is partly due to its universal nature, and partly due to the ease of implementing binary logic in CMOS. Yet, these systems prove inadequate in solving hard problems like combinatorial optimization. Possible reasons include separation of memory and processing, and redundant enforced accuracy and storage at each step. In fact, it can be argued that many of these hard problems are not suited to be solved in terms of discrete arithmetic operations, but instead in terms of continuous representations and dynamics which are not easily calculated using conventional array representations in the digital symbolic metaphor.

1.2 AVENUES OF IMPROVEMENT

This perspective of the anatomy of a computing system highlights many possible avenues for improvements. In order to build dedicated hardware accelerators for special operations, a universal model of computation like the Turing machine is not needed. Also, new technologies and the physics of devices can enable emulation of many other basic operations and functions that are not mere binary logic operations. This has been the premise of analog computation from the beginning [1], but its computational power has always been compared to the Turing machine model in the light of "absolute" results equating the computational power of Turing machine with any analog computer that can be built [2]. Although such results about Turing machine and its universality are some of most important results in computer science, these are disconnected from the real world implementation where the costs involved can come from architectural choices as well. A much better problem specific computing system is possible if an alternative computing model is complemented with the continuous time dynamics, deterministic or stochastic, of new *beyond CMOS devices*. These *beyond CMOS devices* are new devices being researched which have different characteristics than the transistors used in conventional semiconduc-

tor chips. But these efforts face a common challenge - lack of good computational models which can support the dynamical systems of these new interconnected devices. As such, these new devices end up aiming for the same old goals of better switches and compact logical operations that had formed the basis of Turing machine paradigm. The possibility that physical devices can offer more computing abilities than just switches or logic gates has been either less explored or challenging. The work described in this thesis lies at this intersection of design, modeling and architectures to create novel computing systems that use the continuous time dynamics of interacting devices to solve hard computing problems.

1.3 OBJECTIVE OF PROPOSED RESEARCH

The objective of the proposed research is to create alternative computing models and architectures, unlike (discrete) sequential Turing machine/Von Neumann style models, which utilize the network dynamics of interconnected IMT (insulator-metal transition) devices. This work focusses on circuits (mainly coupled oscillators) and the resulting switched linear dynamical systems that arise in networks of IMT devices. Electrical characteristics of the devices and their stochasticity are modeled mathematically and used to explain experimentally observed behavior. For certain kinds of connectivity patterns, the steady state limit cycles of these systems encode approximate solutions to global functions like dominant eigenvector of the connectivity matrix and graph coloring of the connectivity graph.

Chapter 2

LITERATURE SURVEY

Even with the tremendous success of digital Von Neumann architecture, researchers have always been interested in other kinds of *analog* computing systems where the dynamics of the system computes by itself in continuous time. Many of these are inspired by computing that occur in nature with different computing entites interacting with each other, for example, coupled oscillators, neural networks etc.

2.1 TECHNOLOGIES FOR CONTINUOUS TIME DYNAMICAL SYSTEMS

At the fundamental level, compute technologies have used and manipulated the charge, spin, or quantum properties of electrons, or used photons. Important technologies include spin-torque [3–6], insulator-metal-transition [7], optical [5, 8] and quantum [9]. CMOS (Complementary metal oxide semiconductor) technology based on charge has driven most of the digital computing machinery by implementing logic gates. Currently, there has been a lot of emphasis on technologies other than CMOS called *beyond-CMOS* techonlogies. Major reasons for not prefering CMOS based continuous time dynamical systems for computing are:

1. CMOS processes introduce non-linearities when dealing with large signal dynamics which is usually the case for continuous time dynamical systems. This makes it hard to create circuits with predictable dynamics which can be used for computing.

2. Small signal model based traditional analog circuits could be used for linearity but such circuits involve high biasing currents resulting in high power consumption.

3. Size of basic components like oscillators built using CMOS technology are much larger which reduces the density of large arrays of such oscillators.

2.2 COUPLED OSCILLATORS

2.2.1 *Theory*

Coupled oscillator models can explain many natural, chemical and biological synchronization phenomena like the synchronized flashing of fireflies, pacemaker cells in the human heart, chemical oscillations, neural oscillations, and laser arrays, to name a few [10]. The simplest theoretical models of oscillators start with sinusoidal oscillators which have been extensively studied [11–13] and their application in the computational paradigm has been well demonstrated [14, 15]. A generalized description of oscillators in these models is usually a canonical phase model [10, 16], and the coupling mechanisms are generally assumed weak and composed of simple periodic functions which explicitly depend on phases. In this model the oscillators are simple harmonic and their coupling is assumed to affect each other's phases linearly. If the oscillators with phases θ_1 and θ_2 have frequencies ω_1 and ω_2 then in Kuramoto models the coupling of two oscillators will result in the phase equations:

$$\dot{\theta}_1 = \omega_1 + k(\theta_1 - \theta_2)$$
$$\dot{\theta}_2 = \omega_2 + k(\theta_2 - \theta_1)$$

where k is the coupling constant. A *Kuramoto* system of N oscillators is described by

$$\dot{\theta}_i = \dot{\omega}_i + \frac{K}{N}\sum_{j=1}^{N}\sin(\theta_j - \theta_i) \qquad i = 1, ..., N$$

where θ_i and ω_i are the phase and frequency respectively of i^{th} oscillator. Several studies on more general periodic coupling functions have also been studied [17].

Along with sinusoidal oscillators, non-linear Van-der-Pol oscillators [18] and several of its variants, like the Morris-lecar neuron model [19], have also been studied and the applicability of such models in neurobiological and chemical oscillators have been demonstrated

[20–22]. A single van-der-pol oscillator is defined by adding a non-linearity in the simple harmonic oscillator model

$$u'' + \varepsilon(u^2 - 1)u' + u = 0$$

which results in relaxation behavior and hence it is also called *relaxation* type oscillators. But these analysis also assume non-realistic coupling dynamics like weak or pulse coupling and do not focus on engineering aspects of building such coupled oscillators.

Such analytic models of coupled oscillatory systems almost always require a canonical phase description of the oscillators and a periodic phase dependent additive coupling that can be classified as weak. Strong coupling for relaxation type oscillators built using electrical circuits lack good explanations. Some theoretical studies have focussed on pulse coupling [23–25], and injection locking [26, 27] but these are not suitable for understanding coupled relaxation oscillators of the kind focussed in this thesis.

Another kind of two coupled oscillator study was done in [28] which involved the usual relaxation type oscillators [29] which work on charging and discharging of a capacitor. As such, these oscillators show piecewise linear dynamics instead of continuous dynamics as in the previous models and the analysis of coupling is rather difficult as the limit cycle spans different "pieces" of the dynamics.

2.2.2 *Implementation*

It has been always been challenging to create compact as well as low power oscillators. But more challenging is the coupling of such oscillators to give predictable phase or frequency dynamics. Basic oscillators in CMOS technology include logical oscillators, which are square wave oscillators consisting of a chain of odd number of inverters, and LC oscillators which are sinusoidal harmonic oscillators LC components in the loop.

Non-silicon electrical oscillators include two important kinds which are currently being developed. One prominent effort is the use of spin torque oscillators (STOs) coupled with using spin diffusion currents, or electrical signals, for providing a computational platform

Table 2.1: Comparison of different electrical oscillator technologies with VO_2 based oscillators used in this work

	This Work	TaO_x [41]	HfTaOx and $GeTe_6$ [42]	PLL [43]
Power (μW)	12	< 100	< 50	< 700
Area (μm^2)	0.89	0.5	0.5	-
Max Freq. (MHz)	9	500	350	< 10

for machine learning, spiking neural networks, and others [3–6, 30–32]. However, the high current densities of STOs and the limited range of spin diffusion currents continue to pose serious challenges in created coupled networks of such oscillators. Optical oscillators have been studied [8, 33] and used for computing [5], but challenges include bulky components, difficult interfacing between electrical and optical mediums and lack of programmability for any optical computing apparatus. Another promising non-silicon technology for very compact oscillators is the IMT (insulator-metal transition) material based oscillator technology [34, 35] which is the focus in this work. As the oscillation mechanism is completely electrical, the coupling of oscillators can be done easily using electrical components. There have been other implementation efforts for elecrical oscillators [36–40] but the focus has been to build high frequency and low power individual oscillators but not to build coupled systems or to generate interesting dynamics for computing. The oscillators used in this work are based on IMT (insulator-metal-transition) devices built using Vanadium Dioxide (VO_2). A comparison of some other computing focussed oscillators with the VO_2 based oscillators is shown in Table 2.1:

2.2.3 *Computing models*

Coupled oscillator associative memories [15, 44, 45] have been proposed which have been shown to be equivalent to the Hopfield model of associative memories, but successful implementations have yet to come. Another application can be graph coloring [46, 47], but its understanding has been limited to two colorable graphs. An interesting Ising Machine

implementation using Optical Parametric Oscillators (OPO) was shown in [5].

2.3 OTHER DYNAMICAL SYSTEMS FOR COMPUTING

Apart from coupled oscillators, other dynamical system models have been studied for various applications, but few have been implemented in some kind of hardware with proven advantages over corresponding digital implementations of algorithms. Hopfield networks are attractor networks proposed for associative memories [48] where the fixed points (or stable states) of the system correspond to memories and the dynamics of the network is such that the system settles to the fixed point which is closest to the initial state the system starts from. Hopfield style models have also been used for optimization [49]. Cellular neural networks [50] consist of interconnected nodes where each node has linear or non-linear dynamics and the connections specify the coupling between their corresponding differential equations. Their CMOS implementations have been proposed with applications like pattern matching. Ising Machine [5, 51, 52] models have been proposed based on coupled spin glasses. The energy minima of such networks correspond to the solutions of an NP-hard combinatorial optimization problem, and hence can model other NP-hard problems as well [51]. Another dynamical system for constraint satisfaction [53] is built on similar principles. An architecture based on non-repeating phase relations [54] between fabricated CMOS oscillators tries to emulate stochastic local search (SLS) for constraint satisfaction problems. An interesting approach based on "memory co-processors" was introduced as Memcomputing in [55]. Interesting insights can be obtained by looking into dynamical systems like iterated maps [56], cellular automata [57–59], and 0-1 continuous reformulations of discrete optimization problems [60].

Chapter 3

DEVICES, CIRCUITS AND OSCILLATIONS

3.1 BACKGROUND

3.1.1 *Kinds of oscillators*

Not all circuits oscillate and show periodic behavior. For oscillations, a very special kind of instability is required. Coupled with the fact that with the kind of "simple" electrical components available, only certain kinds of electrical behavior can be realized in practice. Here, "simple" components refer to those components which have locally linear relationships between charge, current and voltages. The components assumed in the following characterization include the passive components - resistance, capacitance, and inductance, as well as another component - **a hysteretic resistance**. A hysteretic resistor is a two terminal resistance, but changes between two resistance states - a metallic and an insulating state. The state switches to metallic when the applied voltage exceeds a higher threshold v_h. The state switches to insulating state when the applied voltage goes below a lower threshold v_l. There is hysteresis in switching, which means that $v_h \neq v_l$. When the applied voltage is between v_h and v_l the current resistance state is retained. The transition between metallic and insulatng states is very abrupt/instantaneous. In physical reality, such devices are usually accompanied with some capacitance, but no inductance. This means that the current switches abruptly during the transitions but the voltage avoids any abrupt change.

Using these components, 4 kinds of oscillators have been studied in literature. These oscillator models are not completely distinct and have some well-defined relationships among them. These models are:

1. **Harmonic oscillators:** Also called sinusoidal oscillators, their waveforms are sinusoidal and can be created using an inductance and capacitance in a loop. Harmonic

oscillations have a simple, but second order, diferential equation -

$$x''(t) = -kx$$

whose solutions are sinusoidal functions, which is why they are also called sinusoidal oscillators.

2. **Van der pol oscillators:** These are a variation of the harmonic oscillators but with an added non-linearity, also called damping, and were used to describe oscillations in early circuits involving vaccuum-tubes. The basic form of such oscillators is:

$$x''(t) = \mu(1 - x^2) - kx$$

These are also called relaxation oscillators as an oscillation cycle shows two stages which involve charging and discharging of some capacitive element.

3. **Hysteresis based:** Oscillations in these kinds arise by connecting just a hysteretic resistance in series with a linear resistance, where the hysteresis resistance is accompanied with a parallel capacitor across it. The oscillations arise due to a lack of a stable point. The oscillations are relaxation oscillations where a capacitance is being charged or discharged in the two states of the hysteretic resistance. This study focuses on this particular kind of oscillators.

4. **Spiking Neurons:** Another kind of commonly discussed oscillators are spiking neurons, which are essentially oscillators but with a bifurcation - the bifurcation being between oscillating behavior and a constant behavior (stable fixed point). There are 3 common spiking neuron models, which are successive aproximations of the previous one:

   (a) Hodgkin Huxley (HH) model - 4 dimensional

(b) Fitz-Hugh-Nagumo (FHN) model - 2 dimensional

(c) Integrate and Fire (I&F) model - piece-wise 1 dimensional

3.1.2 *Oscillator implementations*

Oscillators can be implemented in CMOS technologies. Examples include LC oscillators which use an inductance and a capacitance to create harmonic oscillations. Problems with such CMOS oscillators include difficulties integrating large inductances on chip. Without the inductance, it becomes difficult to realize a second order differential equation, and hence harmonic oscillations, in a circuit. As such, from a hardware implementation perspective, it is important to consider oscillators which do not use inductances, and as such are non-harmonic.

This is where hysteresis based oscillators have an advantage. Also, it turns out that not only do hysteresis based oscillators can be very compact, they also have desirable properties of coupling with other oscillators - the coupling is easy to implement, and the coupling has linear characteristics which is easy to analyse.

The reason why oscillator implementations have started involving non-CMOS devices is because the implementation of oscillators using traditional CMOS technologies either consume more resources or have a behavior which is not suitable for the applications they are intended for. Different kinds of device technologies have been used for realizing different kinds of oscillator hardware.

3.2 THIS STUDY

3.2.1 *State-Transition devices*

This study focusses on the hysteresis + R kind of oscillators, and was done in collaboration with a group working on an implementation of such oscillators, specifically the hysteretic resistance. But as a result of this analysis, certain relationships also emerged between the

hysteresis + R kind, and the other kinds of oscillators. The implementation of the hysteretic resistance is based on Vanadium-Dioxide (VO_2) based thin-film devices, called insulator-metal-transition (IMT) devices, or phase-change devices, and the state switching occurs under the application of heat or an electric field [61]. Interestingly, some other efforts to create new kinds of post-CMOS devices also resulted in devices with similar hysteretic resistance behavior like , and the analysis for IMT devices can be extended easily to these other devices. As such, these devices will all be collectively referred to as **State-Transition (ST)** devices. A State-Transition device is defined as a two-terminal device which behaves as a resistance at a given point in time, but switches between two resistance states. The state transition of the device has following characteristics:

1. Only the resistance of the device changes with its state; and the resistance is linear;

2. A state transition is triggered by the voltage across the device. This triggering can be electric field driven or thermally driven, and can be modeled as an equivalent triggering voltage [62]. When the voltage exceeds a higher threshold v_h, the state changes to a metallic (low resistance) state and when the voltage exceeds a lower threshold v_l, the state switches back to the insulating (high resistance) state. The thresholds v_h and v_l are not equal, i.e. there is hysteresis in the switching with $v_l < v_h$.

3. A capacitance is associated with the device that ensures gradual build up and decaying of the voltage (and hence energy) across the device.

3.2.2 *Oscillator Circuits*

We will consider two kinds of relaxation oscillator circuits using such state-changing devices - (a) two state-changing devices in series (3.1). We will refer to this configuration as D-D. And (b) a state changing device in series with a resistance (3.2)[63]. This configuration will be referred to as D-R. The D-D configuration is enticing in its simplicity, both in physical realization and analysis as will be evident in the following sections. The

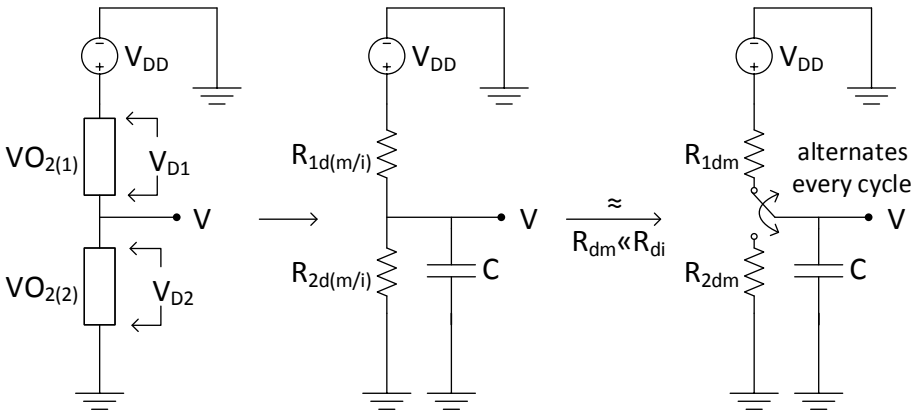

Figure 3.1: Relaxation oscillator circuit realized using two IMT state-changing devices in series (D-D configuration), and its circuit equivalent with R_{dm} and R_{di} as the internal resistance of the IMT devices in metallic and insulating states respectively. When $R_{di} \gg R_{dm}$ the device behaves as a parallel combination of a capacitor and a resistor with a switch.

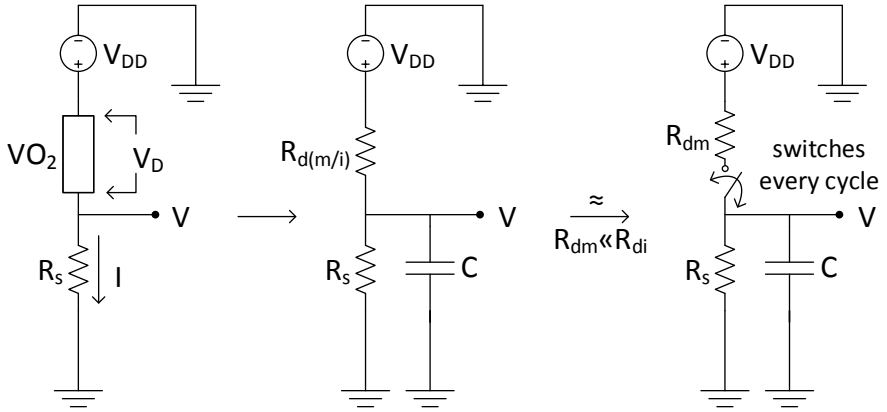

Figure 3.2: Relaxation oscillator circuit realized with a IMT device in series with a resistor (D-R configuration), and its circuit equivalent with R_{dm} and R_{di} as the internal resistance of the IMT device in metallic and insulating states respectively. When $R_{di} \gg R_{dm}$ the device behaves as a parallel combination of a capacitor and a resistor with a switch.

D-R configuration, on the other hand, has been experimentally demonstrated[63] and can be thought of as an extension of the D-D configuration albeit with more complex dynamics of synchronization.

This study of the synchronization dynamics of such coupled systems, although inspired by the experimental realization of VO_2 based oscillators, is not limited to these oscillators only, but encompasses a class of similar pairwise-coupled relaxation oscillators as well. The circuit equivalents of D-D and D-R relaxation oscillators are shown in figures 3.1 and 3.2 respectively. The internal resistance of the device R_d has two different values in the two states of the device - R_{di} in the insulating (high resistance) state and R_{dm} in the metallic (low resistance) state. C is the internal capacitance of the IMT device (including any parasitic capacitances) and R_S is the series resistance. We will also assume that $R_{di} \gg R_{dm}$. In the D-D configuration, the capacitor being charged can be represented as a single capacitor at the output circuit node. The coupling circuit is a parallel combination of a capacitor C_c and a resistor R_c. As shown, the output node of the oscillator is between the device and the resistance, and the coupling circuit is connected between these output nodes[63].

3.2.3 *Modeling*

Let us establish the system model and the system of ODEs that define the system. This will allow us to define the conditions for oscillation as well as the coupling dynamics. We will first consider D-D configuration and then D-R configuration as an extension of the D-D configuration. The D-D configuration, owing to its inherent symmetry renders to easier dynamics and analysis and provides valuable insights into the system.

3.2.3.1 *D-D configuration*

The circuit equivalent for a D-D type relaxation oscillator is shown in 3.1. For simplicity, all voltages are normalized to v_{dd} (including v_l and v_h). We define conductances $g_{di} = R_{di}^{-1}$, $g_{dm} = R_{dm}^{-1}$ and $g_c = R_C^{-1}$. For the conductances, subscript d denotes a state dependent

device conductance and m/i denotes metallic/insulating state respectively. The subscripts preceding dm or di refer to the corresponding numbered device as shown in figure. Also, it is assumed that $g_{dm} \gg g_{di}$, which means that the g_{di} state essentially disconnects the circuit. This implies that the effective charging happens through g_{1dm} and effective discharging through g_{2dm}. The single D-D oscillator can be described by the following set of piecewise linear differential equations:

$$cv' = \begin{cases} (v_{dd} - v)g_{1dm} & charging \\ -v\,g_{2dm} & discharging \end{cases} \tag{3.1}$$

where c is the lumped capacitance of both devices along with the parasitics. The equation can be re-written as:

$$cv' = -g(s)v + p(s) \tag{3.2}$$

where s denotes the conduction state of the device (0 for metallic, and 1 for insulating) and $g(s)$ and $p(s)$ depend on the device conduction state s as follows:

$$g(s) = \begin{cases} g_{1dm}, & s = charging \\ g_{2dm}, & s = discharging \end{cases} \tag{3.3}$$

$$p(s) = \begin{cases} g_{1dm}, & s = charging \\ 0, & s = discharging \end{cases} \tag{3.4}$$

3.2.3.2 *D-R configuration*

The equivalent circuit for a D-R type relaxation oscillator is shown in figure 3.2. As in the case of D-D configuration, voltages are normalized to v_{dd}. The conductances involved are $g_{di} = R_{di}^{-1}$, $g_{dm} = R_{dm}^{-1}$, $g_s = R_s^{-1}$ and $g_c = R_C^{-1}$. Effective charging happens through g_{dm} as in the previous case but there is an added leakage through g_s, whereas effective discharging

happens only through g_s. Following the same methodology as in the D-D case, the equation for the single D-D oscillator dynamics can be written as:

$$cv' = \begin{cases} (v_{dd} - v)g_{dm} - v\,g_s & charging \\ -v\,g_s & discharging \end{cases} \tag{3.5}$$

which can be re-written as:

$$cv' = -g(s)v + p(s) \tag{3.6}$$

where,

$$g(s) = \begin{cases} g_{dm} + g_s, & s = charging \\ g_s, & s = discharging \end{cases} \tag{3.7}$$

$$p(s) = \begin{cases} g_{dm}, & s = charging \\ 0, & s = discharging \end{cases} \tag{3.8}$$

and s denotes the conduction state of the system as before.

3.2.3.3 *D-MOSFET configuration*

One variation of a D-R configuration is when the series resistor is replaced by a mosfet. The idea is to be able to control the effective resistance of the series element using a voltage signal, so as to control the properties of oscillations, and also to be able to switch them on or off. The MOSFET is assumed to operate in its saturation region and is modeled using a voltage controlled current source and an output impedence. As before, the transition voltages for changing the state of the device from insulating to metallic and vice versa correspond to voltages v_l and v_h respectively at the output node. Let the following parameters be defined for the series transistor: g_m – trans-conductance of series transistor, g_0 – output

conductance of series transistor. For simplicity, all voltages in the system are normalized to $v_{\rm dd}$ (including v_l, v_h and $v_{\rm gs}$ applied at the transistor gates); hence, $v_{\rm dd} = 1$. When $g_{\rm di} \ll g_0$ and $g_{\rm dm} \gg g_0$, the equation for the system can be simplified to:

$$cv^{'} = -g(s)\,v + p(s)$$

where s denotes the phase of the device (metallic, or insulating) and $g(s)$ and $p(s)$ depend on the device phase s as follows:

$$g(s) = \begin{cases} g_{dm}, & s = metallic \\ g_0, & s = insulating \end{cases} \tag{3.9}$$

$$p(s) = \begin{cases} g_{dm}, & s = metallic \\ -g_m v_{gs}, & s = insulating \end{cases} \tag{3.10}$$

3.2.4 *Phase space, flows and oscillation conditions*

A series arrangement of two IMT devices (D-D), or an IMT device and a resistor (D-R) will oscillate only when certain conditions are met. In case of two devices in series (D-D), the two devices must be in opposite conduction states (one metallic and the other insulating) all the time for oscillations to occur. If the threshold voltages v_l and v_h are same for the devices and the following condition holds

$$v_l + v_h = V_{DD} \tag{3.11}$$

and at $t = 0$ the devices are in different conduction states, then any time one device switches, the other will make the opposite transition as well. The basic mechanism of oscillations is as follows. The device in metallic state connects the circuit and charges (discharges)

the output capacitor, and the other device in insulating state does not participate in the dynamics. As the capacitor charges, the voltage drop across the device in metallic state decreases and crosses the lower threshold v_l. At the same instant, the voltage drop across the other device in insulating state increases and crosses the higher threshold v_h because $v_{D1} + v_{D2} = V_{DD}$. The devices then switch states and the cycle continues. The devices can be conceived as a switch which is open in insulating state (ignoring any leakage in the insulating state) and closed in metallic state (figure 3.1). If v_l and v_h deviate from (3.11), the devices will not switch at the same instant and oscillations will stop as the system settles to a stable point where both devices are in same state and the voltage of the output nodes remains at $V_{DD}/2$. This may require additional startup circuit in the system, which is trivial to integrate.

In D-R configuration, another set of conditions have to be met [64] which depend on the relative values of the device resistances in the two states (R_{dm} and R_{di}) and the series resistance (R_S). These conditions can be described using the phase diagram of the IMT device (figure 3.3). Lines with slopes r_i and r_m are the regions of operation of the device in insulating and metallic states respectively. The intersection of these lines with the load line due to the series resistance gives the stable points of the system in the two states. For self-sustained oscillations, the stable points in each state should lie outside the region of operation, i.e. outside the region defined by horizontal lines passing through the transition points. This ensures that the system always tries to reach the stable point in the current state but is always preceded by a transition to the other state. This moves the system towards the stable point of the other state (away from the previous stable point) and hence the system never reaches any stable point and oscillates. This configuration is robust towards deviation of v_l and v_h from condition (3.11) and as only one device is involved, it does not require the difficult constraint of simultaneous switching of devices as was in the D-D case. This reduced requirement of symmetry is an attractive property of the D-R configuration as initial experiments have confirmed sustained oscillations in this configuration[63].

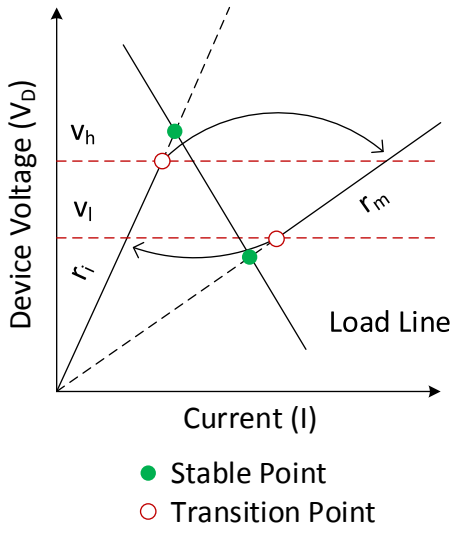

Figure 3.3: Phase space of the state transition device in a single D-R oscillator. Lines with slopes r_i and r_m are the regions of operation in insulating and metallic conduction states respectively. The intersection of these regions with the load line are the stable points in each region of operation. The transition points should be encountered before reaching the stable points for sustained oscillations as shown

We define the region of operation of a device (and hence of an oscillator) as the region where the device voltage lies between v_l and v_h (or the output voltage lies between $1 - v_l$ and $1 - v_h$). For the D-D case, the oscillators are expected to remain within the region of operation all the time. However in the D-R case, the system can go outside the region of operation in a specific manner as described later.

As in the case of D-R, the D-MOSFET circuit oscillates due to the lack of a stable point. But the load line can be controlled using the gate voltage v_{gs} which in turn affects the frequency of oscillations, and can also be used to create a bifurcation between oscillations and no oscillations. Figure 3.4 illustrates the frequency control of the relaxation oscillator with v_{gs} and illustrates the capability of the MOSFET to control the oscillation dynamics.

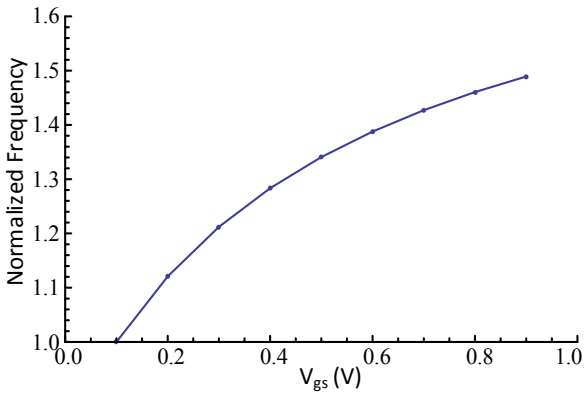

Figure 3.4: Frequency of VO_2 oscillator as a function of gate voltage. The frequency is normalized to frequency at $v_{gs} = 1$

Chapter 4

STOCHASTIC PROPERTIES

A growing need for efficient machine-learning in autonomous systems coupled with an interest in solving computationally hard optimization problems has led to active research in stochastic models of computing. Optimization techniques [65] including Stochastic Sampling Machines (SSM), Simulated Annealing, Stochastic Gradients etc. are examples of such models. All these algorithms are currently implemented using digital hardware which first creates a mathematically accurate platform for computing, and later adds digital noise at the algorithm level. Hence, it is enticing to construct hardware primitives that can harness the already existing physical sources of noise to create a stochastic computing platform. The principal challenge with such efforts is the lack of stable or reproducible distributions, or functions of distributions, of physical noise. One basic stochastic unit which enables a systematic construction of stochastic hardware has long been known - the stochastic neuron [66] - which is also believed to be the unit of computation in the human brain. Moreover, recent studies [67] have demonstrated practical applications like sampling using networks of such stochastic spiking neurons. There have been some attempts for building neuron hardware [68–72], but building a neuron with self-sustained spikes, or oscillations, which are stochastic in nature and where the probability of firing is controllable using a signal has been challenging. Here, we demonstrate and analytically study a true stochastic neuron [73] which is fabricated using oscillators [7, 62, 74] based on insulator-metal transition (IMT) materials, e.g. Vanadium Dioxide (VO_2), wherein the inherent physical noise in the dynamics is used to implement stochasticity. The firing probability, and not just the deterministic frequency of oscillations or spikes, is controllable using an electrical signal. We also show that such an IMT neuron has similar dynamics as a piecewise linear FitzHugh-Nagumo (FHN) neuron with thermal noise along with threshold fluctuations as precursors of bifurcation resulting in a sigmoid-like transfer function for the neural firing rates. By an-

alyzing the variance of interspike interval, we determine that for the range of thermal noise present in our experimental demonstrations, threshold fluctuations are responsible for most of the stochasticity compared to thermal noise.

4.1 IMT PHASE CHANGE NEURON MODEL

A stochastic IMT neuron is fabricated using relaxation oscillators [7, 74] composed of an IMT phase change device, e.g. Vanadium Dioxide (VO_2), in series with a tunable resistance, e.g. transistor [62] (Figure 4.1a). An IMT device is a two terminal device with two resistive states - insulating (I) and metallic (M), and the device transitions between the two states based on the applied electric field (which in turn changes the current through the device and the corresponding temperature) across it. The phase transitions are hysteretic in nature, which means that the IMT (insulator-to-metal) transition does not occur at the same voltage as the MIT (metal-to-insulator) transition. For a range of values of the series resistance, the resultant circuit shows spontaneous oscillations due to hysteresis and a lack of stable point [74]. Overall, the series resistance acts as a parameter for bifurcation between a spiking (or oscillating) state and a resting state of an IMT neuron.

The equivalent circuit model for an IMT oscillator is shown in Figure 4.1b with the hysteretic switching conductance $g_{v(m/i)}$ (g_{vm} in metallic and g_{vi} in insulating state), a series inductance L, and a parallel internal capacitance C. Let the IMT and MIT thresholds of the device be denoted by v_h and v_l respectively, with $v_h > v_l$, and the current-voltage relationship of the hysteretic conductance be

$$v_i = h(i_i, s)$$

where h is linear in i_i and s is the state - metallic (M) or insulating (I).

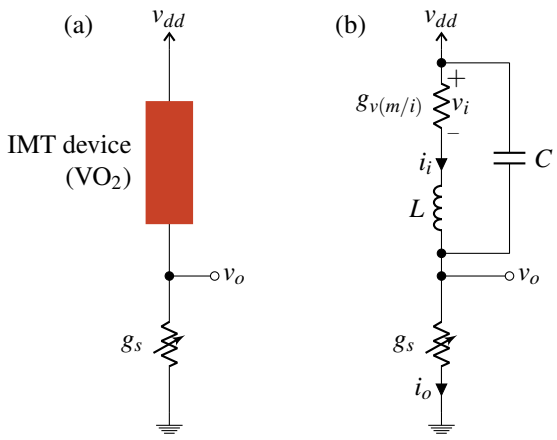

Figure 4.1: (a) VO_2 based IMT spiking neuron circuit consisting of a VO_2 device in series with a tunable resistance. (b) Equivalent circuit of IMT neuron using a series inductance L and a parallel capacitance C

The system dynamics is then given by:

$$\begin{aligned} L\frac{di_i}{dt} &= (v_{dd} - h(i_i, s)) - v_o \\ C\frac{dv_o}{dt} &= i_i - g_s v_o \end{aligned} \tag{4.1}$$

with i_i and v_o as shown in figure 4.1b and s is considered as an independent variable.

4.2 MECHANISM OF OSCILLATIONS AND SPIKES

In VO_2, IMT and MIT transitions are orders of magnitude faster than RC time constants for oscillations, as observed in frequency [75] and time-domain measurements for voltage driven [76] and photoinduced transitions [77]. As such, the change in resistance of the IMT device is assumed to be instantaneous. Figure 4.2a shows the phase space $i_i \times (v_{dd} - v_o)$. V-I curves for IMT device in the two states metallic (M) and insulating (I) and the load line for series conductance $v_o = i_i/g_s$ for the steady state are shown along with the fixed points of the system S_1 and S_2 in insulating and metallic states respectively. The load line and V-I curves are essentially the nullclines of v_o and i_i respectively. The capacitance- inductance pair delays the transitions and slowly pulls the system towards the fixed points S_1 and S_2

even when the IMT device transitions instantaneously. For small L/C ratio, the eigenvector (of the coefficient matrix) with large negative eigenvalue becomes parallel to the x-axis, whereas the other eigenvector becomes parallel to AB' or BA' depending on the state (M or I). When the system approaches A from below (or B from above) and IMT device is insulating (or metallic) with fixed point S_1 (or S_2), the IMT device transitions into metallic (or insulating) state changing the fixed point to S_2 (or S_1). Two trajectories are shown starting from points A and B each for the system (4.1) - one for small L/C value (solid) and the other for large L/C value (dashed). After a transition, the system moves parallel to x-axis almost instantaneously and spends most of the time following the V-I curve towards the fixed point. Before the fixed point is reached the MIT (or IMT) transition threshold is encountered which switches the fixed point, and the cycle continues resulting in sustained oscillations or spike generation.

4.3 MODEL APPROXIMATIONS AND CONNECTIONS WITH FHN NEURON

4.3.1 *Non-hysteretic approximation*

The model of (4.1) is very similar to a piecewise linear caricature of FitzHugh-Nagumo (FHN) neuron model [66], also called the McKean's caricature [78, 79]. Mathematically, the FHN model is given by:

$$\begin{aligned} \frac{du}{dt} &= f(u) - w + I_{ext} \\ \tau\frac{dw}{dt} &= u - bw + a \end{aligned} \tag{4.2}$$

where $f(u)$ is a polynomial of third degree, e.g. $f(u) = u - u^3/3$, and I_{ext} is the parameter for bifurcation, as opposed to g_s in (4.1). In the FHN model, one variable (u), possessing cubic nonlinearity, allows regenerative self-excitation via a positive feedback, and the second, a recovery variable (w), possessing linear dynamics, provides a slower negative feedback. It was reasoned in Ref. [79] that the essential features of FHN model are retained in a

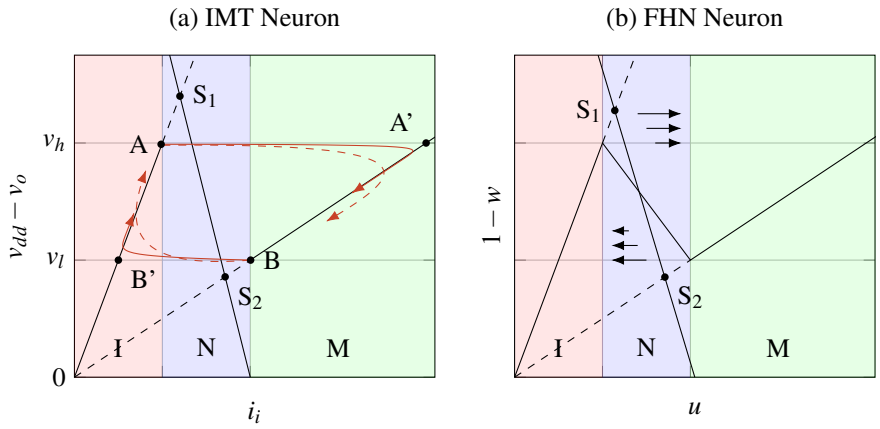

Figure 4.2: (a) Trajectories (red) of system (4.1) in the phase space $i_i \times (v_{dd} - v_o)$ for a small L/C value (solid) and a large L/C value (dashed). The i_i-nullclines of system (4.1) are shown as solid black lines in the metallic (AB') and insulating (BA') states of the IMT device, and S_1S_2 is the v_o-nullcline. Depending on the state, the phase space is divided into three vertical regions - I, N and M. In the region N the i_i-nullclines are dependent on s (b) Nullclines of the FHN model in the phase space $u \times (1-w)$ where $f(u)$ is a piecewise linear function. The dynamics of FHN neuron are equivalent to the IMT neuron in the regions M and I. In the region N, for small L/C, the difference is only in the velocity and not the direction of system trajectories as they are parallel to x-axis

"caricature" where the cubic non-linearity is replaced by a piecewise linear function $f(u)$. Nullclines of (4.2) with a piecewise linear $f(u)$ are shown in figure 4.2b in the phase space $u \times (1-w)$. A function $f(u)$ is trivially possible such that it is equal to $v_{dd} - h(i_i, s)$ in the regions M and I, hence making the u-nullcline similar to the i_i-nullcline in those regions. In the region N, the difference between $f(u)$ and $v_{dd} - h(i_i, s)$ for any state s does not result in a difference in the direction of system trajectories but only in their velocity, because for small L/C the trajectories are almost parallel to x-axis. Bifurcation in VO_2 neuron is achieved by tuning the load line using a tunable resistance (g_s), or a series transistor (figure 4.3a). Figure 4.3b shows two load line curves corresponding to different gate voltages (v_{gs}), where one gives rise to spikes while the other results in a resting state.

4.3.2 *Single dimensional approximation*

Moreover, a single dimensional piecewise approximation of the system can be performed using a dimensionality reduction by replacing the movement along the eigenvector paral-

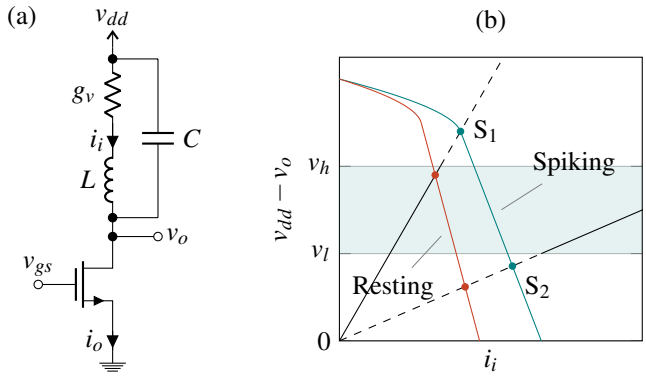

Figure 4.3: (a) IMT neuron with series transistor used to achieve bifurcation between a spiking and a resting state. (b) Nullclines of the system with series transistor in the phase space $i_i \times v_{dd} - v_o$ for two different v_{gs} values for spiking and resting states. Bifurcation occurs when a stable points crosses the boundary of region $v_{dd} - v_o \in [v_l, v_h]$.

lel to the x-axis with an instantaneous transition from A to A', or B to B'. This leaves a 1-dimensional subsystem in M and I each along the V-I curves AB' and BA'. Experiments using VO_2 show that the metallic state conductance g_{vm} is very high which causes the charging cycle of v_o to be almost instantaneous (figure 4.4) and resembles a spike of a biological neuron. As such, the spiking statistics can be studied by modeling just the discharge cycle of v_o. The inductance being negligible can be effectively removed and only the capacitance is needed for modeling the 1D subsystem of insulating state (figure 4.5a) making $v_i = v_{dd} - v_o$.

4.4 NOISE INDUCED STOCHASTIC BEHAVIOR

The two important noise sources which induce stochasticity in an IMT neuron are (a) V_{IMT} (v_h) fluctuations [80, 81], and (b) thermal noise. Thermal noise $\eta(t)$ is modeled in the circuit (figure 4.5a) as a white noise voltage $\eta(t)dt = \sigma_t dw_t$ where w_t is the standard weiner process and σ_t^2 is the infinitesimal thermal noise variance. The threshold v_h is assumed constant during a spike, but varies from one spike to another. The distribution of v_h from spike to spike is assumed to be Gaussian or subGaussian whose parameters are estimated from experimental observations of oscillations. If the series transistor always remains in

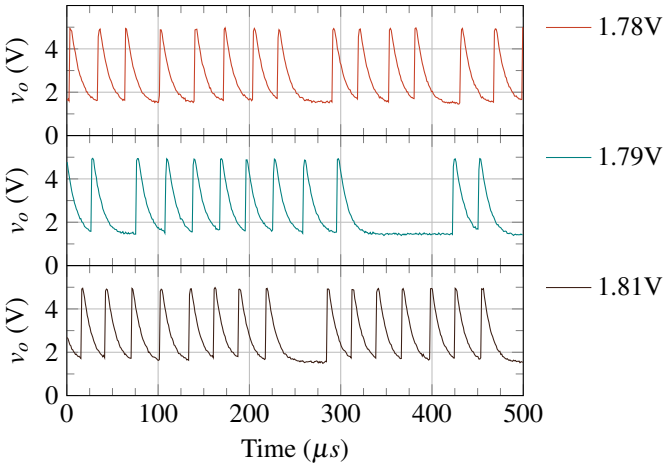

Figure 4.4: Experimental waveforms of VO_2 based spiking neuron for various v_{gs} values (1.78V, 1.79V and 1.81V). A VO_2 neuron shows almost instantaneous charging (spike) in metallic state.

saturation and show linear voltage-current relationship, as is the case in our VO_2 based experiments, the discharge phase can be described by an Ornstein-Uhlenbeck (OU) process

$$\mathrm{d}x = \frac{1}{\theta}(\mu - x)\mathrm{d}t + \sigma \mathrm{d}w_t \tag{4.3}$$

where μ,θ and σ are functions of circuit parameters of the series transistor, the IMT device and σ_t. The interspike interval is thus the first-passage-time (FPT) of this OU process, but with a fluctuating boundary.

4.4.1 *OU process with constant boundary*

Analytical expressions for the FPT of OU process (with $\mu = 0$) for a constant boundary were derived using the Laplace transform method in Ref. [82]. Reproducing some of its results, let the first passage time for the system (4.3), with $\mu = 0$, which starts at $x(0) = x_0$ and hits a boundary S, be denoted by the random variable $\mathbf{t_f}(S,x_0)$, and its m^{th} moment by $\tau_m(S,x_0)$. Also, let $\widetilde{\mathbf{t_f}}(S,x_0)$ be the FPT for another OU process with $\mu = 0$, $\theta = 1$ and $\sigma = 2$, and $\widetilde{\tau_m}(S,x_0)$ be its m^{th} moment. Then time and space scaling for the OU process

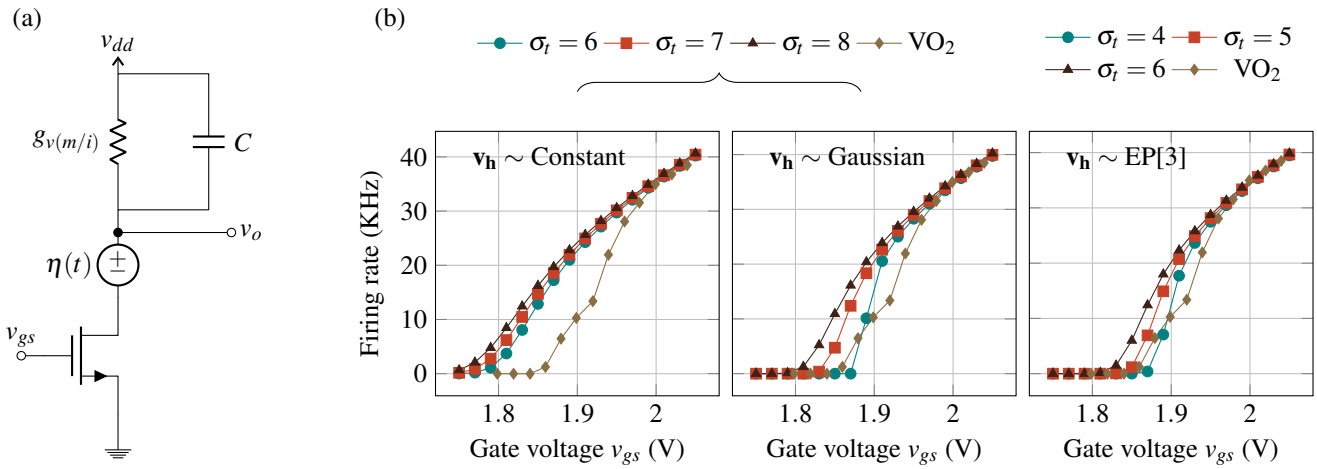

Figure 4.5: (a) Noise model of IMT neuron where the noise components are the thermal noise voltage source $\eta(t)$ and the IMT threshold fluctuation. (b) Firing rate plotted against v_{gs} using the analytical model for different $\mathbf{v_h}$ distributions (Constant, Gaussian, and EP[3]) and comparison with experimental observations.

imply that

$$\begin{aligned} \mathbf{t_f}(S,x_0) &\stackrel{d}{=} \theta\widetilde{\mathbf{t_f}}(\alpha S,\alpha x_0) \\ \therefore \tau_m(S,x_0) &= \theta^m\widetilde{\tau_m}(\alpha S,\alpha x_0) \end{aligned} \tag{4.4}$$

where $\alpha = \sqrt{\frac{2}{\theta\sigma^2}}$. The first 2 moments for the base case OU process $\widetilde{\tau_1}$ and $\widetilde{\tau_2}$ are given by

$$\begin{aligned} \widetilde{\tau_1}(S,x_0) =& \phi_1(S) - \phi_1(x_0) \\ \widetilde{\tau_2}(S,x_0) =& 2\phi_1(S)^2 - \phi_2(S) - 2\phi_1(S)\phi_1(x_0) + \phi_2(x_0) \end{aligned} \tag{4.5}$$

where $\phi_k(z)$ can be written as an infinite sum

$$\phi_k(z) = \frac{1}{2^k}\sum_{n=1}^{\infty}\frac{\left(\sqrt{2}z\right)^n\Gamma\left(\frac{n}{2}\right)\rho(n,k)}{n!} \tag{4.6}$$

with $\rho(n,k)$ being a function of the digamma function [82].

4.4.2 *OU process with fluctuating boundary*

We extend this framework for calculating the FPT statistics with a fluctuating boundary $\mathbf{S}$ as follows. Let the IMT threshold be represented by the random variable $\mathbf{v_h}$. For the VO_2 based IMT neuron, the 1D subsystem in the insulating phase can be converted in the form of (4.3) with $\mu = 0$ by translating the origin to the fixed point. If this transformation is T then $x = \mathrm{T}v_i = \mathrm{T}(v_{dd} - v_o)$, $\mathbf{S} = \mathrm{T}\mathbf{v_h}$ and $x_o = \mathrm{T}v_l$. The start and end points are B' and A respectively in figure 4.2. $\mathbf{v_h}$ is assumed constant during a spike, and across spikes the distribution of $\mathbf{v_h}$ is $\mathbf{v_h} \sim \mathscr{D}$, where $\mathscr{D}$ is either Gaussian, or subGaussian. For subGaussian distributions we use the Exponential Power family EP[κ], κ being the shape factor. Let the interspike interval of IMT neuron be denoted by the marginal random variable $\mathbf{t_{imt}}(\mathscr{D}, v_l)$. Then $\mathbf{t_{imt}}$ is related to $\mathbf{t_f}$ in equation (4.4), given common parameters θ and σ, as follows:

$$\mathbf{t_{imt}}(\mathscr{D}, v_l)|(\mathbf{v_h} = v) \stackrel{d}{=} \mathbf{t_f}(\mathrm{T}v, \mathrm{T}v_l)$$

The moments of $\mathbf{t_{imt}}$ can be calculated as:

$$\begin{aligned}
\mathbb{E}[\mathbf{t_{imt}}(\mathscr{D}, v_l)^m] &= \mathbb{E}_{v_h}[\mathbb{E}[\mathbf{t_{imt}}(\mathscr{D}, \mathrm{T}v_l)^m | \mathbf{v_h} = v]] \\
&= \mathbb{E}_{v_h}[\tau_m(\mathrm{T}\mathbf{v_h}, \mathrm{T}v_l)] \\
&= \theta^m \mathbb{E}_{v_h}[\widetilde{\tau_m}(\alpha\mathrm{T}\mathbf{v_h}, \alpha\mathrm{T}v_l)] \qquad (4.7)
\end{aligned}$$

where $\alpha = \sqrt{\frac{2}{\theta\sigma^2}}$. If $\mathscr{D}$ is Gaussian or EP[κ] distribution and αT is an affine transformation, then $\alpha\mathrm{T}\mathbf{v_h}$ also has a Gaussian or EP[κ] distribution.

4.5 EXPERIMENTS

IMT devices are fabricated on a 10nm VO_2 thin film grown by reactive oxide molecular beam epitaxy on (001) TiO_2 substrate using a Veeco Gen10 system [83]. Planar two terminal structures are formed by patterning contacts using standard electron beam lithog-

raphy which defines the device length (L_{VO2}). Pd (20nm) / Au (60nm) contacts are then deposited by electron beam evaporation and liftoff. The devices are then isolated and the widths (W_{VO2}) are defined using a CF_4 based dry etch.

The IMT neuron is constructed using an externally connected n-channel MOSFET (ALD110802) and the fabricated VO_2 device. A prototypical I-V curve is shown in figure 4.6a. Within the experimental data, the current is limited to an arbitrarily chosen 200 μA to prevent a thermal runaway and breakdown of the device while in the low resistance metallic state. It should be noted that as the metallic state corresponds to the abrupt charging cycle of v_o, limiting the current would not have noticeable effect on spiking statistics of the neuron.

Threshold voltage fluctuations (cycle to cycle) were observed in all devices which were tested (> 10). Threshold voltage distribution was estimated using the varying cycle-to-cycle threshold voltages collected from a single device. Thermal noise is not measured directly, but is estimated approximately by matching the simulation waveforms from the circuit model (Figure 4.5a) with the observed experimental waveforms. It can be verified that thermal noise of the transistor is not the dominant noise source by measuring the threshold variation as a function of the transistor current (Figure 4.6b) and observing that the distribution of switching threshold does not change with varying transistor current. Finally, the firing rate and its variation with v_{gs} (Figure 4.5b) were measured for a single device.

4.6 SPIKING STATISTICS

4.6.1 *First moment and the firing rate*

First moment of $\mathbf{t_{imt}}$ is calculated using (4.5) and (4.7) as

$$\mathbb{E}[\mathbf{t_{imt}}(\mathscr{D}, v_l)] = \theta(\mathbb{E}_{v_h}[\phi_1(\alpha \mathrm{T}\mathbf{v_h})] - \phi_1(\alpha x_0))$$

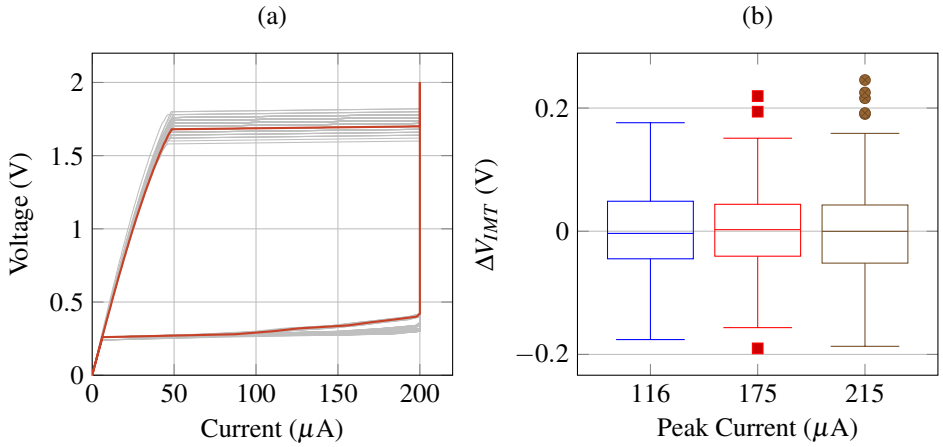

Figure 4.6: (a) The prototypical DC voltage-current characteristics for a single VO_2 device exhibits abrupt threshold switching at V_{IMT} and V_{MIT}. The current in the metallic state has been arbitrarily limited to a 200μA compliance current. (b) V_{IMT} distribution as a function of the peak current during oscillations (value is set by the MOSFET saturation current). V_{IMT} is extracted from 300+ cycles.

The expansion for $\phi_k(z)$ in (4.6) can be used to calculate $\mathbb{E}_{v_h}[\phi_k(\alpha \mathrm{T}\mathbf{v_h})]$ using the moments of $\alpha \mathrm{T}\mathbf{v_h}$ as follows

$$\mathbb{E}_{v_h}[\phi_k(\alpha \mathrm{T}\mathbf{v_h})] = \frac{1}{2^k}\sum_{n=1}^{\infty}\frac{(\sqrt{2})^n \mathbb{E}[(\alpha \mathrm{T}\mathbf{v_h})^n]\Gamma\left(\frac{n}{2}\right)\rho(n,k)}{n!}$$

Figure 4.5b shows firing rate $(1/\mathbb{E}[\mathbf{t_{imt}}(\mathscr{D}, v_l)])$ as a function of v_{gs} for various σ_t values and for 3 distrbutions of threshold fluctuations. The calculations approximate the experimental observations well for all three v_h distributions, the closest being EP[3] with $\sigma_t = 4$.

4.6.2 *Higher moments*

For higher moments, higher order terms are encountered. For example, in case of the second moment, using (4.5) and (4.7), we obtain

$$\begin{aligned}\mathbb{E}_{v_h}[\widetilde{\tau}_2(\alpha \mathrm{T}\mathbf{v_h}, \alpha \mathrm{T}v_l)] =& 2\mathbb{E}_{v_h}[\phi_1(\alpha \mathrm{T}\mathbf{v_h})^2] - \mathbb{E}_{v_h}[\phi_2(\alpha \mathrm{T}\mathbf{v_h})] \\ & - 2\mathbb{E}_{v_h}[\phi_1(\alpha \mathrm{T}\mathbf{v_h})]\phi_1(\alpha \mathrm{T}v_l) \\ & + \phi_2(\alpha \mathrm{T}v_l)\end{aligned}$$

with a higher order term $\phi_1(\alpha \mathrm{T}\mathbf{v_h})^2$. In the case of the third moment we obtain $\phi_1(\alpha \mathrm{T}\mathbf{v_h})\phi_2(\alpha \mathrm{T}\mathbf{v_h})$. As each ϕ_k term is an infinite sum, we construct a cauchy product expansion for the higher order term using the infinite sum expansions of the constituent ϕ_ks and then distribute the expectation over addition. For example, if the ϕ_k expansions of $\phi_1(z)$ and $\phi_2(z)$ are $(\sum a_i)$ and $(\sum b_i)$ respectively, then the cauchy product expansion of $\phi_1(z)\phi_2(z)$ can be calculated as $\sum c_i$, where c_i is a function of $a_{1\ldots i}$ and $b_{1\ldots i}$, and the expectation $\mathbb{E}[\phi_1(z)\phi_2(z)] = \sum \mathbb{E}[c_i]$. Since c_i is a polynomial in z, $\mathbb{E}[c_i]$ can be calculated using the moments of z.

If μ_{imt} and σ_{imt} are the mean and standard deviation of interspike intervals $\mathbf{t_{imt}}$, the coefficient of variation (σ_{imt}/μ_{imt}) varies with the relative proportion of the thermal and the threshold induced noise. Figure 4.7 shows σ_{imt}/μ_{imt} (calculated using parameters matched with our VO_2 experiments) plotted against σ_t for various kinds of $\mathbf{v_h}$ distributions fitted to experimental observations. σ_{imt}/μ_{imt} as observed in our VO_2 experiments is about an order of magnitude more than what would be calculated with only thermal noise using such a neuron, and hence, threshold noise contributes significant stochasticity to the spiking behavior. As the IMT neuron is setup such that the stable point is close to the IMT transition point (figure 4.3b), low σ_t results in high and diverging σ_{imt}/μ_{imt} for any distribution of threshold noise, and σ_{imt}/μ_{imt} reduces with increasing σ_t for the range shown. For a Normally distributed v_h the variance diverges for $\sigma_t \lesssim 8$, but for Exponential Power (EP) distributions with lighter tails, the variance converges for smaller values of σ_t. Statistical measurements on experimental data, as indicated in figure 4.7, provide measures of σ_{imt}/μ_{imt} (dotted line) and σ_t (shaded region). We note that EP distributions provide a better approximation of the stochastic nature of experimentally demonstrated VO_2 neurons as the range of σ_t is estimated to be less than 5.

4.7 COMPARISON WITH OTHER WORK

The IMT neuron emulates the functionality of theoretical neuron models completely by incorporating all neuron characteristics into device phenomena. Unlike other similar efforts,

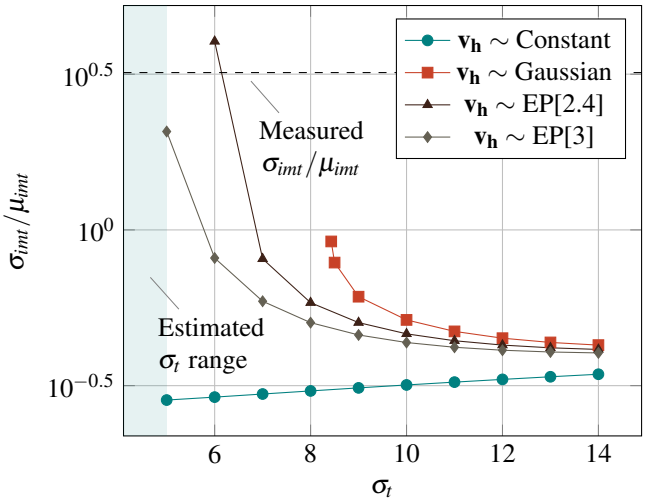

Figure 4.7: σ_{imt}/μ_{imt} for the interspike interval plotted against σ_t for $v_{gs} = 1.8$V with Constant, Gaussian and Exponential Power (EP[κ], where κ is the shape factor) distributions of the threshold noise. The experimentally observed σ_{imt}/μ_{imt} for a VO_2 neuron is shown with a dotted line. The shaded region shows the experimentally estimated range of σ_t ($\sigma_t < 5$)

it does not need peripheral circuits alongside the core device circuit (an IMT device and a transistor) to emulate any sub-component of the spiking neuron model like thresholding, reset etc. Moreover, the neuron construction not only utilizes inherent physical noise sources for stochasticity, but also enables control of firing probability using an analog electrical signal - the gate voltage of series transistor. This is different from previous works which control only the deterministic aspect of firing rate like the charging rate. A comparison of spiking neuron hardware characteristics in different works is shown in Table 4.1.

Such analytical verification of stochastic neuron experiments is one of the first in this work. It is an important result as it indicates reproducibility of stochastic characteristics and helps in creating the pathway towards perfecting these devices. With a growing concensus that stochasticity will play a key role in solving hard computing tasks, we need efficient ways for controlled amplification and conversion of physical noise into a readable and computable form. In this regard, the IMT based neuron represents a promising solution for a stochastic computational element. Such stochastic neurons have the potential to realize bio-mimetic computational kernels that can be employed to solve a large class of

Table 4.1: Comparison of this work (experimental details from [73]) with other spiking neuron hardware works based on different characteristics of spiking neurons

	Tuma *et al.* [6]	**Pickett *et al.*** [7]	**Sengupta *et al.*** [5]	**Indiveri *et al.*** [8]	**This work (VO_2)**
Neuron type	Integrate & Fire	Hodgkin Huxley	Integrate & Fire	Integrate & Fire	Piecewise Linear FHN
Material / Platform	Chalcogenide	Mott insulator NbO_2	MTJ	0.35 µm CMOS	Vanadium Dioxide (VO_2)
Material phenomenon	Phase Change	IMT	Spin transfer torque (STT)	-	IMT
Spontaneous spiking using only device	No	Yes	No	-	Yes
Peripherals needed for spiking	Yes, for spike generation and reset	No	Yes, for spike generation and reset	-	No
Integration mechanism (I&F)	Heat accumulation	-	Magnetization accumulation	Capacitor charging	Capacitor charging
Threshold mechanism (I&F)	External reset by measuring conductance	Spontaneous IMT	External reset by detecting magnet flip	Reset using comparator	Spontaneous IMT
Stochastic	Yes	-	Yes	No	Yes
Kind of stochasticity (I&F)	Reset potential	-	Differential	-	Threshold and differential
Source of stochasticity / noise	Melt-quench process	-	Thermal noise	-	IMT threshold fluctuations & Thermal noise
Control of stochastic firing rate	Only integration rate	-	Only integration rate	Only integration rate	Yes
Status of experiments	Constant stochasticity, variable integration rate	Deterministic spiking	None	Deterministic spiking	Sigmoidal variation of stochastic firing rates
Peak current	750-800 µA		-		200 µA
Power or Energy/spike	120 µW		-	900 pJ / spike	196 pJ / spike
Voltage	5.5 V	1.75 V	-	3.3 V	0.7V
Maximum firing rates	35-40 KHz	30 KHz	-	200 Hz	30 KHz

optimization and machine-learning problems.

Chapter 5

PAIRWISE COUPLING

5.1 THIS WORK

The circuit diagram of two coupled oscillators, D-D or D-R, is shown in figure 5.1. The importance of a physical realization of relaxation oscillators can be clearly seen here, as without it we would not be able to characterize, and hence analyse, the coupling behavior of oscillators, and by extension we would not be able to understand computational abilities of such circuits.

5.1.1 *Phase space, flows and oscillation conditions*

For analyzing the coupled circuits, the phase diagram of a coupled system can be drawn in the $v_1 \times i_1 \times v_2 \times i_2$ space as was done in figure 3.3. However, we note that in a given conduction state of the system, $s = s_1 s_2$, (v_1, v_2) can uniquely identify the system, and hence, $v_1 \times v_2$ space is sufficient for a phase diagram. Therefore, we can draw 4 different phase diagrams of the system for each conduction state s (figure 5.2) with transitions among them[84] (figure 5.3). The transitions occur at the edges when either v_1 or v_2 reach the higher or lower threshold for state change from metallic to insulating or vice versa. The flows in each of the 4 conduction states are linear flows and hence have a single fixed point (figure 5.2). The conditions for oscillations can be described using figure 5.4. Analogous to the case of a single oscillator, these stable points should lie outside the region of operation (in the shaded region) in a way that the system always tries to move towards these stable points but should be preceded by a state transition which occurs when the system reaches the (red) dashed lines.

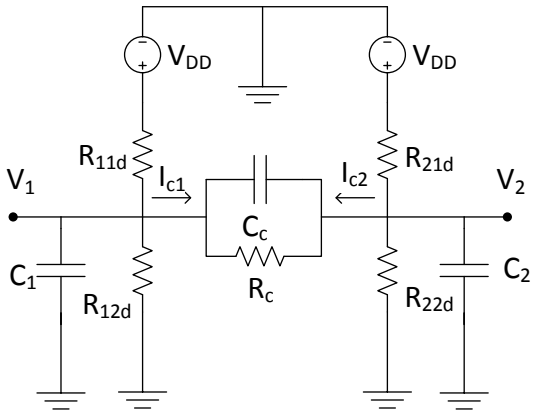

Figure 5.1: Circuit equivalent of coupled D-D oscillators of with an RC circuit used as the coupling circuit. For D-R oscillators, one state-changing resistor of each oscillator is replaced by a constant linear resistor

5.1.1.1 *Monotonic Flows and Periodic Orbits*

The conditions of figure 5.4 are general enough to hold for both D-D and D-R configurations and they ensure that the system does not settle down to a stable point and voltages across oscillators repeatedly increase and decrease. However, these conditions do not ensure the existence of a stable orbit which can give periodic oscillations. To ensure existence of a stable periodic orbit, we consider additional conditions for the systems. For D-D configuration, we consider systems where the flows in the states are monotonic, i.e. v_1 and v_2 are either constantly increasing or constantly decreasing in the region of operation of any conduction state. Figure 5.3 show these monotonic directions with the state transitions for D-D coupled oscillator configurations. It is proved later that for two identical coupled D-D oscillators, this condition of monotonicity of the flows is *sufficient* for existence of a stable orbit and hence for periodic oscillations. For D-R coupled oscillators, we consider systems where either the direction of flows are strictly monotonic as shown in figure 5.3 or are non-monotonic in a very specific way as discussed in 5.1.3 (see figure 5.21). In this case, periodic oscillations can be ensured for certain conditions as described in section 5.1.3. It should be noted here that in the D-R case, the system can also go outside the region of operation as seen in figure 5.5b, but if the fixed points lie in the above mentioned shaded

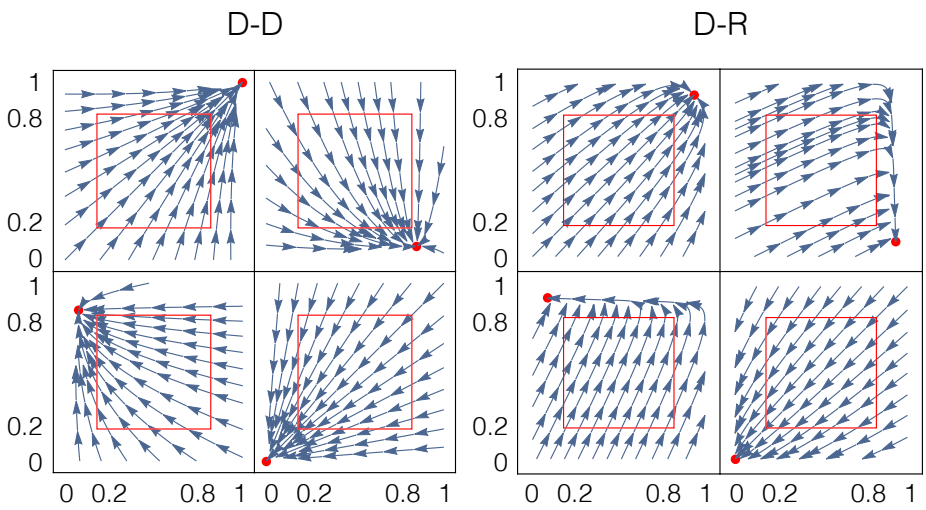

Figure 5.2: The coupled system can be described by 4 different phase spaces for each state $s = s_1 s_2$. This figure shows the system flows of the D-D and D-R coupled oscillator system in the 4 regions of operation along with the fixed points (shown as red dots) in each state. This figure also represents the simplified case where the flows are monotonic within the region of operation

regions, the system will always oscillate. Figure 5.5 shows typical time-domain waveforms and corresponding phase-space trajectories for the coupled oscillators of the D-D and D-R types.

For D-MOSFET kind of oscillator circuit, similar phase space and oscillation conditions as D-R hold. Figure 5.6 shows the phase space flows for two coupled D-MOSFET kind of oscilators, with the red trajectory showing the limit cycle in this case.

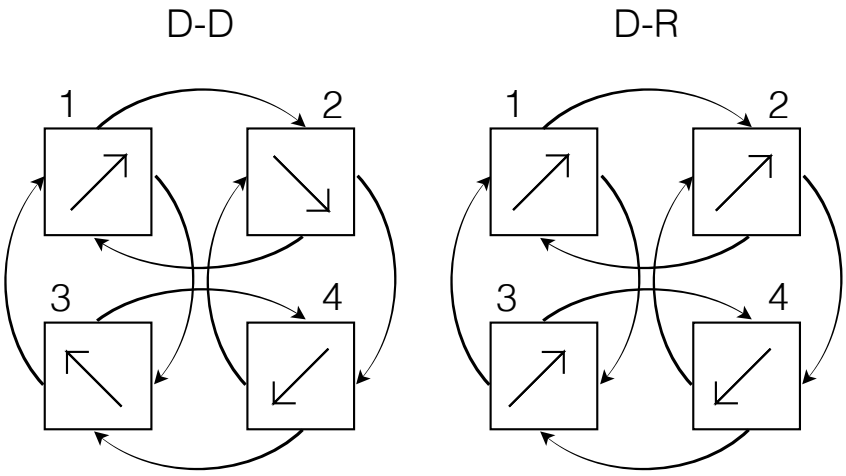

Figure 5.3: Schematic representation showing the monotonic flow directions in the regions of operation in the simplified model. The monotonicity condition is sufficient for existence of a steady state periodic orbit in the D-D case. Transitions are shown among the 4 states 1(MM), 2(IM), 3(MI) and 4(II) of the coupled system when the system reaches any edge, i.e. the voltage of any oscillator reaches a phase change threshold of its IMT device

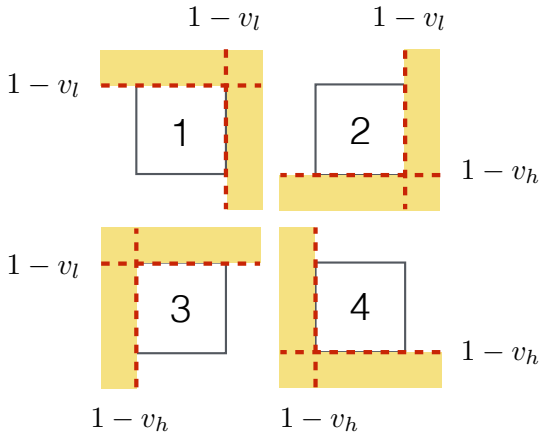

Figure 5.4: The stable points of both D-D and D-R coupled oscillator system should lie in the yellow shaded region for the system to oscillate. The system undergoes a transition to another state when the system hits the red dashed lines

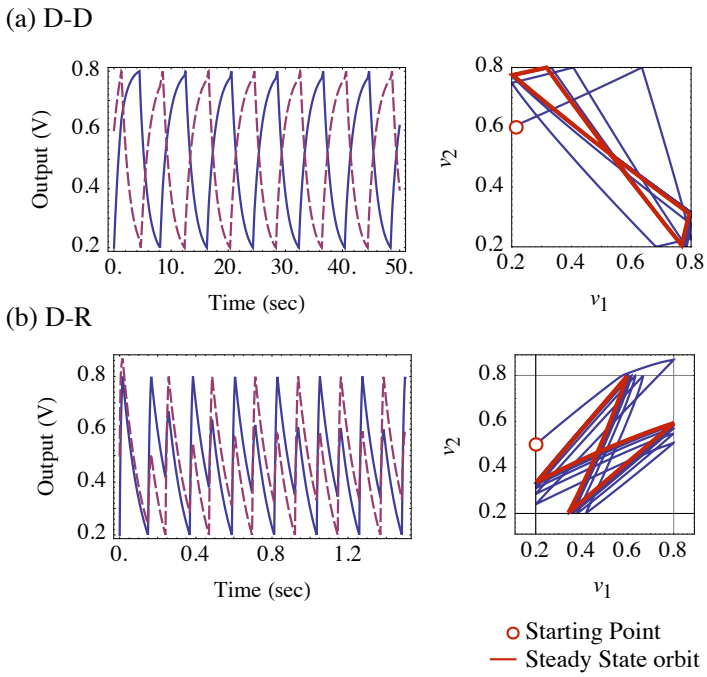

Figure 5.5: Simulation waveforms with time (left) and the system trajectory in phase space (right) of a system of coupled oscillators of type (a) D-D and (b) D-R. The steady state periodic orbit is shown in red. The butterfly shaped steady state trajectory corresponds to waveforms similar to anti-phase locking. The solid and dashed lines represent output of the two oscillators.

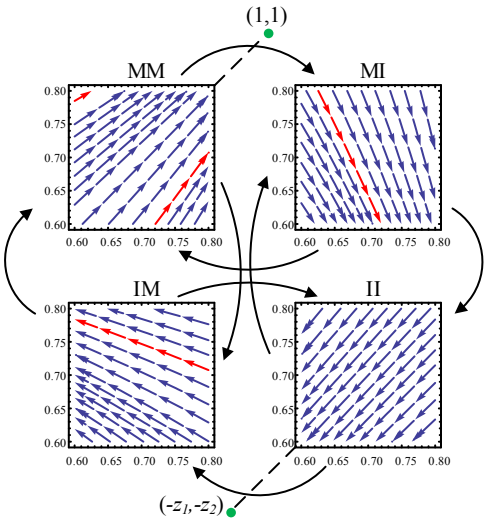

Figure 5.6: Regions of state space of the D-MOSFET coupled oscillator system with parameter values $g : g_0 : g_m = 3 : 1 : 3$, $\alpha = 10$, $v_{gs1} = 0.5$ and $v_{gs2} = 0.4$. Fixed points z_1 and z_2 in states MM and II respectively are shown where $z_1 = g_{m1} v_{gs1}$ and $z_2 = g_{m2} v_{gs2}$. Steady state periodic orbit of the system is marked in red among the flows in the state space. Arrows outside the state space show the transitions between the regions when the system hits any edge.

5.1.2 *D-D oscillators*

5.1.2.1 *Modeling*

When two identical D-D oscillators are coupled in a manner described in figure 5.1, the system can be described by the following coupled equations:

$$c_1 v_1' = \begin{cases} (v_{dd} - v_1) g_{11dm} - i_{c1} & charging \\ -v_1 g_{12dm} - i_{c1} & discharging \end{cases} \tag{5.1}$$

$$c_2 v_2' = \begin{cases} (v_{dd} - v_2) g_{21dm} - i_{c2} & charging \\ -v_2 g_{22dm} - i_{c2} & discharging \end{cases} \tag{5.2}$$

where c_1 and c_2 are the lumped capacitances of the oscillators. For conductances g, the first subscript denotes the oscillator and the second denotes the device. $i_{c1} = -i_{c2}$ is the coupling current given by:

$$i_{c1} = (v_1' - v_2')c_c + (v_1 - v_2)g_c \tag{5.3}$$

When coupled, the system has 4 conduction states $s = s_1 s_2 \in \{00, 01, 10, 11\}$ corresponding to the 4 combinations of s_1 and s_2. Analogous to (3.2), the coupled system can be described in matrix form as:

$$\begin{aligned} c_c F x'(t) &= -g_c A(s) x(t) + P(s) \\ x'(t) &= -\frac{g_c}{c_c} F^{-1} A(s) \left(x(t) - A^{-1}(s) P(s) \right) \end{aligned} \tag{5.4}$$

where $x(t) = (v_1(t), v_2(t))$ is the state variable at any time instant t. The 2×2 matrices

F and $A(s)$, and vector $P(s)$ are given by:

$$F = \begin{bmatrix} 1+\alpha_1 & -1 \\ -1 & 1+\alpha_2 \end{bmatrix} \tag{5.5}$$

$$\begin{aligned} A(00) &= \begin{bmatrix} -\beta_{11}-1 & 1 \\ 1 & -\beta_{21}-1 \end{bmatrix}, \quad P(00) = \begin{bmatrix} \beta_{11} \\ \beta_{21} \end{bmatrix} \\ A(10) &= \begin{bmatrix} -\beta_{12}-1 & 1 \\ 1 & -\beta_{21}-1 \end{bmatrix}, \quad P(10) = \begin{bmatrix} 0 \\ \beta_{21} \end{bmatrix} \\ A(01) &= \begin{bmatrix} -\beta_{11}-1 & 1 \\ 1 & -\beta_{22}-1 \end{bmatrix}, \quad P(01) = \begin{bmatrix} \beta_{11} \\ 0 \end{bmatrix} \\ A(11) &= \begin{bmatrix} -\beta_{12}-1 & 1 \\ 1 & -\beta_{22}-1 \end{bmatrix}, \qquad P(11) = 0 \end{aligned} \tag{5.6}$$

Here, $\alpha_i = c_i/c_c$ is the ratio of the combined lumped capacitance of i^{th} oscillator to the coupling capacitance c_c, and $\beta_{ij} = g_{ijdm}/g_c$ is the ratio of the metallic state resistance of j^{th} device of i^{th} oscillator, where $i \in \{1,2\}$ and $j \in \{1,2\}$. The fixed point in a conduction state s is given by $p_s = A^{-1}(s)P(s)$ and the matrix determining the flow (the *flow matrix* or the *velocity matrix*) is given by $\frac{g_c}{c_c}F^{-1}A(s)$ as can be seen in (5.4). In section 5.1.2.2 we analyze the steady state locking and synchronization dynamics of two such identical oscillators coupled with a parallel resistive and capacitive element as shown in figure 5.1.

5.1.2.2 *Symmetric D-D oscillators*

Let us first investigate the case when the D-D oscillators are identical and their effective charging and discharging rates are equal, i.e. $\beta_{11} = \beta_{21} = \beta_{12} = \beta_{22} = \beta$ and $\alpha_1 = \alpha_2$. This corresponds to a well designed and ideal oscillator system where the pull-up and pull-down device resistances have been matched to create equal charging and discharging rates. In such a scenario the velocity matrices in the four conduction states $\frac{g_c}{c_c}F^{-1}A(s)$

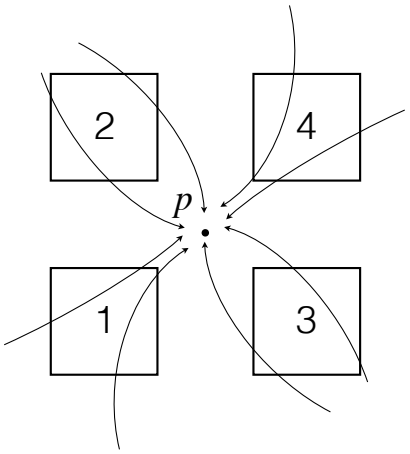

Figure 5.7: Combined phase space in the symmetric D-D coupled oscillator case showing 4 regions of operation of the four different conduction states such that all states share a single fixed point p. This is possible as the flow matrices in all the four states are equal and, hence, all state spaces can be represented in a single space with a single flow but occupying different regions

become equal. As such, the state spaces in the four conduction states can be represented in a common state space with the system flow described by the common velocity matrix and a single fixed point. However, in this common state space, the regions of operation in the four conduction states will be four distinct regions. The position of these regions for a conduction state would depend on the position of its respective fixed points in the original state space. Such a combined phase space is shown in figure 5.7.

The symmetry of the system is apparent in the flow as well. The eigen values λ_1, λ_2 and eigen vectors e_1, e_2 of the velocity matrix $\frac{g_c}{c_c} F^{-1} A$ of the symmetric system are

$$\lambda_1 = -\frac{g_c}{c_c}\left(\frac{\beta}{\alpha}\right), \lambda_2 = -\frac{g_c}{c_c}\left(\frac{\beta+2}{\alpha+2}\right) \tag{5.7}$$

$$e_1 = \begin{bmatrix} 1 \\ 1 \end{bmatrix}, e_2 = \begin{bmatrix} -1 \\ 1 \end{bmatrix} \tag{5.8}$$

Real negative eigen values imply that the flow of the system is symmetric about both the eigen vector directions (i.e. a mirror image of itself about the eigen directions) as shown

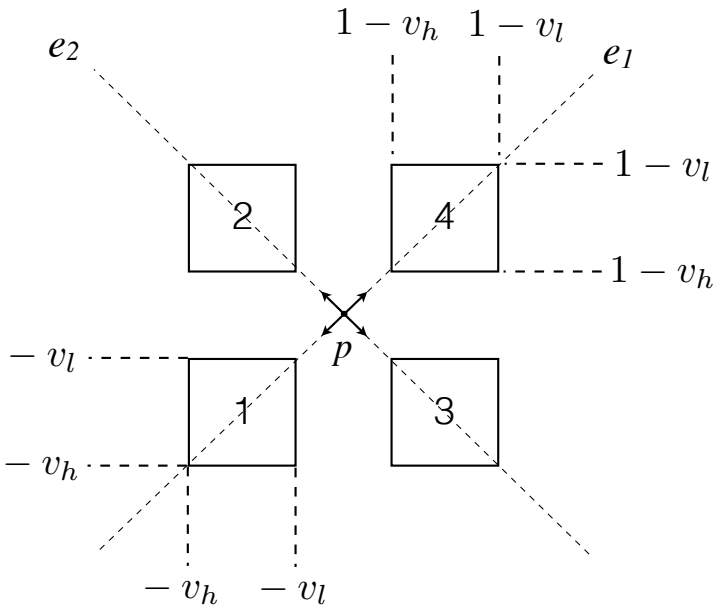

Figure 5.8: In the combined phase space, the flow of the coupled system is a mirror image of itself about its eigen vector directions e_1 and e_2 as the eigen values are real and negative. This symmetry of the flows can be reduced and the state space of the system can be described by considering just one-fourth of this space as shown in figure 5.9

in figure 5.8. The stable fixed points in the conduction states 1(00), 2(01), 3(10) and 4(11) are $p_1 = (1,1)$, $p_2 = \left(1-\frac{1}{2+\beta}, \frac{1}{2+\beta}\right)$, $p_3 = \left(\frac{1}{2+\beta}, 1-\frac{1}{2+\beta}\right)$ and $p_4 = (0,0)$ respectively. Hence, the line along the eigen vector e_1 is the diagonal for both conduction states 1 and 4. Under the assumption that the v_{dd} normalized thresholds v_l and v_h are symmetric i.e. $v_l = 1 - v_h$, the line along e_2 also becomes the diagonal for states 2 and 3. This is because the fixed points of conduction states 2 and 3 - p_2 and p_3 lie on $x + y = 1$ line in their original state spaces which is same as the eigen direction e_2. It should now be noted that the transitions between the conduction states, the regions of operation and the flow, all have the same common discrete symmetry - mirroring about e_1 and e_2. We can do a symmetry reduction at this point and the system can be completely described by just two states and two transitions (figure 5.9a).

To study the steady state periodic orbits of this system, we calculate the return map on the left edge of state 1 in figure 5.9a which is $f = f_1 \circ f_2$. In this case, any periodic orbit in the symmetry reduced space will correspond to at least one periodic orbit in the

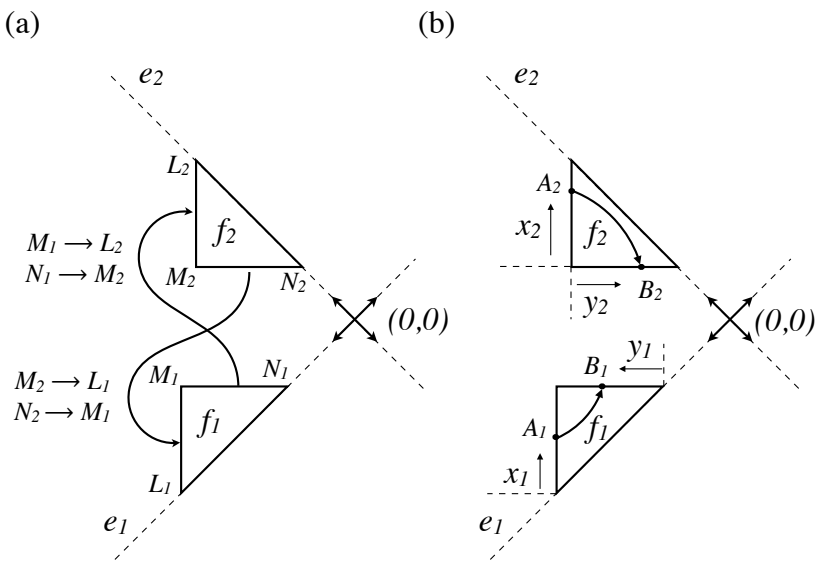

Figure 5.9: (a) Symmetry reduced space (fundamental domain) of the coupled system after reducing the symmetries shown in figure 5.8. f_1 is the mapping from the left edge of state 1 to its top edge and f_2 is the mapping from left edge of state 2 to its bottom edge. (b) Definition of x_1, x_2, y_1 and y_2 on the edges of the states in the symmetry reduced space

complete space (see figure 5.11). Also, if no fixed point of the return map exist in the symmetry reduced space, then there is definitely no periodic orbit in the complete space. The coordinate measurements on the edges are defined as shown in 5.9b. $f_1 : x_1 \to y_1$ is the mapping from the left edge of state 1 to its top edge and $f_2 : x_2 \to y_2$ is the mapping from left edge of state 2 to its bottom edge. x_1, x_2, x_3 and x_4 are defined on their respective edges as shown in figure 5.9b. As both the eigen values λ_1 and λ_2 are real and negative, $f_1(x)$ will lie above $x = y$ line and $f_2(x)$ will lie below it. A representative plot of f_1, f_2 and $f = f_1 \circ f_2$ (i.e. the return map $f : x_1 \to y_2$) is shown in figure 5.10 where $dv = v_h - v_l$. The composition $f = f_1 \circ f_2$ lies above $x = y$ if f_2 is more curved than f_1 and vice versa. As the return map is always increasing, only the first return map needs to be considered for finding fixed points and the higher return maps don't add new fixed points. When the coupling is more capacitive, the composition function tends to be concave as shown in figure 5.10a. *Proposition* 1 gives a mathematical form to this notion where a sufficient condition is proved for anti-phase locking. We show numerically with simulations in figure

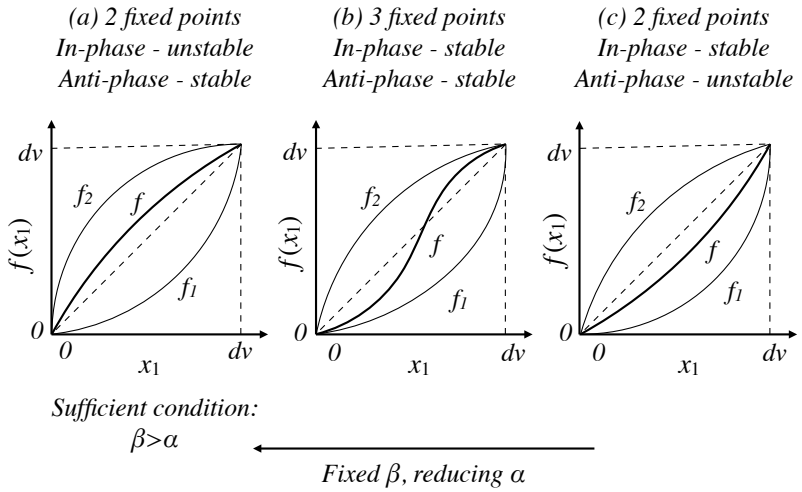

Figure 5.10: Representative plot of mappings f_1, f_2 and their composition $f = f_1 \circ f_2$ with fixed β and varying α. Here $dv = v_h - v_l$. $\beta > \alpha$ is a sufficient condition for a concave f and hence stable anti-phase locking. As α increases, the curve for f transitions into a s-shaped curve with both in-phase and anti-phase lockings stable, and then finally to a convex curve with stable in-phase locking

5.13 the conditions for in-phase locking compared to anti-phase locking.

If the system moves from any arbitrary point on the flow, say (x_a, y_a) to another point, (x_b, y_b) in time t then the following implicit equation can be written:

$$\left(\frac{x_a + y_a}{x_b + y_b}\right)^{\frac{1}{\lambda_1}} = \left(\frac{x_a - y_a}{x_b - y_b}\right)^{\frac{1}{\lambda_2}} \tag{5.9}$$

In state 1, (x_a, y_a) lies on the left edge and (x_b, y_b) lies on the top edge. To define $f_1 : x_1 \to y_1$ we substitute $(x_a, y_a) = (-v_h, -v_h + x_1)$ in (5.9) and obtain an implicit equation for f_1 as:

$$\left(\frac{2v_h - x_1}{2v_l + y_1}\right) = \left(\frac{x_1}{y_1}\right)^{\frac{\alpha+2}{\beta+2}\frac{\beta}{\alpha}} \tag{5.10}$$

Similarly, an implicit equation for $f_2 : x_2 \to y_2$ can be written as:

$$\left(\frac{k_\beta + x_2}{k_\beta - y_2}\right) = \left(\frac{dv - x_2}{dv - y_2}\right)^{\frac{\beta+2}{\alpha+2}\frac{\alpha}{\beta}} \tag{5.11}$$

where $k_\beta = \frac{\beta}{\beta+2}$.

Equations 5.10 and 5.11 can be solved numerically to obtain the steady state orbits of the system.

Proposition 1 : *Existence of stable periodic orbit and sufficient condition for stable anti-phase locking in symmetric D-D coupled oscillator system:* For $\beta > \alpha > \frac{2dv}{1-dv} = \frac{dv}{v_l}$, i.e., $\frac{g_{dm}}{g_c} > \frac{c}{c_c} > \frac{2dv}{1-dv} = \frac{dv}{v_l}$ the coupled symmetric and identical system has only two steady state locking orbits - in-phase and anti-phase. Further, the in-phase locking is unstable and the anti-phase locking is stable.

Proof : The proof can be divided in two steps - (a) There are only two fixed points of f - at 0 and at dv, and (b) $f'(0) > 1$ and $f'(dv) < 1$ which implies that the in-phase locking is unstable and anti-phase locking is stable.

The first part is proved as follows.

As λ_1 and λ_2 are negative, $x_1 > y_1$ and $dv - x_2 > dv - y_2$. And as $\beta > \alpha > \frac{2dv}{1-dv}$, $\frac{\alpha+2}{\beta+2}\frac{\beta}{\alpha} > 1$ and $\frac{\beta+2}{\alpha+2}\frac{\alpha}{\beta} < 1$. Also $\beta > \frac{2dv}{1-dv}$ implies $k_\beta > dv > y_2$. This gives us the following inequalities:

$$\left(\frac{2v_h - x_1}{2v_l + y_1}\right) \geq \left(\frac{x_1}{y_1}\right) \tag{5.12}$$

$$\textit{and } \left(\frac{k_\beta + x_2}{k_\beta - y_2}\right) \leq \left(\frac{dv - x_2}{dv - y_2}\right) \tag{5.13}$$

where the equality holds at the end points i.e. at $x_1 = 0$ and $x_1 = dv$ for (5.12) and at $x_2 = 0$ and $x_2 = dv$ for (5.13). At any fixed point for the return map f, $x_1 = y_2$ and $y_1 = x_2$ and equations (5.12) and (5.13) should be consistent with these fixed point equations. Substituting $x_1 = y_2$ and $y_1 = x_2$ in (5.12) and (5.13) we get:

$$dv - ((dv - y_1) + y_2) + \frac{2(dv - y_1)y_2}{dv + k_\beta} \geq 0 \tag{5.14}$$

$$dv - ((dv - y_1) + y_2) + \frac{(dv - y_1)y_2}{v_h} \leq 0 \tag{5.15}$$

These equations are consistent only when

$$(dv - y_1)y_2 \frac{2}{dv + k_\beta} \geq (dv - y_1)y_2 \frac{1}{v_h} \tag{5.16}$$

which in turn can be true only at the end points, i.e. $y_1 = 0$ or $y_1 = dv$, because $k_\beta < 1$. It can be confirmed that this is indeed the case by inspection of figure 5.9.

The second part of the proof is proved by calculating $f'(0) = f_1'(0) \cdot f_2'(0)$. $f_1'(0)$ and $f_2'(0)$ are calculated from (5.10) and (5.11) as:

$$f_1'(0) = \left(\frac{v_l}{v_h}\right)^q \tag{5.17}$$

$$f_2'(0) = \frac{k_\alpha + dv}{k_\alpha - dv} = \frac{k_\alpha + v_h - v_l}{k_\alpha - v_h + v_l} > \frac{v_h}{v_l} \tag{5.18}$$

where $q = \frac{\beta+2}{\alpha+2}\frac{\alpha}{\beta} < 1$ and $k_\alpha = \frac{\alpha}{\alpha+2}$. Also $\alpha > \frac{2dv}{1-dv}$ implies $k_\alpha > dv$. Hence

$$f'(0) = f_1'(0) \cdot f_2'(0) > \left(\frac{v_h}{v_l}\right)^{1-q} > 1 \tag{5.19}$$

And as f has no other fixed points between 0 and dv and f is continuous, $f'(dv) < 1$. Hence, proved.

It should be noted that this condition is not a strict bound but rather provides key design insights when a particular form of coupling (anti-phase) is sought[85].

CAPACITIVE, RESISTIVE COUPLING AND BISTABILITY The two extreme cases of purely resistive and purely capacitive coupling are of interest. In case of coupling using only a capacitor, the symmetric and identical coupled system always has a stable anti-phase and an unstable in-phase locking. This is because in case of purely capacitive coupling, $\beta \to \infty$ and so $\beta > \alpha$ for all finite α. Even in practical cases where some parasitic resistance is included in parallel with the coupling capacitor [63], β is typically much larger than α.

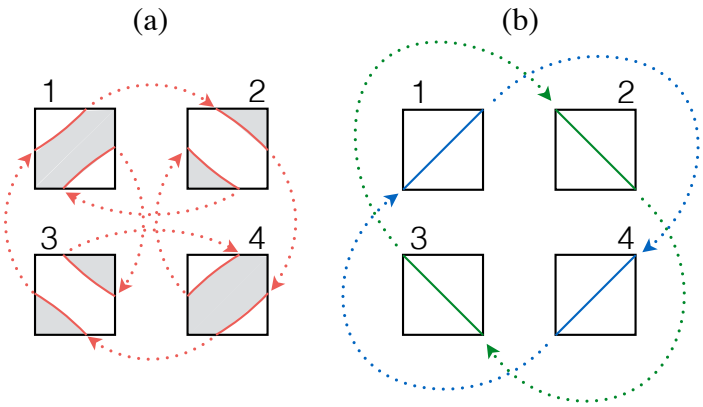

Figure 5.11: The trajectories (which are periodic orbits) corresponding to the fixed points in the return maps of figure 5.10b. (a) The unstable fixed point of figure 5.10b corresponds to two periodic orbits in the unreduced space as shown in red. (b) The fixed point at 0 corresponds to a single periodic orbit shown in blue and the fixed point at dv corresponds to the green periodic orbit. When the initial state of the system lies in the gray region (shown in (a)), the system settles down to an in-phase locking state, and otherwise to an anti-phase locking state

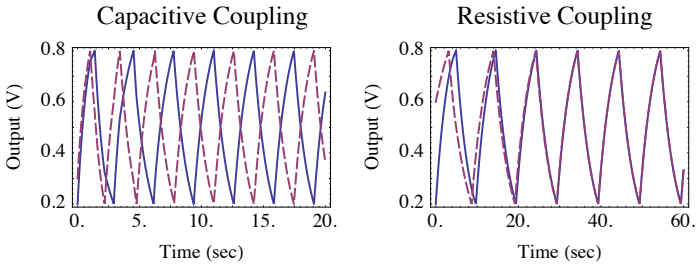

Figure 5.12: Capacitive coupling leads to anti-phase locking and resistive coupling leads to in-phase locking in case of symmetric D-D coupled oscillators. The solid and dashed lines represent output of the two oscillators.

Such anti-phase locking matches well with recent experimental findings of capacitively IMT coupled oscillators as discussed in [85]. In case of coupling using only a resistor, the symmetric and identical coupled system will have a stable in-phase and an unstable anti-phase orbit, as can be predicted from figure 5.13 for $\alpha \to \infty$. Time domain simulations of the coupled systems with purely capacitive and purely resistive coupling are shown in figure 5.12. The parameter values for capacitive coupling are $\alpha = 5$ and $g_{dm} = g_s = 6c_c$ and those for resistive coupling are $c = 13g_c$ and $\beta = 3.6$.

Figure 5.10 (b and c) show cases when $\beta < \alpha$. In the intermediate case when the return

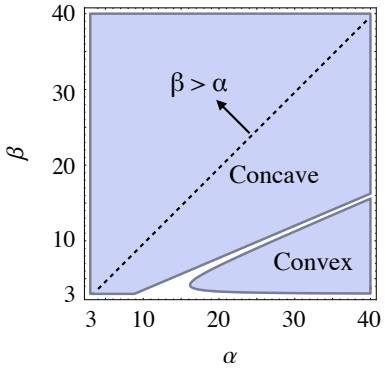

Figure 5.13: Return map type for the symmetric D-D case in the parametric space, $\beta \times \alpha$ for $v_l = 0.2$ and $v_h = 0.8$. We can clearly see that for $\beta > \alpha$ the return map is concave and anti-phase locking is stable. Also when the coupling is more resistive, the return map becomes convex with stable in-phase locking. The region between concave and convex return map is the region with S-shaped return map with both stable in-phase and stable anti-phase locking

map transitions from concave to convex, the system goes through a state where both in-phase and anti-phase locking are stable with one unstable fixed point in between (figure 5.10b). In figure 5.13 the two regions for concave and convex return map can be clearly seen. They are separated by a thin region which represents the case of bistability. Figure 5.14 shows the time domain simulation waveforms of oscillator outputs for $\beta = 3.6$ and $\alpha = 13.1$. We note that the initial voltage of the first oscillator is 0.2V and depending on the initial voltage of the second oscillator, the system can either lock in phase or out of phase. These design parameters correspond to a bistable system of the kind shown in figure 5.10b, and hence the final steady state locking is in-phase or out-of-phase depending on the initial phase of the system. When the initial phase (or output voltage) of oscillators are close to each other (represented by gray region in figure 5.11a) the system locks in-phase, and when they are far the system locks out-of-phase for the same circuit parameters.

5.1.2.3 *Asymmetric D-D oscillators*

Let us now investigate the case of D-D oscillator dynamics where the two oscillators are identical but the pull-up and pull-down devices are non-identical thereby giving rise to

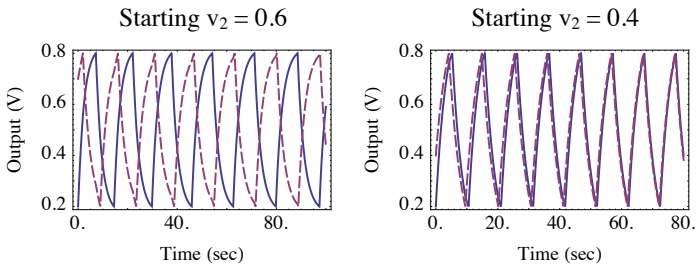

Figure 5.14: Simulation waveforms showing the dependence of final locking to the initial state of the system in the intermediate case of figure 5.10b when the return map is S-shaped. The solid and dashed lines represent the two oscillators. Initial $v_1 = 0.2V$ in both cases, but the system locks in-phase when initial $v_2 = 0.4V$, and anti-phase when initial $v_2 = 0.6V$. With reference to figure 5.11, the intial point $(0.2, 0.4)$ lies in the gray region and the point $(0.2, 0.6)$ lies outside the gray region in conduction state 1

asymmetric charging and discharging rates. As the the oscillators are identical, $\beta_{11} = \beta_{21} = \beta_c$ and $\beta_{12} = \beta_{22} = \beta_d$ where subscripts c and d stand for charging and discharging. The symmetry of the system (due to the identical oscillators) can be seen in the flows of the states. Flows of conduction states 1(00) and 4(11) are mirror images about the diagonal $x = y$ and the flow in conduction state 2(10) is equivalent to the flow in state 3(01) with axes x and y interchanged. This symmetry is also shown in the transitions between states. The system can be expressed after reducing the symmetry as in figure 5.15. For $\beta_c < \beta_d$, two kinds of cycles are possible in the regions $1 \to 2b \to 1$ and $1 \to 2c \to 4 \to 2a \to 1$. To find the fixed points of the system, we draw the return map with the bottom edge of state 1 as the Poincare section. Let f_1 be the mapping from bottom edge of conduction state 1 to its right edge, and f_{2a}, f_{2b} and f_{2c} are the mappings between edges in conduction state 2 as shown. Also, let $f_1(x'_k) = x_k$ and $f_{2b}(0) = y_k$ as shown in figure 5.16. For small asymmetries, the flows remain monotonic and also $y_k > x'_k$. Because it is a symmetry reduced space, we consider the first return map for trajectories of the type $1 \to 2c \to 4 \to 2a \to 1$ and the second return map for trajectories of the type $1 \to 2b \to 1$. Then the return map f is given by:

$$f(x) = \begin{cases} f_1 \circ f_{2c} \circ f_4 \circ f_{2a}(x), & 0 \le x < x'_k \\ f_1 \circ f_{2b} \circ f_1 \circ f_{2b}(x), & x'_k \le x < dv \end{cases} \tag{5.20}$$

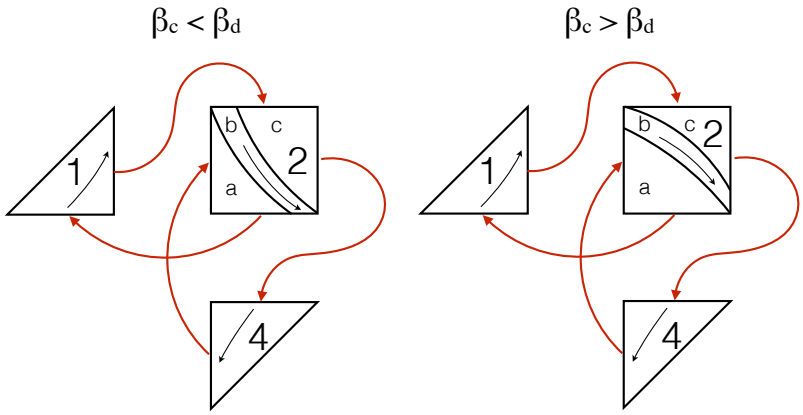

Figure 5.15: Symmetry reduced space in the asymmetric D-D configuration with $\beta_c > \beta_d$ (left) and $\beta_c < \beta_d$ (right). Such configuration will have only a single symmetry. The flow matrices in the four conduction states are not equal and hence states cannot be represented in a single combined state space with a single fixed point as was done in the symmetric D-D case ($\beta_c = \beta_d$)

Proposition 2 : *Sufficient conditions for existence of stable periodic orbit in asymmetric D-D coupled oscillator system:* If in a D-D asymmetric coupled oscillator system the asymmetries are small enough such that the flows are monotonic and $y_k > x'_k$, then the following are true about the return map f on the bottom edge of state 1:

1. f is continuous
2. $f'(0) > 1$ for $\beta_c > \alpha$ and $\beta_d > \alpha$
3. f has one fixed point at 0 and at least one in the interval $x'_k < x < dv$ at, say, x_f
4. Either the fixed point at x_f is stable, or there exists a stable fixed point at x'_f where $0 \leq x'_f < x_f$

Proof : (a) The return map is separately continuous in intervals $[0, x'_k)$ and $(x'_k, dv]$ as it is a composition of mappings of continuous flows. The continuity of f at x_k can be established by considering two points close to x'_k on either side. From (5.20) we can see that $f(x'_{k+}) = f(x'_{k-}) = y_k$, and hence f is continuous at x_k .

(b) It can be proved by similar procedure as adopted before in *Proposition 1* that $f'(0) = f'_1(0) \cdot f'_{2c}(dv) \cdot f_4(0) \cdot f'_{2a}(0) > 1$ for $\beta_c > \alpha$ and $\beta_d > \alpha$.

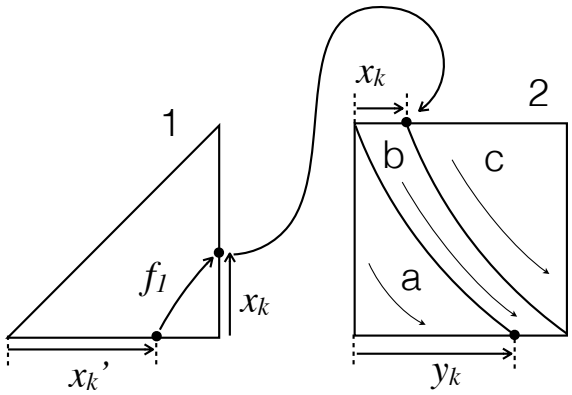

Figure 5.16: Diagram of symmetry reduced state spaces for conduction states 1 and 2 in the asymmetric D-D configuration. In conduction state 2, the top-left corner does not map to the bottom-right corner as was the case in the symmetric D-D case. The width of this middle region where the flow maps the top edge to the bottom edge is defined using x_k and y_k

(c) The fixed point at 0 can be seen clearly in the flow diagram. In interval $x_k' < x < dv$, the fixed points of first return $f_1 \circ f_{2b}$ will also be the fixed points of second return (which is f), but not the other way around. Now $f_1 \circ f_{2b}(x_k') = dv$ and $f_1 \circ f_{2b}(dv) = y_k$. As $f_1 \circ f_{2b}$ is continuous, and hence decreasing, in the interval $x_k' < x < dv$, there exists a fixed point for $f_1 \circ f_{2b}$, and hence for f, in the interval $x_k' < x < dv$.

(d) As f is continuous and has fixed points at 0 and x_f, one of these two should be stable if there is no other fixed point in between 0 and x_f. If they both are unstable, then a stable fixed point exists in the interval $(0, x_f)$. Hence proved.

Figure 5.17 shows a representative return map for the asymmetric D-D configuration. The poincare section chosen in the symmetric D-D case was the left edge of conduction state 1. Due to symmetry, the left edge of conduction state 1 is same as the bottom edge of conduction state 1. Hence the return maps in the symmetric D-D case can be compared with the return maps in the asymmetric D-D case as if they were drawn on the same edge. Figure 5.18 shows a comparison of the return maps of a symmetric case ($\beta_c = \beta_d = 60$, $\alpha = 10$) with that of two asymmetric cases ($\beta_c = 50 \, and \, 40$, $\beta_d = 60$, $\alpha = 10$). The corresponding time domain waveforms and phase plots are shown in figure 5.19. The figure clearly shows

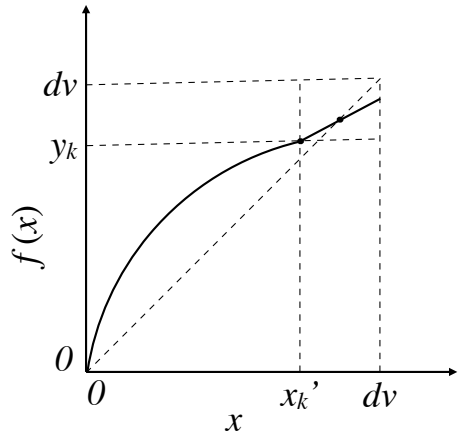

Figure 5.17: Representative plot of the return map on the bottom edge of conduction state 1 in the asymmetric D-D case. The fixed point corresponding to anti-phase locking which was at dv in the symmetric case is shifted inside away from dv in the asymmetric case

that the steady state periodic orbit changes from a diagonal (perfect anti-phase locking) to a butterfly shaped curve (imperfect anti-phase locking) as the asymmetry increases. However, the time domain waveforms for butterfly shaped periodic orbits would still be very similar in appearance to anti-phase locking. The fixed point close to dv in the return map shifts away from dv as the difference between β_c and β_d increases. This trend can be seen in figure 5.20 which shows the movement of the anti-phase fixed point with $\beta_d - \beta_c$ for fixed $\beta_d = 60$ and $\alpha = 10$. For $\beta_c > \beta_d$, the cycles will be of the type $4 \to 2b \to 4$ and $1 \to 2c \to 4 \to 2a \to 1$, and the return map will have to be drawn on an edge of state 4. The return map in this case will be analogous to the $\beta_c < \beta_d$ case with β_c and β_d interchanged.

5.1.3 *D-R oscillators*

5.1.3.1 *Modeling*

In case of coupled D-R oscillators, arguments similar to the previous case lead to the same matrix equation as (5.4):

$$x'(t) = -\frac{g_c}{c_c} F^{-1} A(s) \left(x(t) - A^{-1}(s) P(s) \right) \tag{5.21}$$

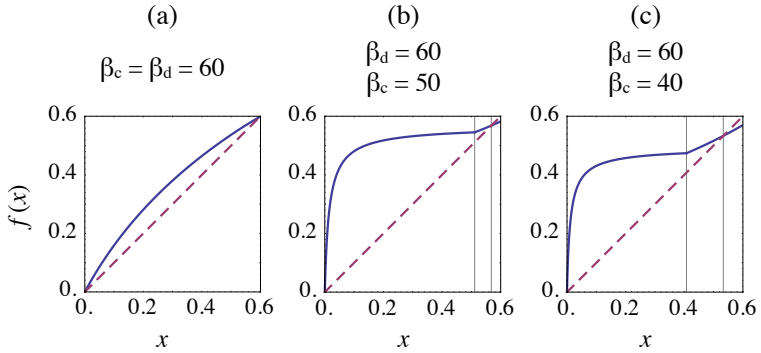

Figure 5.18: Comparison of return maps in the symmetric (a) and asymmetric (b and c) D-D configurations for constant $\alpha = 10$. Both symmetric and asymmetric configurations have a fixed point at 0 corresponding to in-phase locking (which is unstable here as $\beta > \alpha$ condition is satisfied) along with another fixed point, which in symmetric case, is at dv (perfect anti-phase locking) but in asymmetric case shifts away from dv

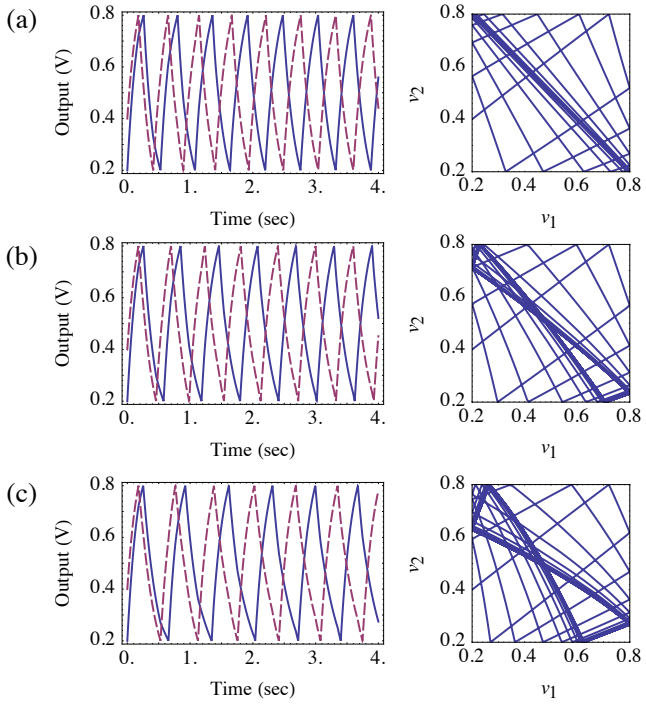

Figure 5.19: Time domain waveforms and phase plots corresponnding to the configurations in figure 5.18(a, b and c). The steady state periodic orbits can be seen clearly in the phase plots to transform from a diagonal (perfect anti-phase locking) in the symmetric case (a) to a butterfly shaped curve (imperfect anti-phase locking) as the asymmetry increases and the anti-phase fixed point in the return map shifts away from dv

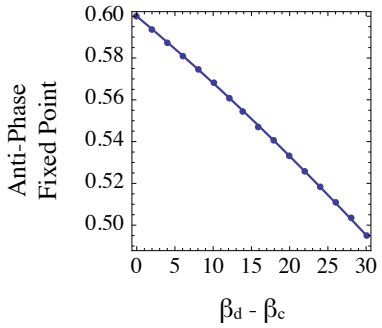

Figure 5.20: Numerical simulations illustrating the fixed point close to dv shifts away from dv with increasing difference between β_c and β_d in the asymmetric case

where matrices F and P remain the same as before but matrix A changes to the following:

$$F = \begin{bmatrix} 1+\alpha_1 & -1 \\ -1 & 1+\alpha_2 \end{bmatrix} \tag{5.22}$$

$$\begin{aligned} A(00) &= \begin{bmatrix} -\beta_1 - \beta_{s1} - 1 & 1 \\ 1 & -\beta_2 - \beta_{s2} - 1 \end{bmatrix}, & P(00) &= \begin{bmatrix} \beta_1 \\ \beta_2 \end{bmatrix} \\ A(10) &= \begin{bmatrix} -\beta_{s1} - 1 & 1 \\ 1 & -\beta_2 - \beta_{s2} - 1 \end{bmatrix}, & P(10) &= \begin{bmatrix} 0 \\ \beta_2 \end{bmatrix} \\ A(01) &= \begin{bmatrix} -\beta_1 - \beta_{s1} - 1 & 1 \\ 1 & -\beta_{s2} - 1 \end{bmatrix}, & P(01) &= \begin{bmatrix} \beta_1 \\ 0 \end{bmatrix} \\ A(11) &= \begin{bmatrix} -\beta_{s1} - 1 & 1 \\ 1 & -\beta_{s2} - 1 \end{bmatrix}, & P(11) &= 0 \end{aligned} \tag{5.23}$$

Here $\beta_i = g_{idm}/g_c$ and $\beta_{si} = g_{si}$.

For all numerical simulations in the rest of the paper, the normalized values of v_l and v_h w.r.t v_{dd} are chosen to be 0.2 and 0.8 respectively.

5.1.3.2 *Limit cycle behavior*

In this section we consider the dynamics of a D-R coupled system. This is of interest because of its ease of fabrication, relaxed conditions for oscillations and already published reports of such coupled oscillatory systems [63]. We consider coupling of identical oscillators and hence we define $\beta_1 = \beta_2 = \beta$ and $\beta_{s1} = \beta_{s2} = \beta_s$. Unlike the D-D coupled oscillator case, the notion of symmetric charging and discharging does not apply in D-R coupled oscillator case because the circuit by construction is different for charging and discharging. During charging a part of the net charging current charges up the output capacitor whereas the rest of it flows through the pull-down resistance to ground. The process of discharging has no such leakage component. In terms of the conductance ratio β, this can be explained by the fact that the net charging component in the matrix A is $(\beta + \beta_s)$ and it is always greater than the discharging component β_s. However, the flows can still be simplified for analysis as was described in section 5.1.1. The simplification assumes that the flows are monotonic in the regions of operation in all four conduction states, but the direction of monotonicity is different from the D-D coupled oscillator case as shown in figure 5.3. For our analysis, a particular type of non-monotonicity is allowed in state 2 (and state 3) as shown in figure 5.21. Here the fixed point for conduction state 2 satisfies the condition of oscillation shown in figure 5.4, but the flow in state 2 as shown in the symmetry reduced space (figure 5.21) is non monotonic. We will consider the case of identical oscillators , and following the methodology of the asymmetric D-D case, we can reduce the symmetry of identical oscillators as shown in figure 5.21. In this case, two kinds of cycles are possible - $4 \rightarrow 2b \rightarrow 4$ and $4 \rightarrow 2c \rightarrow 4a \rightarrow 4$. To find the fixed points of the system, we draw the return map on the top edge of conduction state 4 as the Poincare section. Let f_4 be the mapping from top edge of state 4 to its left edge, f_{4a} be the mapping from the extended right edge of state 4 to its top edge, f_{2a}, f_{2b} and f_{2c} be the mappings between edges of state 2. Also let $f_4(x'_k) = x_k$ and $f_{2b}(0) = y_k$ as shown in figure 5.22. We consider the scenario when the flows of the system are as shown in figure 5.21 and $y_k > x'_k$. Because

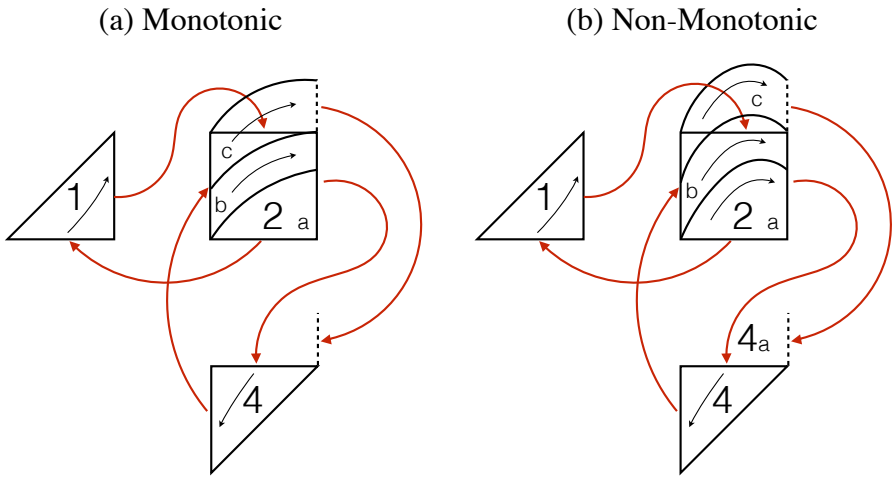

Figure 5.21: Symmetry reduced space in the D-R coupled oscillator system. There is only a single symmetry due to identical oscillators

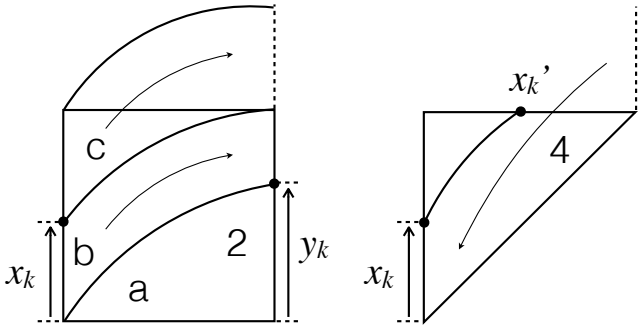

Figure 5.22: Symmetry reduced space for the D-R coupled oscillator system in states 1 and 4 with the definition of x_k, x_k' and y_k. f_4 is the mapping from top edge of state 4 to left edge of state 4 and f_{2a}, f_{2b} and f_{2c} are mappings between edges of state 2 as shown

it is a symmetry reduced space, we will have to consider the second return map for cycles of the type $4 \to 2b \to 4$ but only the first return map for $4 \to 2c \to 4a \to 4$ type cycles. Then the return map f is given by:

$$f(x) = \begin{cases} f_4 \circ f_{2c} \circ f_{4a}(x), & 0 \le x < x_k' \\ f_4 \circ f_{2b} \circ f_4 \circ f_{2b}(x), & x_k' \le x < dv \end{cases} \tag{5.24}$$

Proposition 3 : *Sufficient conditions for existence of stable periodic orbit in D-R coupled oscillator system:* If in a D-R coupled oscillator system, the flows are as shown in

figure 5.21 and $y_k > x'_k$ then the following are true about the return map on the top edge of state 4 in the symmetry reduced state space (figure 5.21)

1. f is piece-wise continuous with discontinuity at x'_k. Moreover, $f(x'_{k+}) = y_k$ and $f(x'_{k-}) = dv$.

2. f has at least one fixed point in the interval $x'_k < x < dv$ at, say, x_f

3. f has at least one stable fixed point in the interval $x'_k < x < dv$

Proof : (a) The argument is the same as in *Proposition 2.* The return map is separately continuous in intervals $[0, x'_k)$ and $(x'_k, dv]$ as it is the composition of continuous flows. From (5.24) we can see that $f(x'_{k+}) = y_k$ and $f(x'_{k-}) = dv$.

(b) In the interval $x'_k < x < dv$, the fixed points of the first return map $f_4 \circ f_{2b}$ will also be the fixed points for its second return map (which is f). Now $f_4 \circ f_{2b}(x'_k) = dv$ and $f_4 \circ f_{2b}(dv) = y_k$. As $f_4 \circ f_{2b}$ is continuous (and hence decreasing) in this interval, there exists a fixed point for $f_4 \circ f_{2b}$, and hence f, in the interval $x'_k < x < dv$.

(c) As $f(x'_{k+}) = y_k$, f is continuous in the interval $x'_k < x < dv$ and f has a fixed point at x_f where $x'_k < x_f < dv$, hence either the fixed point at x_f is stable or there exists another fixed point in the interval $x'_k < x < x_k$ which lies in $x'_k < x < dv$. Hence proved.

Figure 5.23 shows the return map f on the top edge of state 4 for the D-R coupled oscillator system for varying β_s. The return maps in the figure have a single stable fixed point at x_f in the interval $x'_k < x < dv$. The movement of the fixed point x_f with β_s is shown in figure 5.24.

Another important design consideration for the coupled oscillator system, is the role of the coupling circuit on the overall system dynamics, as is seen in figure 5.25. We note that as the value of α increases the phase diagram in the $v_1 \times v_2$ plane shows strong sensitivity. In particular, for low values of α, the system shows in-phase locking. As α increases (for intermediate value of α), the butterfly shaped phase plot widens and the system exhibits a non-monotonic decrease in the output voltages, v_1 and v_2 from v_h to v_l. This can also

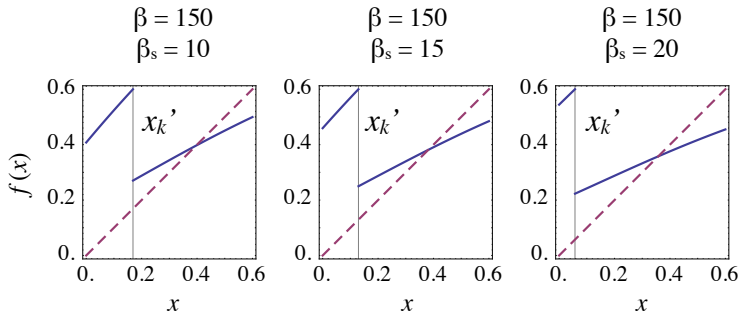

Figure 5.23: Return map on the top edge of state 4 for the D-R coupled oscillator system for $\alpha = 1$, $\beta = 150$ and βs values of 10, 15 and 20

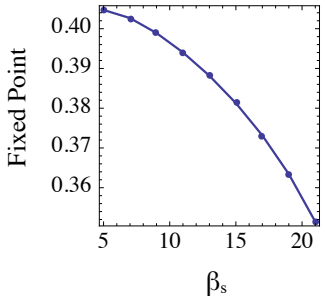

Figure 5.24: Movement of the fixed point x_f for fixed $\alpha = 1$, $\beta = 150$ and varying β_s for the return map on the top edge of state 4 for the D-R coupled oscillator system

be seen in the time domain waveforms where the output voltages first decrease to an intermediate voltage, then increase and again decrease; clearly demonstrating four possible conduction states (MM, MI, IM and II) in both phase and time domain plots. Finally, for high values of α the butterfly in the phase plot opens even further, thus making the decrease of output voltages from v_h to v_l more monotonic and the system tends to anti-phase locking, as exhibited in both phase and time (figure 5.25).

5.1.4 *D-MOSFET oscillators*

5.1.4.1 *Modeling*

When two D-MOSFET type relaxation oscillators are coupled electrically, their phase dynamics would evolve over time till a steady state is reached. The system we consider consists of two relaxation oscillators that are coupled using a capacitor c_c. The equation of

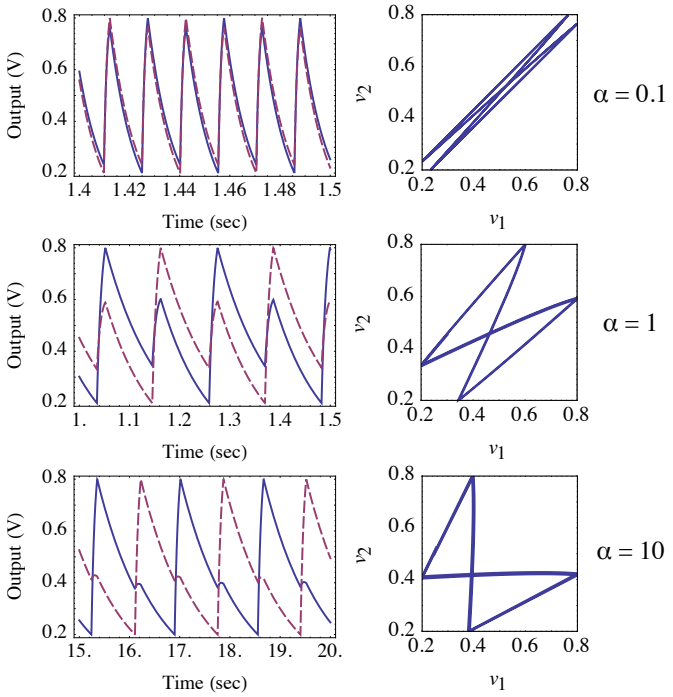

Figure 5.25: Steady state waveforms and phase trajectories for the D-R coupled oscillator system with $\alpha = 0.1$ (top), $\alpha = 1$ (middle) and $\alpha = 10$ (bottom). The solid and dashed lines represent the two oscillators.

the system of coupled oscillators is given by:

$$c_c \begin{bmatrix} \alpha_1 + 1 & -1 \\ -1 & \alpha_2 + 1 \end{bmatrix} \begin{bmatrix} v_1' \\ v_2' \end{bmatrix} = \begin{bmatrix} -g_1(s_1)\, v_1 \\ -g_2(s_2)\, v_2 \end{bmatrix} + \begin{bmatrix} p_1(s_1) \\ p_2(s_2) \end{bmatrix}$$

where $g_i(s_i)$ and $p_i(s_i)$ are as defined above for each oscillator and α is the ratio $\frac{c_1}{c_c} = \frac{c_2}{c_c}$. We start by defining the state space of the coupled system. At any time, the state of the system is characterized by (v_1, v_2, s_1, s_2). s_1 and s_2 take only 2 values each – charging and discharging, as explained before, and v_1 and v_2 vary between v_l and v_h. As we did with previous configurations, we can represent the state space as 4 regions of 2 dimensional state spaces corresponding to 4 combinations of phases of the two devices – MM (metallic-metallic), MI (metallic-insulating), IM (insulating-metallic) and II (insulating-insulating) (figure 5.6). It is assumed that the parameters are varied in a way that the flows in all the states remain monotonic in the direction as shown. This monotonicity condition guarantees

oscillations of both oscillators in steady state and can be considered as an extension of the previous condition for oscillation in case of a single oscillator. As the flow is linear in all the 4 regions of the state space, there is a single fixed point in all states. The fixed points for regions MM and II are shown in figure 5.6. Due to symmetry in region MM, if the system starts from bottom left corner, it ends in the opposite corner and the flow is symmetric along the diagonal line as shown. Such symmetry is possible in state II only when $v_{gs1} = v_{gs2}$.

5.1.4.2 *Limit cycle behavior*

When two D-MOSFET type oscillators are coupled, the system is expected to lock when the individual frequencies of oscillators are close. For identical oscillators, closer frequencies correspond to close values of the corresponding v_{gs}. The mechanism of locking, however, is different from the mechanism by which coupled sinusoidal oscillators lock. The locking range in terms of v_{gs}, i.e. the range of v_{gs} for which the system locks and settles to a stable periodic orbit in steady state, is depicted in figure 5.26. Locking is determined by monitoring the waveforms of both oscillators to see if the time difference in their successive peak values become constant after a while or not. The locking range of figure 5.26 describes the region of a single rational rotation number and the region outside describes irrational or other rational rotation numbers [84]. The steady state periodic orbits of the coupled system for $v_{gs1} = 0.3$ and varying v_{gs2} are shown in figure 5.27. As can be seen, the system has a butterfly shaped stable orbit when v_{gs} values are close, which transitions into a rectangular orbit as v_{gs} values diverge and finally the system ceases to lock after a certain point. The symmetric butterfly curve is along the diagonal that corresponds to out-of-phase oscillation of the oscillators in time domain. As the system moves away from symmetry, the phase difference between the oscillators in time domain reduces but breaks synchronization much before reaching in-phase locking state.

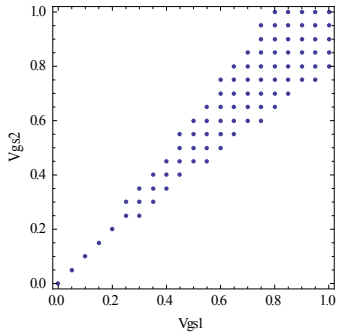

Figure 5.26: Region in the (v_{gs1}, v_{gs2}) plane for which the coupled system locks. Locking range is larger for larger v_{gs} values

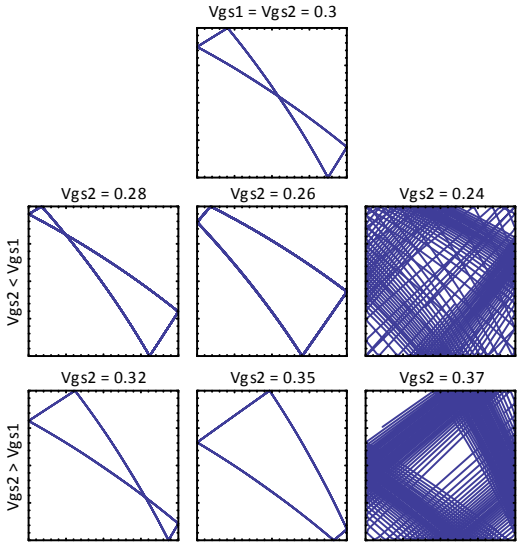

Figure 5.27: Steady state orbits in the state space of the coupled system for fixed $v_{gs1} = 0.3$ and varying v_{gs2}. When both v_{gs} values are equal, the stable periodic orbit is butterfly shaped along the diagonal that correspond to out-of-phase locking. As the difference in the v_{gs} values increase, the periodic orbit slowly changes to rectangular and finally breaks synchronization after a point.

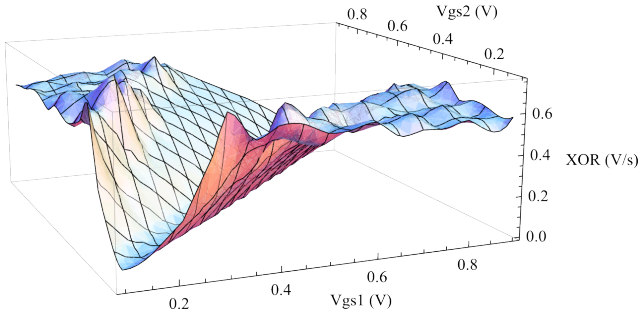

Figure 5.28: XNOR output as a function of v_{gs1} and v_{gs2}. The surface of the plot resembles some parabola or some even power of $(v_{gs1} - v_{gs2})$ in the locking range and settles to a value around 0.5 outside the locking region.

5.1.5 *Computational applications: Analog subtraction*

D-R type oscillators (including D-MOSFET) are suited for computing applications as they can be implemented in practice. D-D oscillators need stringent operating conditions and as such are not suitable for realiazing in real hardware. In coupled D-R oscillators, the trajectories in the phase space can be used to capture the difference in the values of v_{gs1} and v_{gs2} using an averaged XNOR measure on the output waveforms. The averaged XNOR measure is defined as first thresholding the output to binary values, second applying XNOR operation on these binary values at every time instant and finally averaging this XNOR output over some time duration. The averaged XNOR output for various v_{gs} values is shown in figure 5.28. We can make the following observations from it:

- It has the least value when $v_{gs1} = v_{gs2}$
- Within the locking range, it rises as an even function of $\left(v_{gs1} - v_{gs2}\right)$ resembling a parabola
- Outside the locking range, it averages to about 0.5
- The selectivity is better at lower v_{gs} values and the XNOR output becomes less selective as v_{gs} values increase

These characteristics of the curve can be explained by realizing that the averaged XNOR

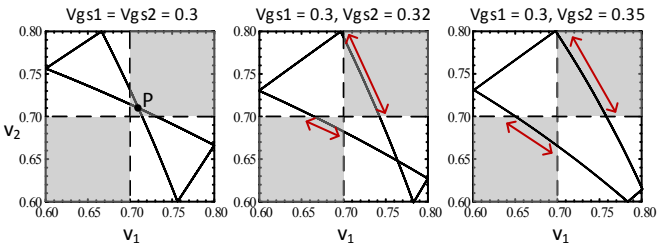

Figure 5.29: Plots showing the relation between XNOR output and the steady state periodic orbit of the system. XNOR operation at a time instant is 1 in the grey region determined by the thresholds on respective voltages. Averaged XNOR output is equal to the fraction of time spent by the system in the grey regions. XNOR output is minimum in case of a butterfly shaped orbit and increases as the orbit transitions to a rectangular orbit.

measure by construction is equal to the fraction of the time the system spends in the grey region (region where XNOR output is 1, and is determined by the thresholds on v_1 and v_2) in steady state (figure 5.29). It can be seen that the XNOR measure should have the least value in the symmetric case when the system locks out-of-phase and should increase as v_{gs} values diverge. The thresholds on v_1 and v_2 can be chosen corresponding to point P which gives 0 XNOR measure in the symmetric case. Also the XNOR output averages to around 0.5 outside the locking region as the system does not lock and the trajectories visit the grey and white regions almost equally.

A time domain interpretation can also be given for explaining the nature of the XNOR surface of figure 5.29. The XNOR operation can also be thought of as a measure of phase difference between the oscillators, and according to the arguments before, the system locks out-of-phase when the gate voltages are equal, and hence XNOR value is minimum in this case. Also the XNOR output should increase as the phase difference reduces when v_{gs} values diverge.

Such oscillatory subtractors can have many advantageous applications. Firstly, they would be noise tolerant as they work on fixed-point or attractor dynamics. Secondly, their compact size would enable building arrays of such subtractors which can be used in parallel distributed computing architectures within the sensors, like cameras for pixel-wise subtraction. An application is template matching for cases where element-wise compar-

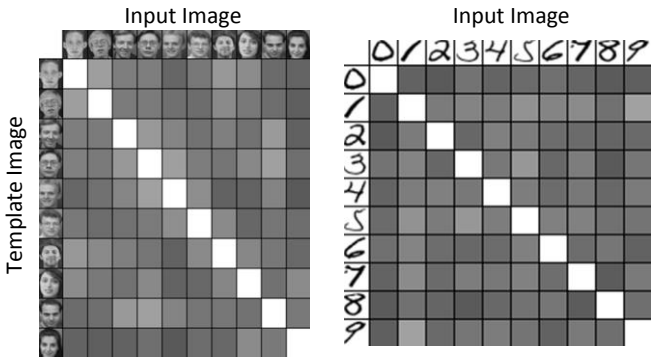

Figure 5.30: Averaged XNOR outputs for comparing faces (left) and handwritten number patterns (right) to stored template patterns using arrays of coupled VO_2 oscillators. Grey shade corresponds to fraction of pixels with positive match, white being the highest.

isons suffice to decide a match. We demonstrate this by comparing images of faces and hand-written numbers. We first use the XNOR measure for each pixel and calculate the number of pixels with XNOR output below a threshold value v_{thXOR}. Figure 5.30 shows the results of comparing faces with an oscillatory subtractor, where the grey shade corresponds to the fraction of pixels with positive match, white being the highest. Such system followed by a winner-take-all (WTA), i.e. a threshold on the number of pixels that give a positive match, can be used to decide if the input image matches a stored template pattern. The value of v_{thXNOR} is chosen around 0.2 considering the minimum values of the XNOR surface in the operating range of v_{gs} values. The two thresholds described above depend on different factors. The threshold of the number of pixels for WTA would depend on the database and the error statistics required or estimated. On the other hand, v_{thXOR} would be decided more by the nature of the XNOR surface (figure 5.28) and its minimum values.

5.1.5.1 *Variations and mismatches*

As the XOR measure is a DC measure and because the system has fixed point dynamics, temporal noise should not affect the steady state output. Hence, we restrict ourselves to variations in the form of mismatches in the device parameters c, g of the IMT devices and v_t of the series transistors. Figure 5.31 shows the effect of parametric mismatches on

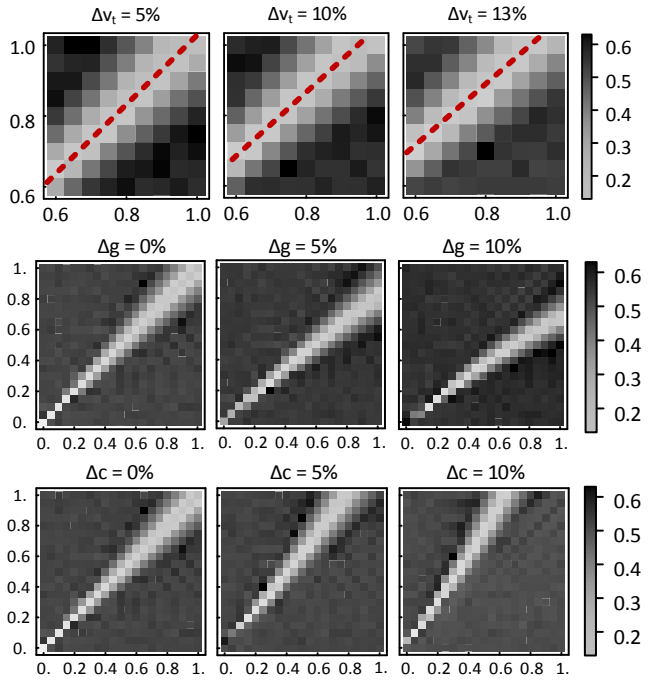

Figure 5.31: XNOR output as a function of v_{gs}values and its sensitivity to mismatch in v_t of the series transistor (top), IMT device conductance g (middle) and IMT device internal capacitance c (bottom). Averaged XNOR output is much more susceptible to device parameters at higher v_{gs} values.

the XOR output. The coupled system is much more sensitive to the device parameters – internal capacitance c and metallic phase conductance g, than the threshold voltage v_t of the series transistor. Value of v_t is varied around 0.3, normalized to v_{dd}. Also the effect of mismatches is more for higher v_{gs} values, which implies that deciding the operating v_{gs} range, apart from operating in the saturation region, will also have a trade-off in terms of combatting parametric mismatches. Larger overdrive voltages would reduce the effect of v_t variation, but would be more affected by the variations in the IMT device parameters.

5.1.6 *A note on stability*

For sustained oscillations, the fixed points of the flows should lie outside the region of operation in all the three cases discussed. When fixed points come inside the region of operation, the oscillations would stop and the system settles at the fixed points. In the case of sustained oscillations, the symmetric D-D coupled oscillator system always has

monotonic flows and a stable periodic orbit. For the other two cases of asymmetric D-D and D-R coupled oscillator systems, some sufficient conditions for stability have been discussed in the previous sections - monotonic flows and $y_k > x'_k$. But when these conditions are not met, the system might not have a stable periodic orbit. For asymmetric D-D coupled oscillator case, the conditions of monotonicity and $y_k > x'_k$ hold for small asymmetries, i.e. small difference between β and β_s. For large asymmetries, these conditions might not hold. In such cases, the system might have periodic orbits with more than 4 transitions per period or no periodic orbit with irrational rotation numbers [84]. On the other hand, in the D-R coupled oscillator case, the conditions of monotonicity and $y_k > x'_k$ hold for large differences in β and β_s and might show irrational rotation numbers otherwise.

5.1.7 *Experimental demonstrations*

An IMT device can be realized using VO_2 (Vanadium dioxide) which exhibits unique electronic properties like metal-insulator phase transitions. VO_2 has been shown to undergo abrupt first order metal-to-insulator and insulator-to-metal transitions with upto five orders of change in conductivity[86] and ultra-fast switching times [61]. Transitions have been shown to be electrically driven, thermally driven or a combination thereof. Recent work shows that for such a transition, a metallic filament structure is formed which acts as a conduction pathway in the low resistance state of VO_2 [87]. Also, a series circuit of VO_2 with a resistive pull down network has been shown to exhibit self-sustained electrical oscillations[63] when conditions of oscillations as described above are met. Moreover, two such relaxation oscillators can be electrically coupled to produce synchronized oscillations [63].

For experimental validation, we apply our models of coupled relaxation oscillators on a system of two coupled VO_2 oscillators. Figure 5.32 shows a schematic representation of the coupled circuit with a parallel resistance (R_C) and capacitance (C_C) as the coupling circuit. Frequency domain results of this system have been previously reported [63] show-

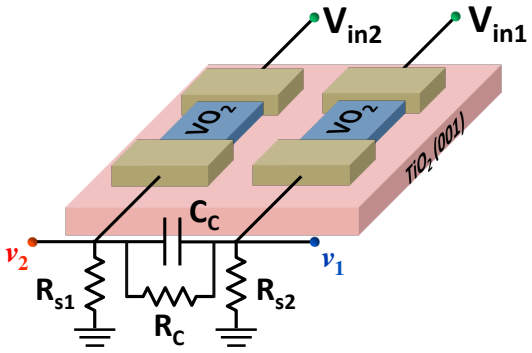

Figure 5.32: Schematic of the experimental setup of coupled VO_2 oscillators, with series resistances R_{s1} and R_{s2} respectively, coupled using a parallel $R_C - C_C$ circuit

ing a close match between experiments and theoretical results of a D-D model; and are not reproduced here. Using the D-R model developed in this paper, we obtain close match in the time-domain and phase plots of the oscillator system as well. With proper calibration of the system parameters, the D-R model described above shows very close qualitative match with experimental results. One such experimental result has been shown in figure 5.33 along with model prediction. This validation of the proposed models enables further design of experiments. It further models and explains both qualitative and quantitative the role of the system design parameters on the rich synchornization dynamics.

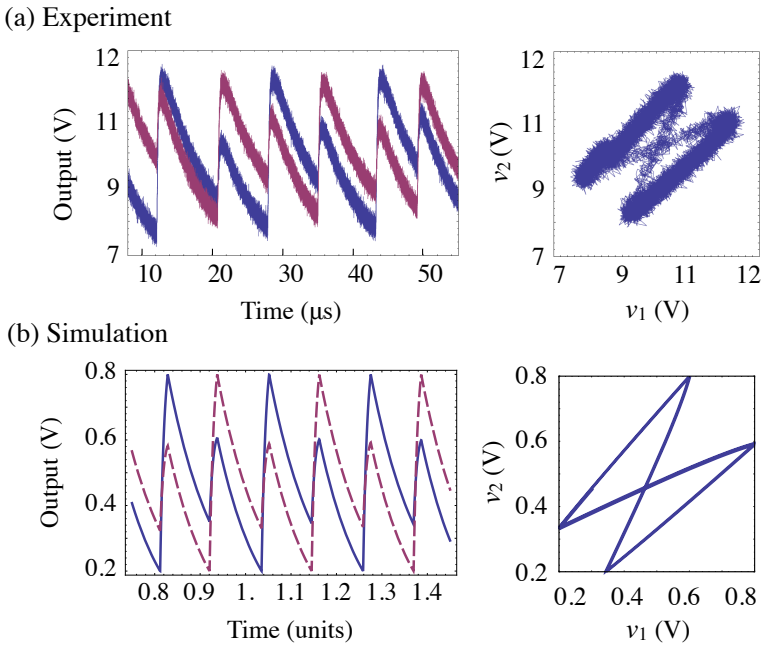

Figure 5.33: Experimental and simulated time domain waveforms in the steady state and phase plots for a parallel $R_C - C_C$ coupled oscillator system. The D-R coupled relaxation oscillator model is used for model development and simulation. The two waveforms show close match and validate the model prediction.

Chapter 6

NETWORK COUPLING AND GRAPH COLORING

6.1 PRIOR STUDIES

First let us define the concept of network coupling. Previously we have seen how two oscillators, when connected through some coupling circuit, can affect each others oscillations and eventually synchronize to a specific limit cycle behavior. In network coupling, multiple oscillators are connected to each other, and as such they all affect the oscillation behavior of all other connected oscillators. In these cases, even though a single coupling circuit (a capacitor, or a resistor) connects only two oscillators, we cannot study the behavior of the circuit by studying such pairs of oscillators separately, but the whole network circuit needs to be analyzed as a whole.

In this work, the reasons to understand network coupling behavior of oscillators are two fold:

1. Understand the computational abilities of such oscillators
2. Implement such coupled oscillators in hardware for the next generation of computing machines

Most of the prior work on network dynamical systems have been done in physics, esp. in analysis of lattice models, and computational neuroscience, for analysing network of coupled neurons. Unfortunately, almost all the prior work related to coupled oscillators, or network dynamical systems, have achieved only one of the above objectives, but failed to achieve both. Theoretical works which could analyse the network behavior, and in some case connect to computing applications, relied on oscillator models which could not be realized in hardware. In experimental work where such oscillators were realized in hardware, coupling two or more oscillators in some desired or useful way have always been

a challenge. Below is a brief review of some prior work regarding network coupling of oscillators.

6.2 THIS WORK

In this work, we establish that a system of coupled relaxation oscillators fabricated using Vanadium dioxide (VO_2) metal-insulator-transition devices and coupled capacitively, can lead to system dynamics on which vertex coloring of unweighted and undirected graphs (hitherto referred to as the graph coloring problem) can be successfully mapped (figure 6.1a). We demonstrate experimentally and using simulations that when such relaxation oscillators are coupled using only capacitances in a manner topologically equivalent to an input graph, their steady state phases can be used to approximate the solution of the NP-hard *minimum graph coloring problem*. For this, we propose a reformulation of the graph coloring problem where instead of finding a color assignment for each node, the objective is to find a circular ordering or circular permutation of the nodes such that the same colored nodes appear together in the ordering. Such a reformulation preserves the hardness of the problem and is useful for interpreting the output of our circuit (figure 6.1a). We show analytically that the dynamics of such a coupled relaxation oscillator system is intrinsically connected to spectral algorithms for graph coloring [88–90], which use eigenvectors of adjacency matrix of the input graph to approximate the solutions. Alternatively, the permutation of steady state phases of coupled relaxation oscillators depends on eigenvectors of the adjacency matrix in the same way as have been used by spectral algorithms for graph coloring (figure 6.1b). A programmable circuit for a such a coupled oscillator system, where the oscillators are coupled in a graph with adjacency matrix A and coupling capacitance matrix C_c is shown in figure 6.2. Our simulation results show that the hardness of problem instances has, on average, expected effects on important metrics of solutions found using such a circuit like the number of colors detected and the settling time.

It is well known that eigen properties of the coefficient matrix in the evaluation equation

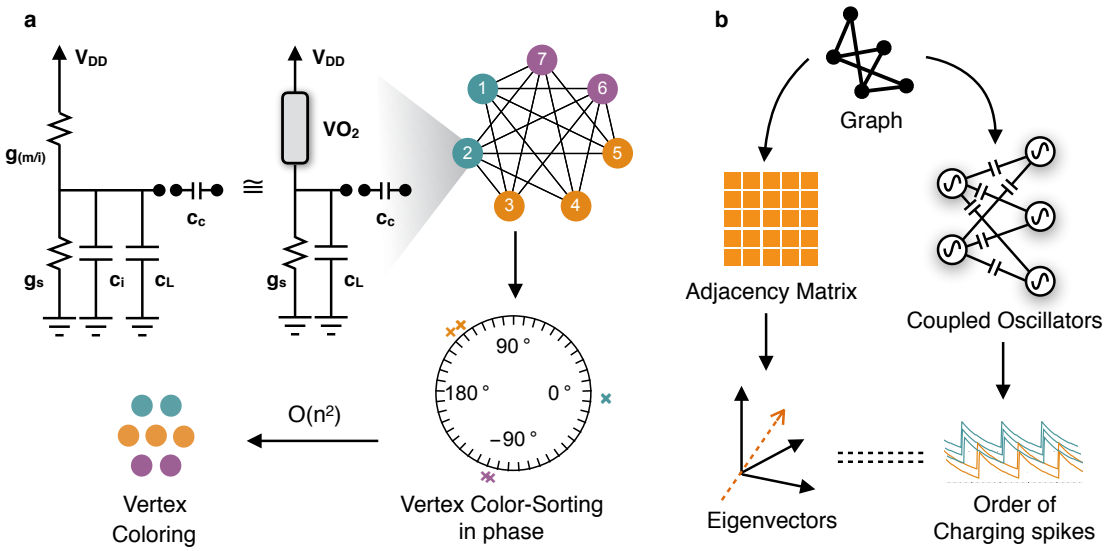

Figure 6.1: (a)Overview of the proposed system for vertex coloring and a simulation example. First step is a coupled relaxation oscillator circuit where the oscillators are composed of a series combination of VO_2 device and a resistor (with a loading capacitor in parallel), and are connected in a graph using capacitors. The equivalent circuit diagram of the VO_2 oscillator is shown using an internal capacitance c_i and a phase changing conductance $g_{d(m/i)}$ which switches between metallic conductance g_m and insulating conductance g_i. An example 3-partite graph is simulated and the relative phases of these oscillators are shown in a phase diagram which shows vertex color-sorting in phase, and can be used to calculate vertex-coloring with $O(n^2)$ complexity. (b) The circuit is composed of VO_2 oscillators capacitively coupled in a network same as the input graph. The final order of phases, or charging spikes, of the oscillators is related to the eigenvectors of the adjacency matrix of the input graph which in turn are related to the solution of the graph coloring problem.

of a dynamical system determine important structural properties of the system including stability, bifurcation, energy minima(s) and overall system dynamics. Here, we provide a theoretical bridge and experimental evidence that a dynamical system whose coefficient matrix inherits properties of the incidence matrix of a graph, can indeed emulate spectral graph algorithms just through its time evolution. We envision such dynamical systems to provide foundational paradigms in the development of next-generation computational accelerators and kernels.

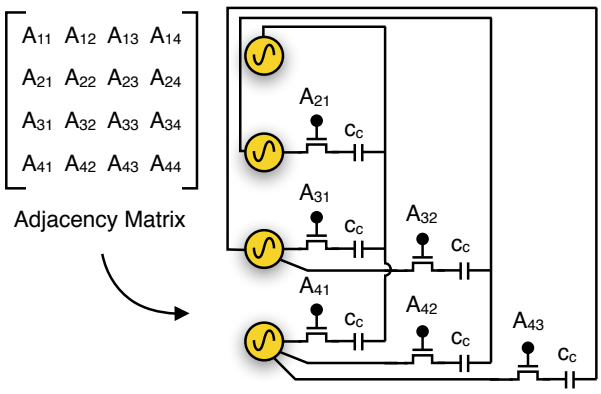

Figure 6.2: A circuit of 4 coupled oscillators with capacitive connections between oscillators controlled using switches corresponding to the adjacency matrix A and coupling capacitance c_c. The subscripts denote the corresponding entries in A. Note that $A_{ij} = A_{ji}$, $A_{ii} = 0$ and $A_{ij} \in \{0,1\}$.

6.2.1 *D-R network coupling*

6.2.1.1 *Modeling*

The mathematical model of the circuit is created as follows. As before, the VO_2 devices switch between a low resistance metallic state with conductance g_{dm} and a high resistance insulating state with conductance g_{di} based on the voltage v_d across their two terminals. On increasing v_d the device switches to a metallic state (insulator-to-metal (IMT) transition) after a threshold v_h, and on decreasing v_d below v_l the device switches back to an insulating state (metal-to-insulator (MIT) transition). Here $v_h > v_l$ and $v_h - v_l$ defines the hysteresis in switching. Consider a supply voltage which is applied across the series combination of such a hysteretic device and a conductance g_s where the subscript s denote a series conductance. Without loss of generality, we assume that at $t = 0$ the device is in high resistance state and the voltage drop across the device $v_d = 0$. The internal capacitance of the device charges up and v_d increases and eventually crosses the threshold v_h. Due to this the device transitions into a metallic state which causes the internal capacitance of the device to discharge and reduces v_d which finally drops below v_l. This causes the device to switch back to the insulating state resulting in oscillations with piecewise linear dynamics.

In case of the coupled oscillator circuit, a loading capacitance c_L of appropriate magnitude is required as shown in figure 6.1a for correct circuit operation.

Recall that the dynamics of a single oscillator (figure 6.1a) can be written as the following piecewise differential equation:

$$cv^{'}(t) = -g(s)\,v(t) + p(s)$$

where c is the lumped capacitance of device along with the loading capacitance and parasitics, $s \in \{0,1\}$ is the state of system - charging (denoted by 1) or discharging (denoted by 0), and $g(s)$ is the net path conductance in state s, with $g(s) = g_s + g_{dm}s$. If the voltage v is normalized to v_{dd} then $p(s) = g_{dm}s$.

The dynamics of the coupled system with n oscillators coupled pairwise to each other using capacitances can be written as:

$$(C_i + C_c + C_l)\,\mathbf{v}'(t) = -G(\mathbf{s})\mathbf{v}(t) + H(\mathbf{s}) \tag{6.1}$$

where $\mathbf{s}$ is the state of the system, $\mathbf{s} = \{s_1, s_2, \cdots, s_n\}$, s_k being the state of k^{th} oscillator and $\mathbf{v}(t)$ is the vector of all the output voltages of oscillators. C_i is the intrinsic internal capacitance matrix and C_l is the loading capacitance matrix. These are diagonal matrices with each element equal to the corresponding capacitance of the oscillator.

$$C_i = \begin{pmatrix} c_{i1} & & 0 \\ & \ddots & \\ 0 & & c_{in} \end{pmatrix}, C_l = \begin{pmatrix} c_{l1} & & 0 \\ & \ddots & \\ 0 & & c_{ln} \end{pmatrix}$$

where c_{ik} is the internal capacitance and c_{lk} is the loading capacitance of k^{th} oscillator.

C_c is the coupling capacitance matrix

$$C_c = \begin{pmatrix} \sum & -c_{c_{12}} & \cdots & -c_{c_{1N}} \\ -c_{c_{21}} & \sum & & -c_{c_{2N}} \\ \vdots & & \ddots & \\ -c_{c_{N1}} & -c_{c_{N2}} & & \sum \end{pmatrix}$$

where $c_{c_{ij}}$ is the coupling capacitances between i^{th} and j^{th} oscillators, and $\sum$ represent the sum of rows (or columns). When all the coupling capacitances are equal to c_c, then C_c is basically the scaled Laplacian matrix L of the graph with $C_c = c_c L = c_c(D-A)$ where D is the diagonal matrix of degrees of vertices and A is the adjacency matrix of the graph. It should be noted that the loading capacitances are chosen such that $diag(C_c + C_l)$ is constant. We envision a system where the oscillators are connected in a graph which is topologically equivalent to the input graph. As such the coupling matrix is programmed by the incidence matrix of the input graph. For each row i in C_c every absent edge ij in the graph adds a loading capacitance of magnitude c_c to the i^{th} node to maintain a constant $diag(C_c + C_l)$. This ensures equal loading effect for all the nodes and symmetric dynamics.

$G(\mathbf{s})$ and $H(\mathbf{s})$ are state dependent matrices

$$G(\mathbf{s}) = \begin{pmatrix} g_1(s_1) & & 0 \\ & \ddots & \\ 0 & & g_N(s_2) \end{pmatrix}, H(\mathbf{s}) = \begin{pmatrix} h_1(s_1) \\ \vdots \\ h_N(s_N) \end{pmatrix}$$

where

$$g_k(s_k) = \begin{cases} g_{dmk} + g_{sk} & s_k = 1, (charging) \\ g_{sk} & s_k = 0, (discharging) \end{cases}$$

and

$$h_k(s_k) = \begin{cases} g_{dmk} & s_k = 1, (charging) \\ 0 & s_k = 0, (discharging) \end{cases}$$

with g_{ik} and g_{sk} being the internal conductance and the series conductance of the k^{th} oscillator respectively.

Thus the dynamics of n coupled oscillators can be written as:

$$\mathbf{v}'(t) = (C_i + C_c + C_l)^{-1} \left[-G(\mathbf{s})\mathbf{v}(t) + H(\mathbf{s})\right]$$

where voltages are normalized to V_{DD}.

Symmetric system with identical oscillators Let us first consider a symmetric system, i.e. all oscillators have equal internal capacitances (c_i), coupling capacitances (c_c), internal metallic conductances (g_{dm}) and series conductances (g_s). In such case, $(C_i + C_c + C_l) = (c_i I + c_c D - c_c A + C_l)$ where A is the adjacency matrix of the graph and D is the diagonal matrix of degrees of vertices. One simple choice of C_l is $C_l = c_c(nI - D)$ which makes

$$\begin{aligned} diag(C_c + C_l) &= diag(c_c D - c_c A + c_c nI - c_c D) \\ &= diag(c_c nI) \\ &= c_c n\, diag(I) \end{aligned}$$

which is constant. Hence the coefficient matrix becomes

$$-G(\mathbf{s})(c_i I - c_c A + c_c nI)^{-1} = G(\mathbf{s})\left(c_c A - (c_i + c_c n)I\right)^{-1}$$

Let us define $B = (c_c A - (c_i + c_c n)I)^{-1}$. Also let $\hat{S}$ be a diagonal matrix where $diag(\hat{S}) = \mathbf{s}$. Then $H(\mathbf{s}) = g_{dm}\mathbf{s}$ and $G(\mathbf{s}) = g_s I + g_{dm}\hat{S}$ where I is the identity matrix. The system of

6.1 can then be written as:

$$\mathbf{v}'(t) = B\left(g_{dm}\hat{S}\mathbf{v} + g_s\left(\mathbf{s}-\mathbf{v}\right)\right) \tag{6.2}$$

The dynamics of a circuit of identical coupled relaxation oscillators can then be described using the following matrix differential equation:

$$\mathbf{v}^{'}(t) = \left(C_i + C_c + C_l\right)^{-1}\left[-G\left(\mathbf{s}\right)\mathbf{v}\left(t\right) + g_{dm}\mathbf{s}\right] \tag{6.3}$$

6.2.1.2 *Phase evolution and dynamics*

We note two important features about the charging transitions: (a) charging processes are very fast compared to the period of oscillations (figure 6.3a), which we also refer to as "charging spikes" and (b) Charging of one oscillator has weak (but finite) effect on the other oscillators. Hence, we study the dynamics of coupled relaxation oscillator system in terms of two distinct interacting systems - the linear dynamics in the discharging state $\mathbf{s} = \mathbf{0}$, and the charging transitions.

As the charging processes are very fast, the relative phases of oscillators are same as the relative times of the charging spikes in the oscillator waveforms. This gives a good way to visualize how the relative phases of oscillators evolve with time. For all oscillators, we first note all the time instants when the charging spikes start. The time differences between consecutive charging spikes should settle to a constant value if the oscillators settle, say Δt_i for the i^{th} oscillator. If all the oscillators synchronize to a common frequency then $\Delta t_i = \Delta t_0$ for all i. Then at any n^{th} charging spike which occur at time instant t_n, we can calculate the relative phase of an oscillator w.r.t. a hypothetical oscillator whose charging spikes occur at regular intervals of Δt_i from the start ($t = 0$) as:

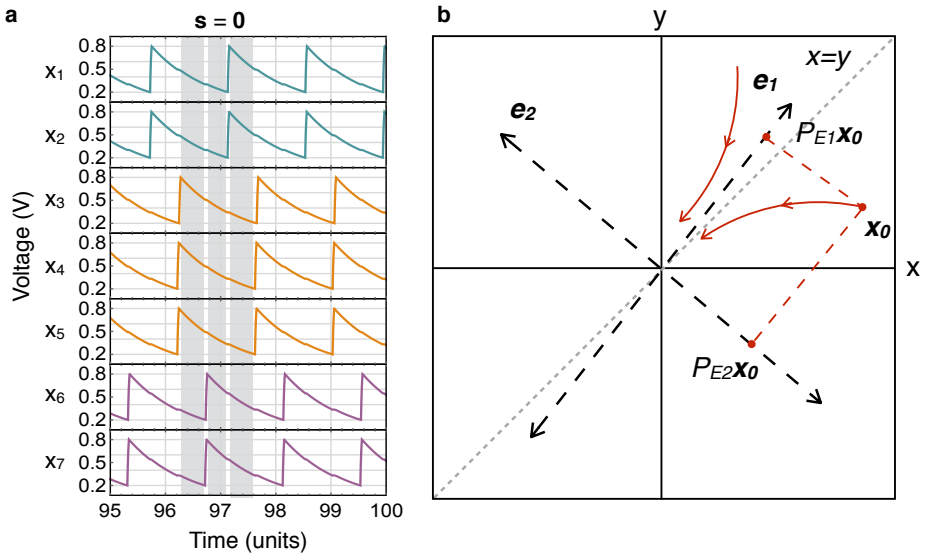

Figure 6.3: (a) Simulation waveforms of a circuit connected in the 3-partite graph shown in Fig. 1a. The gray regions show the time when the system is in state $\mathbf{s} = \mathbf{0}$. (b) Representative figure showing the relation between the asymptotic order of components of the state vector and the eigenspaces in a two-dimensional linear system where the coefficient matrix has negative eigenvalues.

$$\phi(n) = (t_n - n\Delta t_i)\frac{2\pi}{\Delta t_i} \quad (\mod 2\pi)$$

When all Δt_i are equal, i.e. the oscillators synchronize, $\phi(n)$ calculates the relative phases w.r.t. a common Δt_0 for all oscillators. We plot $\phi(n)$ vs n for all oscillators in figure 6.4. What we observe is that the phases $\phi(n)$ converge and cluster together for dense graphs but as the graphs become sparse, which are considered harder, the the phases do not converge. In the intermediate region between dense and very sparse graphs, the phase do converge but they do not cluster together in groups. In these cases our proposed algorithm and reformulation of vertex coloring is particulalry useful because it does not rely on the clustering of phases. Our algorithm does an $O(n^2)$ post-processing on the steady state order of phases and calculates a color assignment which is always correct but can have non-optimal coloring, i.e. the number of colors can be more than the chromatic number.

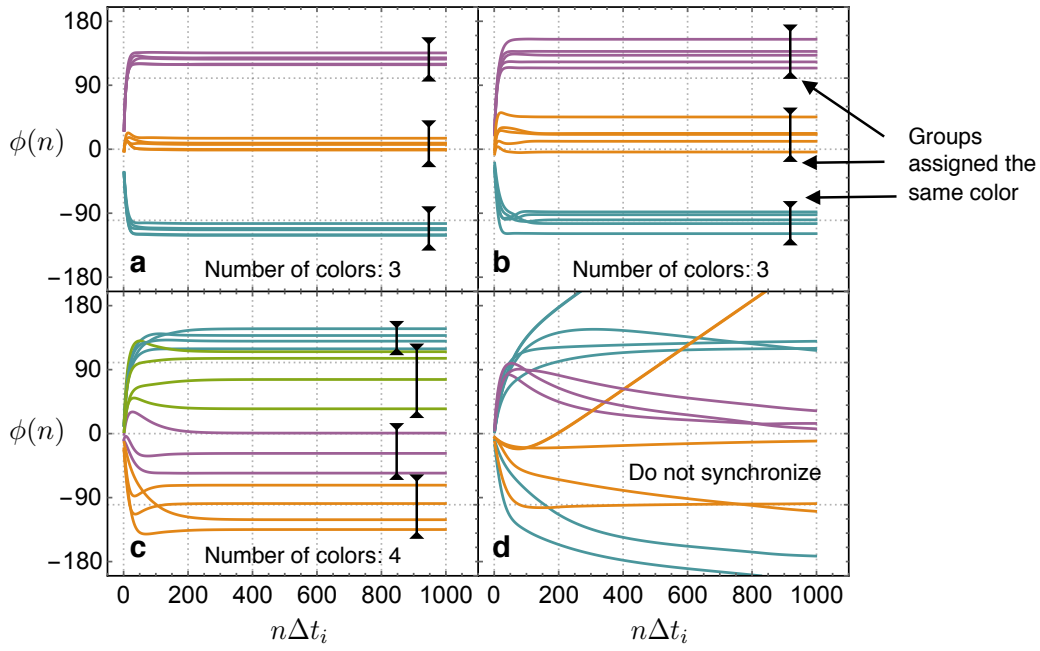

Figure 6.4: The phases $\phi(n)$ plotted against $n\Delta t_i$ for four relaxation oscillator systems for solving 3-colorable graphs with the same color partition $(5,5,5)$ but with different connectivities. Case (a) is the case of a complete 3-partite graph, and graphs become sparser from (a) to (d). The phase clustering degrades as graphs become sparser and for very sparse graphs (d) the oscillators do not synchronize. The number of colors detected using our algorithm is shown with each graph and the nodes which are assigned the same color are indicated.

6.2.1.3 *Dynamics in the discharge state* $\mathbf{s} = \mathbf{0}$

In the state $\mathbf{s} = \mathbf{0}$ where all the oscillators are in the discharging state, the system is an autonomous linear dynamical system

$$\mathbf{v}'(t) = -g_s \left(c_i I + c_c L + C_l\right)^{-1} \mathbf{v}(t)$$

Hence, the time evolution of this dynamical system is governed by the spectral properties of the coefficient matrix. In an identical system, the equation is

$$\begin{aligned} \mathbf{v}'(t) &= g_s \left(c_c A - (c_i + n c_c) I\right)^{-1} \mathbf{v}(t) \\ &= g_s B \mathbf{v}(t) \end{aligned}$$

Let the eigenvectors of B be μ_k.

Proposition 1. *The eigenvectors of the coefficient matrix B of the identical system are the same as those of the adjacency matrix A. The eigenvalues* μ_k *of B are related to the eigenvalues of A as follows:*

$$\mu_k = \frac{1}{c_c \left(\lambda_k - \frac{c_i}{c_c} - n\right)}$$

Moreover, $\mu_k < 0$ *for* $1 \leq k \leq n$.

Proof. For any matrix M with an eigenvalue m, the eigenvectors of $M + \alpha I$ and $\beta \left(M + \alpha I\right)^{-1}$ are same as M for any scalars α and β. This can be seen as follows:

$$\begin{aligned} \left(M + \alpha I\right) x &= Mx + \alpha x \\ &= (m + \alpha) x \end{aligned}$$

And eigenvectors remain unchanged for matrix inverse. Also eigenvalues for $\beta \left(M + \alpha I\right)^{-1}$

will be $\beta/(m+a)$. Substituting appropriate values for α and β gives us the required relation between μ_k and λ_k.

Now, the Perron-Frobenius theory [91]implies that largest eigenvalue of A is less than or equal to the maximum row sum which is less than n, i.e.

$$\lambda_{max} \leq r_{max} < n$$

Hence, $\left(\lambda_k - \frac{c_i}{c_c} - n\right) < 0$ for all k which implies that $\mu_k < 0$ for all k. □

In the linear dynamical system with the state variable $\mathbf{v}(t)$, the order of components of $\mathbf{v}(t)$ also define a permutation at any time instant t. In state $\mathbf{s} = \mathbf{0}$, the linear dynamical system is

$$\mathbf{v}'(t) = B\mathbf{v}(t)$$

where B is real, symmetric and the initial state of the system $\mathbf{v}(0) = \mathbf{v}_0$.

Geometry of permutation regions For any ordering P of components $\mathbf{v}_{i1} > \mathbf{v}_{i2} > \ldots > \mathbf{v}_{in}$, the region that corresponds to this ordering is given by

$$\mathscr{R}_{\mathscr{P}}(P) = \bigcap_{m=i}^{n} \left(\mathbf{v}_{im} > \mathbf{v}_{i(m+1)}\right) \tag{6.4}$$

$\mathscr{R}_{\mathscr{P}}(P)$ is a pair of n-dimensional simplexes with one vertex as the origin and are mirror images of each other about the origin. As such, any line that passes through the origin either passes through both of them, or none.

Asymptotic direction of trajectories In a linear dynamical system, the asymptotic order of components is hence governed by the asympotic direction in which the system state converges to.

Proposition 2. *In the linear dynamical system $\mathbf{v}'(t) = B\mathbf{v}(t)$, where the coefficient matrix B is real, symmetric and full-rank, the system trajectory always converges asymptotically*

to a particular direction. Moreover, if the asymptotic direction is given by $d(\mathbf{v}_0, B)$ where $\mathbf{v}(0) = \mathbf{v}_0$, then $d(\mathbf{v}_0, B)$ lies in the eigenspace of B with the largest eigenvalue (including the sign) almost everywhere, i.e. when the system starts from anywhere except on a set of measure 0.

Proof. Let $\mathbf{v}(t, \mathbf{v}_0)$ be the solution of the dynamical system when the initial starting state $\mathbf{v}(0) = \mathbf{v}_0$. As the fixed point is $\mathbf{0}$, the asymptotic direction $d(\mathbf{v}_0, B)$ to which the system state converges can be written as

$$\begin{aligned} d(\mathbf{v}_0, B) &= \lim_{t \to \infty} \frac{\mathbf{v}(t)}{\|\mathbf{v}(t)\|} \\ &= \lim_{t \to \infty} \frac{e^{Bt}\mathbf{v}_0}{e^{\lambda(\mathbf{v}_0)t}} \end{aligned}$$

where $\lambda(\mathbf{v}_0)$ is the Lypunov exponent of the trajectory starting from $\mathbf{v}_0$. As B is real and symmetric, all its eigenvalues are real and the matrix is diagonalizable. Let $B = Q\Lambda Q^T$, where Λ is the diagonal matrix with of all eigenvalues. Then

$$d(\mathbf{v}_0, B) = Q \left(\lim_{t \to \infty} \frac{e^{\Lambda t}\mathbf{v}_0}{e^{\lambda(\mathbf{v}_0)t}} \right) Q^T \mathbf{v}_0$$

Let $\lambda_1 > \lambda_2 > ... > \lambda_l$ be the l distinct eigenvalues of B, and let E_k, $1 \leq k \leq l$ be the corresponding eigenspaces. Now, $\lambda(\mathbf{v}_0) = \lambda_1$ for $\mathbf{v}_0 \in \bigoplus_{k=1}^{l} E_k \setminus \bigoplus_{k=1}^{l-1} E_k$. This means

$\lambda(\mathbf{v}_0) = \lambda_1$ almost everywhere, i.e. everywhere except on a set of measure 0. Hence

$$\begin{aligned} d(\mathbf{v}_0, B) &= Q \begin{pmatrix} 1 & 0 & 0 & \cdots & 0 \\ 0 & 1 & 0 & & \\ 0 & 0 & \ddots & & \\ \vdots & & & 0 & \\ 0 & & & & \ddots \end{pmatrix} Q^T \mathbf{v}_0 \\ &= \left(q_{1a} q_{1a}^T + q_{1b} q_{1b}^T + \ldots\right) \mathbf{v}_0 \\ &= P_{E_1} \mathbf{v}_0 \end{aligned}$$

Here, the diagonal elements of the middle matrix are ones only for the rows corresponding to the eigenvector λ_1, and $q_{1a}, q_{1b}, \ldots$ are orthogonal vectors that span E_1. Hence $d(\mathbf{v}_0, B) \in E_1$ almost everywhere. In case the largest eigenvalue λ_1 of B has multiplicity 1, $d(\mathbf{v}_0, B)$ is simply q_1 a.e. □

Asymptotic order of components The asymptotic order of components of $\mathbf{v}(t)$ is determined by the permutation region in which $d(\mathbf{v}_0, B)$ lie. Let $T(\mathbf{v})$ denote the order of components of vector $\mathbf{v}$, then $T(d(\mathbf{v}_0, B)) = T(P_{E_1} \mathbf{v}_0)$ is the asymptotic order of components of $\mathbf{v}(t)$. The asymptotic order becomes a little more complex when $d(\mathbf{v}_0, B)$ lies at the boundary of two or more permutation regions, i.e. some of the components of $d(\mathbf{v}_0, B)$ are equal. In such cases, $T(d(\mathbf{v}_0, B))$ is only a partial order as determined by $d(\mathbf{v}_0, B)$. $T(d(\mathbf{v}_0, B))$ can be extended to a total order by the asymptotic direction of the system in the remaining space $E_2 \oplus E_3 \oplus \ldots \oplus E_l$. Let us denote this by $d(\mathbf{v}_0 \backslash E_1)$. Also, let P_{E_1} be the projection matrix on E_1, then

$$d(\mathbf{v}_0, B \backslash E_1) = \lim_{t \to \infty} \frac{(I - P_{E_1}) \mathbf{v}(t)}{\| (I - P_{E_1}) \mathbf{v}(t) \|}$$

Now, $d(\mathbf{v}_0, B \backslash E_1) \perp d(\mathbf{v}_0, B)$. When $d(\mathbf{v}_0, B)$ is at the boundary of some permutation

regions, the disambiguation among these regions, i.e. ordering among the components which are equal, is done by $d(\mathbf{v}_0, B\backslash E_1)$ as it is perpendicular to $d(\mathbf{v}_0, B)$. Hence, the asymptotic order is determined by both $d(\mathbf{v}_0, B)$ and $d(\mathbf{v}_0, B\backslash E_1)$. If $d(\mathbf{v}_0, B\backslash E_1)$ lie at the boundary of some other permutation regions, then the argument can be extended in a similar way and the asymptotic order of components is determined by $d(\mathbf{v}_0, B)$, $d(\mathbf{v}_0, B\backslash E_1)$ and $d(\mathbf{v}_0, B\backslash E_1 \oplus E_2)$ together, and so on.

The extension of the partial order $T(d(\mathbf{v}_0, B))$ using $T(d(\mathbf{v}_0, B\backslash E_1))$ is similar to the ordinal sum $T(d(\mathbf{v}_0, B)) \oplus T(d(\mathbf{v}_0, B\backslash E_1))$ but a preferential one, i.e. the orders determined by $T(d(\mathbf{v}_0, B))$ are preferred over those determined in $T(d(\mathbf{v}_0, B\backslash E_1))$. Let us denote this operation by the binary operator $\oplus'$ which acts on an ordered pair of two partial orders and gives another partial or total order.

The range of $(I - P_{E_1})$ is $E_2 \oplus E_3 \oplus ... \oplus E_l$. The dynamics that govern the time evolution of $(I - P_{E_1})x(t)$ in the space $E_2 \oplus E_3 \oplus ... \oplus E_l$ is simply determined by the eigenvectors and eigenvalues corresponding to $E_2, E_3, ..., E_l$. Hence from 2, $d(\mathbf{v}_0, B\backslash E_1) \in E_2$. Specifically,

$$d(\mathbf{v}_0, B\backslash E_1) = \left(q_{2a}q_{2a}^T + q_{2b}q_{2b}^T + ...\right)\mathbf{v}_0$$

where $q_{2a}, q_{2b}, ...$ are the eigenvectors corresponding to λ_2. Extending the argument, we have $d(\mathbf{v}_0\backslash E_1 \oplus E_2) \in E_3$ and so on. Hence, we have the following:

Proposition 3. *The asymptotic order of components of* $\mathbf{v}(t)$ *in the linear dynamical system* $\mathbf{v}'(t) = B\mathbf{v}(t)$*, where the coefficient matrix B is real, symmetric and full-rank, is determined by* $T(d(\mathbf{v}_0, B))$*. In case* $d(\mathbf{v}_0, B)$ *lies on the boundary of some permutation regions then* $T(d(\mathbf{v}_0, B))$ *is a partial order which can be extended to a total order as* $T(d(\mathbf{v}_0, B)) \oplus' T(d(\mathbf{v}_0, B\backslash E_1))$*. And in case* $d(\mathbf{v}_0, B\backslash E_1)$ *lies at some boundary then the asymptotic order*

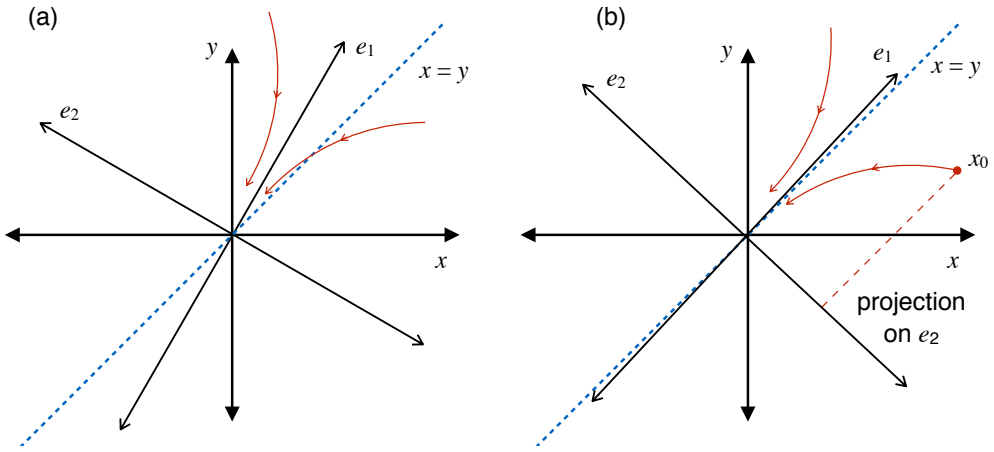

Figure 6.5: Representation of flows in a two dimensional linear dynamical system where both eigenvalues are negative and $|\lambda_2| > |\lambda_1|$. (a) The system trajectory approaches the direction of e_1 with time and hence the order of components, i.e. the order of x and y coordinates is determined by e_1. (b) When e_1 lies close to the $x = y$ line, the order depends on which side x_0 lies w.r.t. e_1 which is given by the projection of $\mathbf{v}_0$ on e_2.

is determined as $T(d(\mathbf{v}_0, B)) \oplus' T(d(\mathbf{v}_0, B \backslash E_1)) \oplus' T(d(\mathbf{v}_0, B \backslash E_1 \oplus E_2))$ *. Moreover,*

$$\begin{aligned} d(\mathbf{v}_0, B) &= \left(q_{1a} q_{1a}^T + q_{1b} q_{1b}^T + \ldots\right) \mathbf{v}_0 = P_{E_1} \mathbf{v}_0 \in E_1 \\ d(\mathbf{v}_0, B \backslash E_1) &= \left(q_{2a} q_{2a}^T + q_{2b} q_{2b}^T + \ldots\right) \mathbf{v}_0 = P_{E_2} \mathbf{v}_0 \in E_2 \\ d(\mathbf{v}_0, B \backslash E_1 \oplus E_2) &= \left(q_{3a} q_{3a}^T + q_{3b} q_{3b}^T + \ldots\right) \mathbf{v}_0 = P_{E_3} \mathbf{v}_0 \in E_3 \end{aligned}$$

and so on. Hence, the asymptotic order of components is determined as

$$Q_0(\mathbf{v}_0) = T(P_{E_1} \mathbf{v}_0) \oplus' T(P_{E_2} \mathbf{v}_0) \oplus' T(P_{E_3} \mathbf{v}_0) \ldots$$

6.2.1.4 *Dynamics in the charging states* $\mathbf{s}\neq\mathbf{0}$

When $\mathbf{s} \neq \mathbf{0}$ the system is a linear dynamical system, but the fixed point is not 0. The identical system in a charging state s can be described as

$$\begin{aligned} \mathbf{v}'(t) &= B\left[G(\mathbf{s})\mathbf{v}(t) - H(\mathbf{s})\right] \\ &= BG(\mathbf{s})\left(\mathbf{v}(t) - G(\mathbf{s})^{-1}H(\mathbf{s})\right) \end{aligned}$$

The fixed point of the system in a state s is

$$G(\mathbf{s})^{-1}H(\mathbf{s}) = \frac{g_i}{g_s + g_i}\mathbf{s}$$

and the coefficient matrix for the linear flow is

$$\left(c_c A - (c_i + c_c n)I\right)^{-1} G(\mathbf{s}) = BG(\mathbf{s})$$

where $B = \left(c_c A - (c_i + c_c n)I\right)^{-1}$ as in the previous section about discharging state. When $g \gg g_s$, i.e. the chargings are much faster than the dischargings, the fixed points of the system are close to s which are the corners of the unit cube in n dimensions. Following the arguments as in section 6.2.1.3, even in this case the system trajectory will converge to an asymptotic direction. The asymptotic ordering of components would depend on first the fixed point, and in case the fixed point has equal components then it would also depend on the asymptotic direction of trajectory. This is explained as:

Proposition 4. *In the linear dynamical system of the charging states* $\mathbf{v}'(t) = BG(\mathbf{s})\left(\mathbf{v}(t) - \mathbf{p}\right)$, *where* $\mathbf{p} = \frac{g}{g_s+g}\mathbf{s}$ *is the fixed point and the coefficient matrix B is real, symmetric and full-rank, the asymptotic permutation of the components will be same as the permutation of components of the fixed points, i.e.* $T(\mathbf{p})$. *In case the fixed point* $\mathbf{p}$ *lies at (or close) to the boundary of some permutation regions, i.e. some components of* $\mathbf{p}$ *are equal, the disam-*

biguation of ordering among these components can be done considering the linear dynamics of $\mathbf{v}'(t) = B\mathbf{v}(t)$ *with fixed point shifted to* $\mathbf{0}$*, and following Propositions 3. Hence, the asymptotic order of components is given by*

$$\begin{aligned} Q_s(\mathbf{v}_0) &= T(\mathbf{p}) \oplus' T(P_{sE_1}\mathbf{v}_0) \oplus' T(P_{sE_2}\mathbf{v}_0) \oplus' \dots \\ &= T(\mathbf{s}) \oplus' T(P_{sE_1}\mathbf{v}_0) \oplus' T(P_{sE_2}\mathbf{v}_0) \oplus' \dots \end{aligned}$$

where $P_{sE_1}, P_{sE_2}, \dots$ *are the projections on the eigenspaces of* $BG(\mathbf{s})$*.*

In case the matrix B in the equation $\mathbf{v}'(t) = BG(\mathbf{s})(\mathbf{v}(t) - \mathbf{p})$ is not full rank, the system trajectory does not converge to the point $\mathbf{p}$. If N is the null space of the matrix B and P_N is the projection on the null space N, then the convergence limit point for the trajectory starting from $\mathbf{v}_0$ is $\mathbf{p} + P_N\mathbf{v}_0$. Also, N is also the null space for $BG(\mathbf{s})$ for all $\mathbf{s}$. Hence, Proposition 4 can be modified for matrices B which are not full-rank as follows

Proposition 5. *In the linear dynamical system as described in Proposition 4, but where B is not full rank, the asymptotic order of components is given by*

$$Q_s(\mathbf{v}_0) = T\left(\frac{g_i}{g_i + g_s}\mathbf{s} + P_{sN}\mathbf{v}_0\right) \oplus' T(P_{sE_1}\mathbf{v}_0) \oplus' T(P_{sE_2}\mathbf{v}_0) \oplus' \dots$$

where P_{sN} *is the projection matrix on the null space of* $BG(\mathbf{s})$*.*

When $\mathbf{v}_0$ is close to the eigenspaces, i.e. magnitude of $P_{sN}\mathbf{v}_0$ is very small, the additive term of $P_N\mathbf{v}_0$ in the first term does not change the order determined by $\mathbf{s}$. Formally, when $\max\{(P_N\mathbf{v}_0)_i\} < \frac{g_s}{g_i+g_s}$

$$T\left(\frac{g_i}{g_i + g_s}\mathbf{s} + P_N\mathbf{v}_0\right) = T(\mathbf{s}) \oplus' T(P_N\mathbf{v}_0)$$

and hence,

$$Q_s(\mathbf{v}_0) = T(\mathbf{s}) \oplus' T(P_{sN}\mathbf{v}_0) \oplus' T(P_{sE_1}\mathbf{v}_0) \oplus' T(P_{sE_2}\mathbf{v}_0) \oplus' \dots \tag{6.5}$$

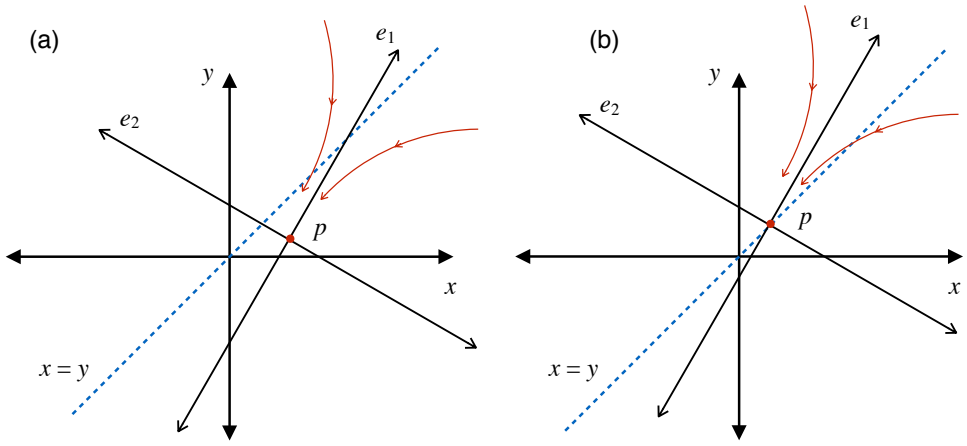

Figure 6.6: (a) When the fixed point in a two dimensional linear dynamical system is not **0** then the asymptotic order of the components is determined by the fixed point **p**. (b) If the fixed point lies on the $x = y$ line, which is a boundary of permutations regions, then the disambiguation is done using the eigenvectors.

APPROXIMATION BY INSTANTANEOUS CHARGING If the chargings are very fast, i.e. $\frac{g_s}{g_i} \to 0$, we can approximate the chargings by an instantaneous change in the state from $\mathbf{v}$ to $\mathbf{v} + \Delta\mathbf{v}$ by linearizing the system at the time instant when the state changes from $\mathbf{s} = \mathbf{0}$ to the charging state. Let $\hat{S}$ denote a diagonal matrix such that $diag(\hat{S}) = \mathbf{s}$ where $\mathbf{s}$ is the state vector. When $\mathbf{s} \neq \mathbf{0}$ we have from (6.2)

$$\begin{aligned} \mathbf{v}'(t) &= B\left(g_i \hat{S}\mathbf{v} + g_s(\mathbf{s} - \mathbf{v})\right) \\ &= Bg_i\left(\hat{S}\mathbf{v} + \frac{g_s}{g_i}(\mathbf{s} - \mathbf{v})\right) \\ &\simeq g_i B\hat{S}\mathbf{v} \end{aligned}$$

If the k^{th} node charges then $\hat{S}\mathbf{v} = v_l\mathbf{e_k}$ where $\mathbf{e_k}$ is the $k - axis$ vector whose all components are **0** expect the k^{th} which is **1**. If the k^{th} node charges completely from v_l to v_h

without any state transition in between, we have

$$\begin{aligned} (\Delta \mathbf{v})_k &= dv \\ \implies (\mathbf{v}')_k \Delta t &= dv \\ \implies \Delta t &= \frac{dv}{(g_i B \hat{S} \mathbf{v})_k} \\ &= \frac{dv}{g_i v_l \mathbf{e_k}^T B \mathbf{e_k}} \\ &= \frac{dv}{g_i v_l B_{kk}} \end{aligned}$$

Therefore,

$$\begin{aligned} \Delta \mathbf{v} &= \mathbf{v}' \Delta t \\ &= dv \frac{v_l g_i B \mathbf{e_k}}{v_l g_i B_{kk}} \\ &= \frac{dv}{B_{kk}} B \mathbf{e_k} \end{aligned}$$

which is just a scaled column vector of B. We have the following:

Proposition 6. *In the dynamical system of (6.2), when* $\mathbf{s} \neq \mathbf{0}$ *and only a single node charges, the chargings can be approximated by linearizing the system. If the transition occurs from* $\mathbf{v}$ *to* $\mathbf{v} + \Delta \mathbf{v}$ *then* $\Delta \mathbf{v}$ *is given by:*

$$\Delta \mathbf{v} = \frac{dv}{B_{kk}} B \mathbf{e_k}$$

Remark 1. An important point to note here is that this change is independent of $\mathbf{v}$.

6.2.1.5 *Minimum Graph Coloring Problem and its reformulation*

The main point of studying these oscillators is to use them for some computing problem, specifically *graph coloring*. To understand the connection between the dynamics of coupled oscillators and an algorithm of graph coloring, viz. spectral algorithm, let's first describe the problem of graph coloring. The objective of *graph coloring* or *vertex coloring* is

to assign one color (out of total k colors) to each vertex of an undirected graph such that no two adjacent vertices receive the same color. A graph coloring that minimizes the number of colors k is called *minimum graph coloring*. The minimum k for which a correct coloring is possible is called the *chromatic number* of the graph. A graph which can be colored using at most k colors is called a *k-partite graph*. A k-partition of a set, like the set of nodes, is a grouping of the elements of the set into k groups. Hence, a vertex coloring with k colors is a k-partition. We reformulate the objective of finding a color assignment to finding a circular permutation of nodes such that the same colored nodes appear together. We refer to this reformulation as *vertex color-sorting* and the corresponding optimal version as *minimum vertex color-sorting*.

Definition 1. (k-Color-Sorting) An ordering $u = \{u_i\}$, $i \in [1,n]$ of the n nodes of a graph is a proper k-Color-Sorting if there exists a proper k-Coloring $\{c_i\}$, $i \in [1,n]$, where c_i is the color assigned to the i^{th} node such that all nodes with the same color appear together in u, i.e. for any nodes i, j, k with $u_i < u_k < u_j$, $c_i = c_j \implies c_i = c_k = c_j$. This can be extended to a cyclic ordering where the nodes with the same color appear together.

The following results are helpful in understanding coloring in terms of sorting.

Lemma 1. *For a graph with n nodes, adjacency matrix A and chromatic number χ_A:*

1. Any ordering of nodes S is a proper k-Color-Sorting for some k such that $\chi_A \leq k \leq n$.

2. Let $B(M)$ be the minimum number of diagonal blocks which are identically $'0'$ and which cover the complete diagonal of the matrix M. The minimum k for which S is a proper k-Color-Sorting is $B(PAP^T)$. If S is a proper k-Color-Sorting and P its permutation matrix, then

$$\chi_A \leq B(PAP^T) \leq k$$

Proof. Any ordering S is a proper n-Color-Sorting, and if S is a proper k color sorting then minimum number of colors can be χ_A.

If P is the permutation matrix of an ordering u, then PAP^T is the adjacency matrix of a graph with the ordering of nodes changed to u. If u is a proper k-Color-Sorting then, PAP^T will have at least k number of $'0'$ diagonal blocks, one corresponding to each color group, hence, $B(PAP^T) \leq k$. Also, the diagonal blocks which are $'0'$ also determine a valid coloring of the graph and hence $B(PAP^T) \geq \chi_A$. □

Proposition 7. *For a k-chromatic graph, k-Color-Sorting is NP hard. Moreover, finding the chromatic number χ_A of a graph with adjacency matrix A and the proper χ_A-Coloring is equivalent to the following optimization problem:*

$$min B(PAP^T), \quad P \in all\ permutations\ of\ nodes$$

where the solution P is a proper χ_A-Color-Sorting, $\chi_A = min\{B(PAP^T)\}$.

Proof. Computing $B(PAP^T)$ is a $O(n^2)$ problem, n being the number of nodes because there are n^2 elements in PAP^T. And for a k-chromatic graph, $\chi_A = B(PAP^T) = k$ where P is a proper k-Color-Sorting. Hence, χ_A can be computed in $O(n^2)$ if a proper k-Color-Sorting P can be found.

Also, for any permutation P, $B(PAP^T) \geq \chi_A$ as stated above, where equality holds only when P is a proper χ_A-Color-Sorting. Hence, finding chromatic number is equivalent to the stated optimization problem. Also, once a proper χ_A-Color-Sorting is known, the $'0'$ diagonal blocks also determine the proper χ_A-Coloring. □

Using this method, any permutation P gives a correct color assignment but a *better* permutation gives lesser number of colors, and an optimal color-sorting permutation gives the minimum number of colors. In the proposed coupled oscillator system, each oscillator represents a vertex (or node) of the graph. Any two nodes connected in the original graph by an edge (as indicated by a '1' in A), are capacitively coupled in the hardware implementation. As the coupled system evolves, the relative phases of the oscillators are ordered, and we

observe that the relative ordering of the phases approximates *minimum vertex-color-sorting* of the original graph.

6.2.1.6 *Connection to Vertex Coloring*

The eigenvectors with least negative eigenvalues determine not just the asymptotic order in state $\mathbf{s} = \mathbf{0}$ but also the limit cycle. To obtain an intuitive understanding of how the system settles to a limit cycle with the correct color-sorting, i.e. steady state oscillations where order of charging spikes become constant and equal to a correct color-sorting, we consider the following proposition.

Proposition 8. *The following three conditions when satisfied result in the existence of a cycle and helps us understand why the possibility of it reduces as graphs become sparser, and hence harder.*

1. ***Attractor:*** *The system in state* $\mathbf{s} = 0$ *tries to order the components of the state vector in the correct vertex color-sorting. Hence, if the system starts from a state* x_0 *whose order of components is same as the final asymptotic order, i.e.* $T(x_0) = Q_0(x_0)$*, then with time* $T(x(t))$ *remains constant.*

2. ***Ordering:*** *The charging spikes just change the order of components of x by a circular permutation. If the* k^{th} *oscillator charges from* v_l *to* v_h *then the order of all other components remains same.*

3. ***Sustaining the cycle:*** *If condition 2 is true then the charging transitions cycle the order of* x_0 *to all the circular permutations. For a cycle to exist, the state* $s = 0$ *should not only preserve the order of* x_0 *when* $T(x_0) = Q_0(x_0)$ *but it should also have lower tendency to change the order when* $T(x_0)$ *is any circular permutation of* $Q_0(x_0)$*.*

Why these conditions hold in the prototypical case of complete graph with equal number of nodes in each color class can be seen as follows.

Explanation for condition 1: The adjacency matrix A in the prototypical case is a low rank matrix with the rank equal to the number of colors, i.e. if it is a k-partite graph then rank is n. The adjacency matrix is a block matrix with equal sized k^2 blocks and the diagonal blocks are 0 and the non-diagonal blocks are 1. One eigenvector of the matrix A is the constant vector $[1,1,1,...]$ which is the diagonal of the n-dimensional cube $[v_l, v_h]^n$ and also lies at the intersection of all the simplexes of the permutation regions (equation 6.4) and does not affect the asymptotic order of components of x. Hence all the other eigenvectors decide the asymptotic order and lie in the non-positive quadrants. The eigenvectors of B with least negative eigenvalues (which are the eigenvectors of A with most negative eigenvalues) have components which are equal on each color class (Appendix A.1.1) and hence should direct the system towards a correct vertex color-sorting in state $s = 0$. We also know that all the eigenvalues of the coefficient matrix in the state $s = 0$ are negative, and hence, if the system starts with the correct order of components, i.e. $T(x_0) = Q_0(x_0)$ then the system state x will continue to lie in the same permutation region with time.

Explanation for condition 2: Assuming very fast charging and using the instantaneous charging approximation, we see from Proposition 6 that the state transition Δx is in the direction of the k^{th} column vector of B when the k^{th} node charges. As shown in appendices A.1.2 and A.1.3, in case of weak coupling, i.e. $c_i \gg c_c$ the k^{th} column vector is constant for all non-charging components and hence Δx does not change the order of the non-charging components. The variation in the non-charging components of Δx is inversely propotional to $n+m$ and hence with larger n and m the charging transition $x \to x + \Delta x$ tries to preserve the order of non-charging components more (Appendix A.1.3). As shown in figure 6.7 the effect of charging transitions can be seen as small kinks in the waveforms of non-charging components. The magnitude of these kinks is negligible for weak coupling (a), and is clearly visible for stronger coupling (c). Even though the charging transitions affect the non-charging components in the case of a stronger coupling, the order of non-charging components is not disturbed, i.e. the change in all the non-charging components is almost

the same (Appendix A.1.3).

Explanation for condition 3: If the system state x is close to the eigenspace of B with least negative eigenvalue, say E_1, then x has components which are close for the same color class (Appendix A.1.1) and components of different color classes will have more separation between them by comparison. If the components of x are ordered in increasing order then it will have a pattern $\{x_{a_1}, x_{a_2}, ..., x_{b_1}, x_{b_2}, ..., x_{c_1}, x_{c_2}, ...\}$, where a_i are the indices for one color class, b_i for another etc. If the order among the color classes is changed, say $\{x_{b_1}, x_{b_2}, ..., x_{a_1}, x_{a_2}, ..., x_{c_1}, x_{c_2}, ...\}$ even then x will be close to the eigenspace E_1 because of the multiplicity of the least negative eigenvalue (Appendix A.1.1). The charging transitions of nodes of the same color class will occur consecutively with little time durations between them. This little time does not allow the system state $s = 0$ which occurs between these transitions to change the order. When all nodes of one particular class have undergone charging processes, the system state x again comes close to the eigenspace E_1 because the components of x belonging to the same color class are again close to each other. Hence, the state $s = 0$ does not disurb this order as well. The cycle repeats with very fast consecutive charging processes of the next color class. This also gives rise to clustering of the phases of nodes w.r.t. their color classes.

Adjacency matrices of non-simple graphs can be considered as perturbations to the prototypical cases of complete graphs, and using perturbation theory of matrices we can say that the eigenvectors of perturbed matrices are rotations of the original eigenvectors [92], where the extent of rotation depend on the amount of perturbation. Hence, even in non-simple cases, the eigenvectors with most negative eigenvalues of the adjacency matrix will tend to have components which are close to each other within the same color class and away from those of different color classes. This property has been explored with mathematical detail in works related to spectral algorithms for graph coloring [**Alon:aa**, **Aspvall:aa**, **McSherry:aa**]. When viewed from the perspective of a coupled relaxation

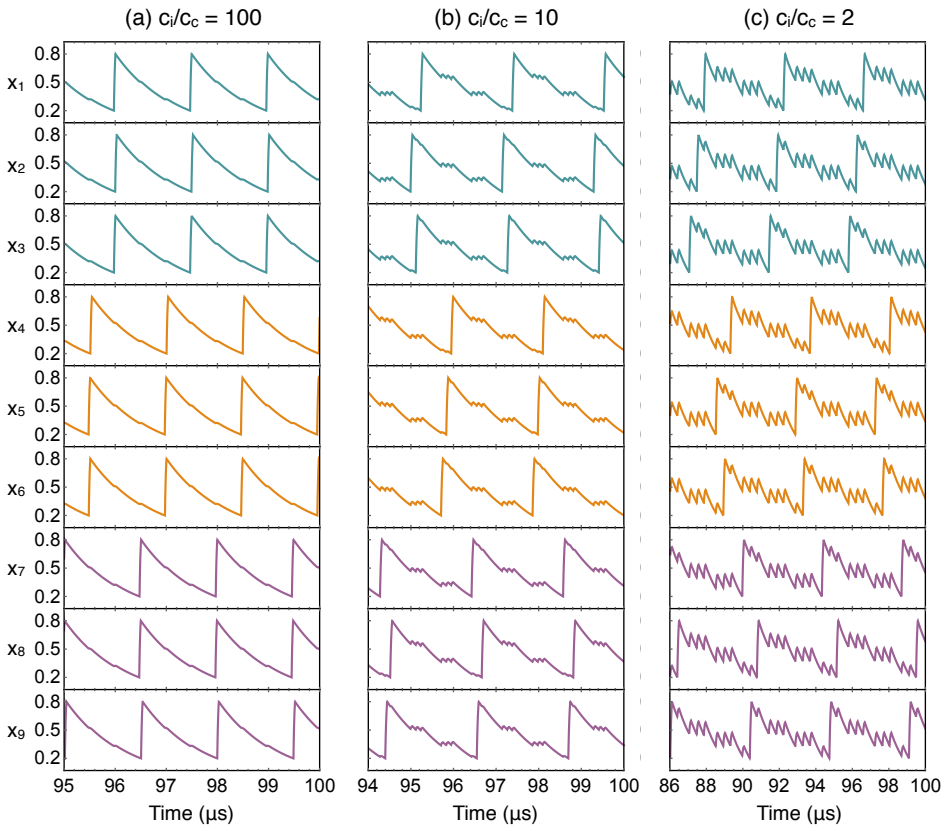

Figure 6.7: Simulation waveforms of a coupled relaxation oscillator circuit connected in a complete 3-partite graph with 3 nodes in each color class for different c_i/c_c values (a) 100, (b) 10, and (c) 2. As can be seen, the charging transitions do not affect the non-charging components of the state vector $x$in case of weak coupling (a). In case of stronger coupling (c), even though the charging transitions affect the non-charging components (seen as small kinks in the waveforms), the order of non-charging components is undisturbed.

oscillator system of (6.2), the above mentioned property of eigenvectors of the adjacency matrix A with most negative eigenvalues will be shared by the eigenvectors of B with the least negative eigenvalues because of Proposition 1. As shown above, the asymptotic order of components of the system state in the discharge phase $s = 0$ of coupled relaxation oscillator systems depend on the least negative eigenvalues of B. Hence, the relaxation oscillator systems in state $s = 0$ is expected to direct the system towards correct vertex color sorting, which satisfies condition 1 of Proposition 8. Conditions 2 and 3 also depend on eigenvectors and hence similar arguments of matrix perturbation can be applied. This also explains why vertex color-sorting using the coupled relaxation oscillator circuit becomes less optimal as graphs become sparse. This is known to be true for spectral algorithms as well as heuristics that dense graphs are easier to color than sparser ones.

6.2.1.7 *Simulation Results and Performance Assessment*

We simulate the dynamical system as described by (6.3) for random graph instances of 3-colorable graphs. The initial conditions are chosen at random $\mathbf{x_0} \in [0.35, 0.65]^n$ and $\mathbf{s} = \mathbf{1}$ at $t = 0$ because all oscillators are in charging state when the power is switched on. Without loss of generality, v_l and v_h are chosen as 0.2 and 0.8. To assess the performance of such circuit on random graphs, we use a random graph generation model $G(n,k,i)$ to generate instances of colorable k-partite graphs with total n nodes. The graphs are generated by first choosing a random k-partition of n nodes, then creating a complete k-partite graph with this k-partition and finally removing random i number of edges from this complete graph. *Average connectivity* is defined as the ratio of total number of edges in the generated graph $G(n,k,i)$ to the total number of edges in the complete k-partite graph with the same partition.

As is true with hard problems, even in graph coloring problems no heuristic algorithm works best for all graph instances [93]. Also different heuristics work better for different instances, and hence no single *order parameter* can account for the hardness of an instance

of a graph coloring problem [94–96]. The most commonly used order parameter is average connectivity [97]. We use this parameter to account for the hardness of the problems being solved and observe how a coupled relaxation oscillator network behaves for problems with varying levels of average connectivity. Observations are made particularly about the *cluster diameter*, the *number of colors detected* and the *settling time,* which are defined as follows.

When the coupled oscillator circuit settles to a correct color-sorting, the phases of oscillators or nodes with the same color form a cluster for many graphs, esp. the dense graphs. The maximum phase difference of two oscillators in the same cluster, i.e. with the same color, is called the *cluster diameter*. The *number of colors detected* is calculated using the order of charging spikes at the end of the finite time period for which the circuit is simulated. *Settling time* is the defined as the time after which the number of colors detected does not change till the end of the simulation time.

Figure 6.8 gives a visualization to how the order of charging spikes evolves with time for 3 different graphs of 20 nodes with decreasing average connectivity. All three graphs are 3-partite with partition $(8, 2, 10)$. For a single simulation instance, we note the order of charging spikes at various time instances and associate a unique number (within a simulation instance) to each permutation. A plot of this permutation number with time shows how the order, or permutation, of the charging spikes evolve with time. Figure 6.8 shows this plot along with plot of the number of colors detected using the order of charging spikes at various times. Figure 6.8a shows the typical case of a complete partite graph where the order of charging spikes settles quickly to a correct color-sorting, and the number of colors detected falls quickly to the minimum number of colors (3 in this case). Figures 6.8b and 6.8c show graphs with lower connectivity but the same partition structure. We make two observations. Firstly, even after the number of colors detected settles down, the permutation or order of charging spikes can evolve. Secondly, figure 6.8c shows lower number of colors detected than figure 6.8b but the settling time is higher for figure 6.8c.

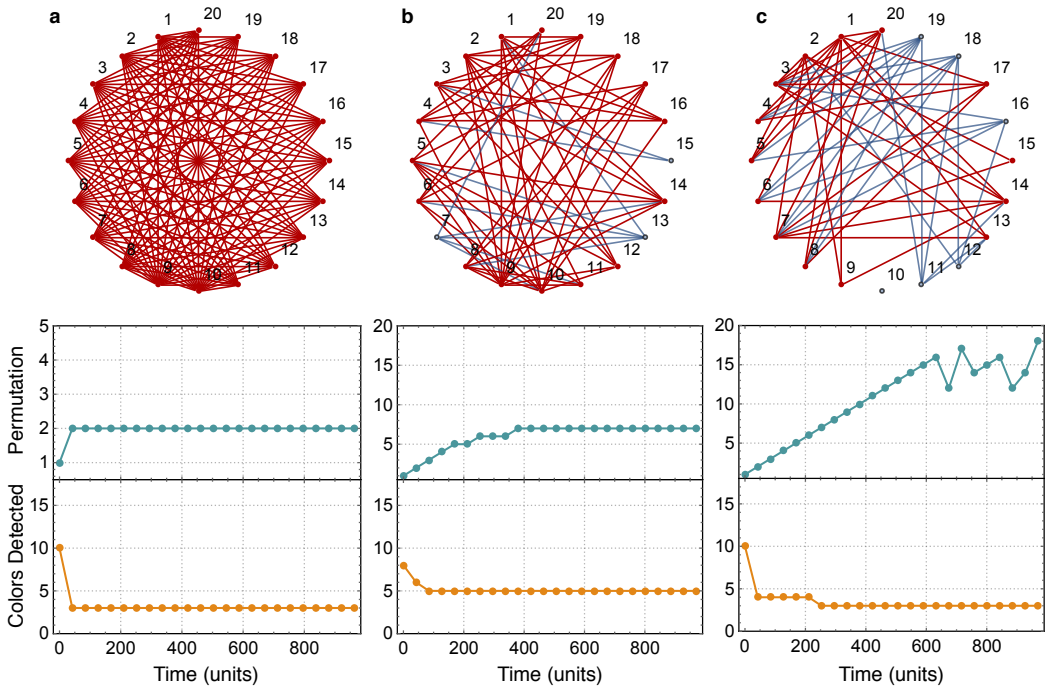

Figure 6.8: (Above) Graph diagram and (below) waveforms of permutation number (a unique number corresponding to each permutation) of charging spikes and number of colors detected with time. All graphs are 3-partite with partition $(8, 2, 10)$ with varying levels of average connectivity: (a) 1.0, (b) 0.57 and (c) 0.48. All triangles in the graph are shown with red edges and the rest edges are shown in blue.

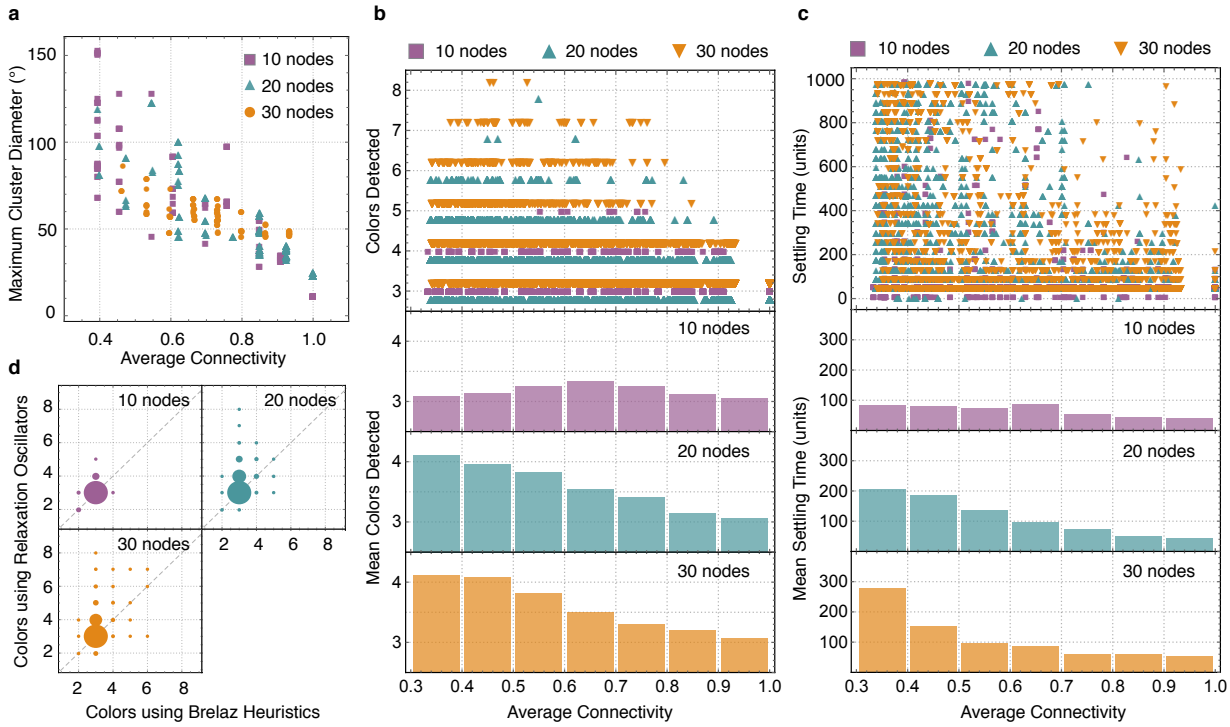

Figure 6.9: (a) Maximum cluster diameter for those graphs for which 3 colors were detected. (b) (Top) Number of colors detected plotted against the average connectivity. (Below) Mean colors detected in connectivity intervals. (c) (Top) Settling time plotted against the average connectivity. (Below) Mean settling time in connectivity intervals. (d) Number of colors detected using the relaxation oscillator circuit plotted against number of colors detected using Brelaz heuristics for the random graph instances used in b and c. Each graph instance represents a point whose coordinates are denoted by the pair of colors detected using the two methods. The size of dots represents the percentage of instances which lie at the center of corresponding dot.

As such, both settling time and number of colors detected can be considered as *imperfect* order parameters for hardness of graph coloring just like average connectivity.

Figure 6.9 shows the performance of such network on random graph instances. We generate 3-partite graphs using $G(10,3,i)$, $G(20,3,i)$ and $G(30,3,i)$ with increasing values of i. The graphs which become bipartite after removing i edges are discarded. Various metrics to evaluate the circuit output are plotted against average connectivity. We see that as graphs become sparse with decreasing average connectivity, the cluster diameter increases (figure 6.9a). This comparison is made only among those graphs where the final phases are

clustered correctly into 3 clusters, i.e. the number of colors detected is 3. When graphs are dense and closer to being complete partite, the possibility of them being optimally colored with 3 colors is high, and the settling time on average is less (figure 6.9b,c). As graphs become sparser, the number of colors detected (figure 6.9b) as well as settling time (figure 6.9c) increase statistically on average. It also follows our intuitive understanding that hard computational problems remain hard even under domain transformation, albeit with potential practical implications such as increased energy-efficiency and performance benefits of continuous time systems over their digital counterparts. A comparison of colors detected from simulating the coupled oscillator network with that using Brelaz Heuristics [98] (figure 6.9d) shows the effectiveness of the circuit as a tool to approximate the *minimum graph coloring problem*. Number of colors detected by simulating sample graphs from the second DIMACS implementation challenge [99] are shown in Table 6.1, where for certain instances we note that the dynamical system outperforms heuristic algorithms.

As such, it is established that a system of capacitively coupled relaxation oscillators can perform graph coloring, which is a commonly studied and practically useful combinatorial optimization problem. Further, the connection between system dynamics and the order of steady state phases of oscillators with spectral techniques for graph coloring has been discussed and it shows an innate, yet, hitherto unexplored, connection between the time evolution of dynamical systems and computationally hard problems that have solutions or approximations in the spectral domains.

6.2.1.8 *Experimental Demonstrations*

As was done in previous experiments, a relaxation oscillator is constructed by exploiting the electrically induced large and abrupt change in resistance across the insulator-to-metal transition (IMT) in Vanadium Dioxide (VO_2) [34, 35], and stabilizing it with a negative feedback from a series conductance g_s.

Table 6.1: Comparison of the number of colors detected using Brelaz heuristics with those detected using a coupled relaxation oscillator circuit for various graph instances from the second DIMACS implementation challenge.

Graph	Number of Nodes	Chromatic Number χ	Brelaz Heuristics	Coupled Oscillator
huck	74	11	11	12
myciel3	11	4	4	4
myciel4	20	5	5	5
myciel5	47	6	6	6
myciel6	95	7	7	8
david	87	11	11	13
queen5_5	25	5	7	6
queen6_6	36	7	10	12
queen7_7	49	7	12	12
queen8_8	64	9	15	14
DSJC125 .1	125	-	8	9
DSJC125 .5	125	-	24	34

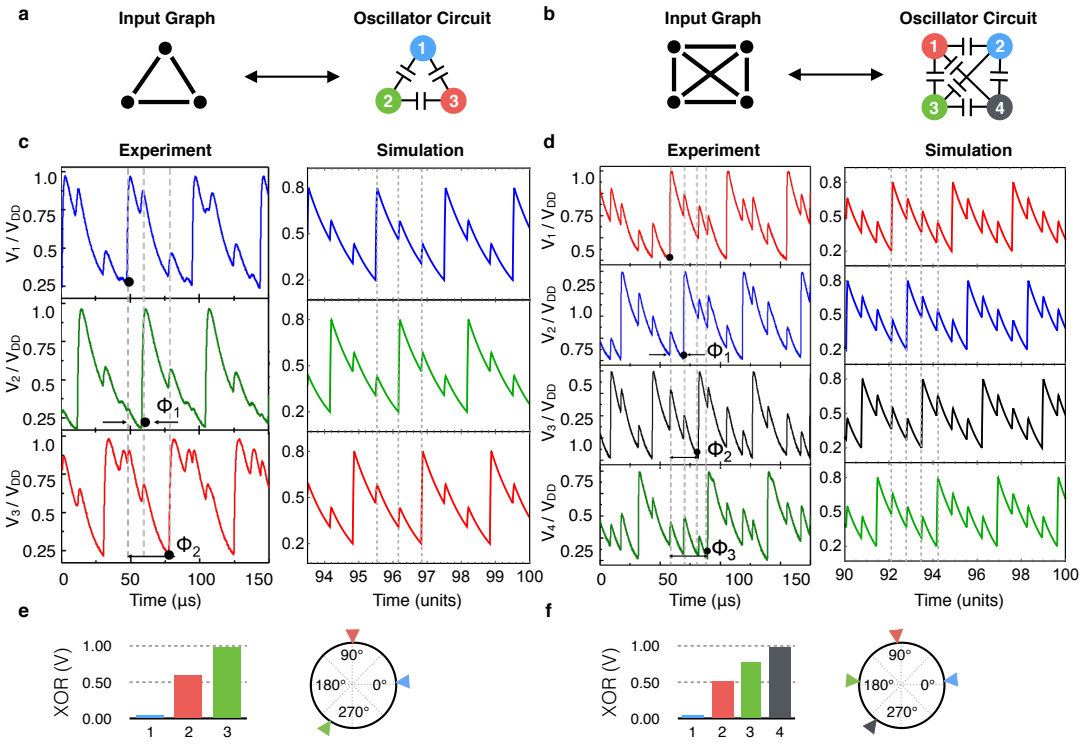

Figure 6.10: (a,b) Schematics of two representative configurations (a: delta configuration; b: cross-connected ring) of capacitively coupled VO_2 based oscillators, and their corresponding graphs. (c,d) Time domain waveforms from experiment and simulations for the two coupled oscillator configurations in (a,b), respectively, showing that while the oscillators are synchronized in frequency, no two directly coupled oscillators are in-phase. This important property of the coupled oscillator system enables graph coloring. (e,f) Time averaged XNOR of thresholded outputs of oscillators (each w.r.t. oscillator number 1), and respective polar phase plots showing steady state relative phases detected using PFDs. The XNOR values are normalized with respect to the maximum value.

Figure 6.10 shows two representative configurations of graphs (figure 6.10a: delta configuration; figure 6.10b: cross-connected ring configuration) along with their equivalent implementations using coupled oscillators. The respective time domain waveforms of the oscillators (figure 6.10c,d) reveal a unique relationship among the phases of the oscillators: there is a distinct non-zero phase difference between any two directly coupled oscillators. This is because the nature of capacitive coupling among the relaxation oscillators ensures that two adjacently connected oscillators will tend to force each other out of phase. Additionally, when an oscillator is connected to multiple other nodes, the net phase of the

oscillator is the aggregate of the 'repelling effect' of all the other connected oscillators. As such, in the light of vertex coloring, such a circuit is expected output phases which are clustered by color, i.e. oscillators with the same color have phases which are close together. But such an interpretation of oscillator phases is weak and is difficult to apply for most cases of graphs which either do not have well clustered phases or have incorrect clusters. Our interpretation of outputs as *color-sorting* solves all these problems and is well defined. As will be discussed in the next section, the combined repelling effect in a network of oscillators gives special properties to the order of phases of oscillators in steady state, viz. they approximate *minimum vertex-color-sorting*. As discussed earlier, this steady state ordering of phases is then used to calculate a *vertex-coloring*.

Since the oscillators in this work are non-sinusoidal in nature, the steady state phase differences among the coupled oscillators can be calculated using phase-frequency detectors (PFDs) or the time-averaged XNOR metric as discussed in previous chapters. The time-averaged XNOR measure of any two oscillator outputs is calculated by first thresholding the outputs to binary valued waveforms and then taking the average difference in time of these thresholded waveforms over the complete steady-state periodic orbit of the system. The time-averaged XNOR metric is proportional to the absolute value of phase difference between the oscillators, and hence it does not differentiate between lead or lag. Figures 3e,f show the relative phases detected using a PFD (shown using the polar phase plots) and the XNOR measures of each oscillator with respect to a common reference oscillator (shown as bar graphs).

Next, we experimentally investigate the coloring of some other graph configurations with up to five vertices, using the system of VO_2 based oscillators (figure 6.11). The coupled oscillators are configured to represent the respective graphs as discussed earlier, and the corresponding values of the time-averaged XOR along with the respective phase plots of the oscillators are shown in figure 6.11. It can be observed that the hardware is able to *optimally* color all the graphs investigated here.

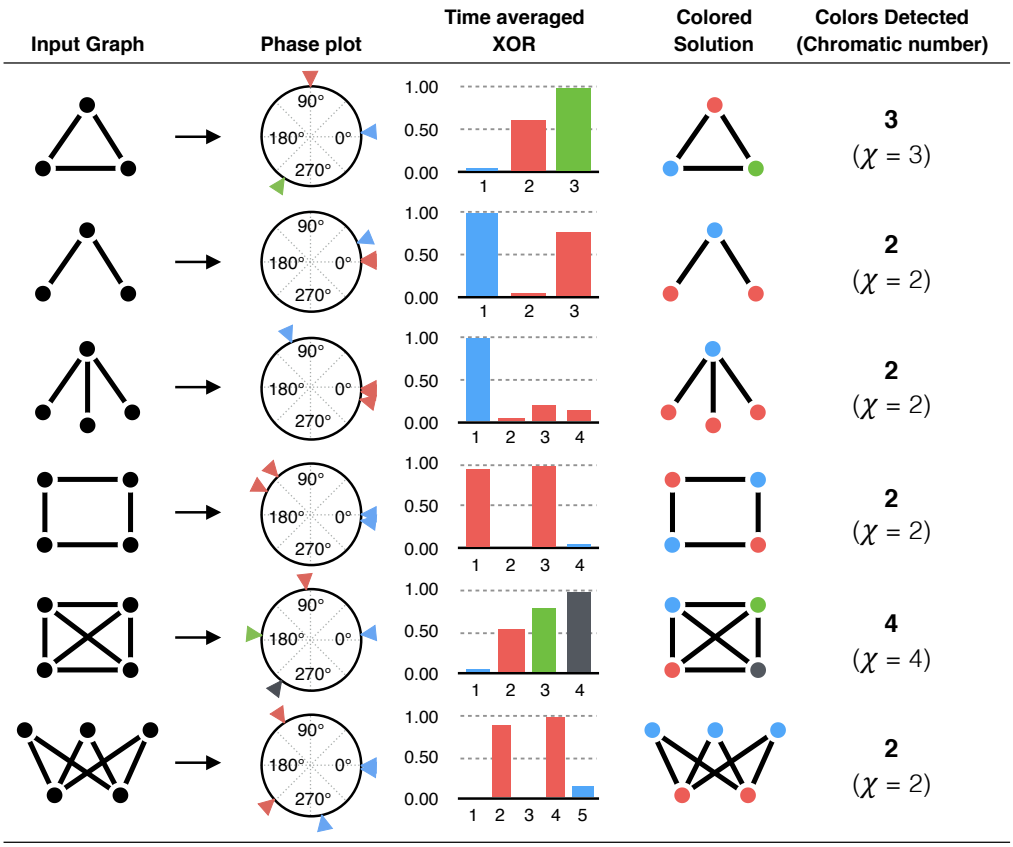

Figure 6.11: Various graph configurations, and their experimentally obtained solutions (PFD outputs and XNOR values) using the coupled relaxation oscillator system. After mapping the graphs onto the coupled oscillator hardware, the steady state order of phases of oscillators is used as a color-sorting and a color assignment is calculated.

Chapter 7

NETWORK MODELS

There has been lot of work asserting graph coloring (or some other form of clustering) capabilities of network dynamical systems, ranging from linear dynamics to coupled oscillator networks to neuron models. One reason is because the relationship of network models to coloring, or clustering, have much more general and common underlying principles. This underlying principle arises from the basic notion of framing the graph coloring problem as a minimization problem, the key elements to which are (a) the cost function, and (b) the constraints. The next section describes such formulation of the coloring problem and two other equivalent problems, their approximations, and their continuous vector relaxations. These vector relaxations are closely related to the network dynamical systems mentioned above, and as such represent the common principles that impart graph partitioning capabilities to steady states of network dynamical systems. The steady states of the IMT coupled oscillator systems are compared to two such vector relaxations - Spectral and Rank constrained SDP - and it is shown that for some connectivity patterns, the steady states of the coupled oscillator system resemble and encode solutions to these relaxations. The solution to the Spectral relaxation is the eigenvector of the adjacency matrix with most negative eigenvalue, and as such the IMT coupled oscillator model encodes an eigenvector of the adjacency matrix in its steady state.

7.1 BACKGROUND

7.1.1 *Colors, Cuts, and Clusters*

Vertex coloring [100] (or *graph coloring*) of a graph is defined as assigning a unique color to each node such that no two connected nodes receive the same color. The minimum vertex coloring problem aims to achieve this by using minimum number of total colors.

The minimum number of colors for a graph is called the *chromatic number* $\chi(G)$. Given an undirected graph G with n nodes, let the edge set be E and vertex set be V. The graph can be described using an adjacency matrix $A = \{w_{ij}\}$ which has $0/1$ elements w_{ij} depending on which edge is present in A, and is symmetric. We need to find an assignment of colors $c \in \mathbb{Z}^n$. Let δ denote the knonecker delta function defined on $\mathbb{Z}$, where

$$\delta(a,b) = \begin{cases} 0 & a = b \\ & \\ 1 & a \neq b \end{cases}, \quad a,b \in \mathbb{Z}$$

As such, the minimum graph coloring problem can be framed as follows:

$$\begin{aligned} \min_{c \in \mathbb{Z}^n} \quad & \text{distinct}(c) \\ \text{s.t.} \quad & w_{ij}\left(1 - \delta(c_i, c_j)\right) = 0 \quad \forall i, j \in V \end{aligned} \tag{7.1}$$

Another formulation of coloring is to fix the number of colors to say k, i.e. $\text{distinct}(c) = k$ and find a feasible solution. This problem is called *k-coloring*. But *k-coloring* is feasible only if $k \geq \chi(G)$, and hence, k-coloring has to be preceded by the question of *k-colorability,* which is to find whether $k \geq \chi(G)$. k-coloring and k-colorability can be considered in a combined manner in the following way. We can move the constraints to the objective by trying to minimize the number of violated constraints, which gives

$$\begin{aligned} \min_{c \in \mathbb{Z}^n} \quad & \sum_{i,j \in V} w_{ij}\left(1 - \delta(c_i, c_j)\right) \\ \text{s.t.} \quad & \text{distinct}(c) = k \end{aligned} \tag{7.2}$$

where $\sum w_{ij}\left(1 - \delta(c_i, c_j)\right)$ is the number of violated constraints, also called defects, i.e. number of monochromatic edges. This formulation does not need us to consider k-colorability

separately, because if the graph is k-colorable the optimal solution above is 0, and the argument c is the coloring. On the other hand, if the optimal solution is not 0, the graph is not k-colorable, but in this case, we get an approximate k-coloring which violates the minimum number of constraints. In this paper, we will refer to (7.2) as the *minimum defect k-coloring*.

A closely related problem to coloring is the *cut cover* problem. For any graph $G = (V, E)$ as above, a cut is defined as a partition of vertices into 2 sets such that every edge has its one end in one set, and the other end in the other set. It is obvious that a cut is exactly same as 2-coloring the graph. This can be extended to the *k-cut cover* problem as follows. A k-cut cover is partitioning the vertices into k sets such that every edge has its end in any two different sets. *As such, a cut cover is equivalent to a coloring.*

The number of cuts in a cut-cover is called the cardinality of the cut cover. The *minimum cardinality cut cover* problem is to find a cut cover with minimum number of cuts, and the minimum cardinality of any cut cover for a graph G is usually denoted by $c(G)$. It can be seen *that the minimum graph coloring problem is exactly same as the minimum cardinality cut cover problem.* The relationship between $c(G)$ and $\chi(G)$ can be written as [101]:

$$c(G) = \lceil \log(\chi(G)) \rceil \tag{7.3}$$

This relationship can be derived by constructing a coloring using a cut cover. If we have a cut cover with p cuts, then let us assign a binary vector $\mathbf{x}_i$ of dimension p to each node i. Also, let us say that every cut divides the vertices into two sides - left side (0) and the right side (1). Now for every cut j, assign the j^{th} component of $\mathbf{x}_i$ to 1 or 0 depending on which side of the cut the node lies. Using this process, we have assigned a p dimensional binary vector to every node such that no two nodes connected by an edge recieves the same vector. If every binary vector used in the graph is mapped to a unique color, then we have a valid coloring with colors no more than 2^p. Similary, a cut cover can be easily constructed

using a coloring. Based on these conversions, we can get the equality of (7.3) as was done in [101].

The relationship of the above two problems with cliques is also a simple deduction. Coloring a graph is same as finding cliques in the complementary graph. This is because in a coloring, if we consider the nodes with the same color, none of them are connected. This means in the complementary graph, they all will be connected to each other. To define it formally, every coloring corresponds to a *clique*-partition, which is a covering of all the vertices using cliques, in the complementary graph. Hence, minimum graph coloring is equivalent to the *minimum clique partition* problem in the complementary graph where the number of cliques has to be minimized. Approximation of clique partition is in general referred to as *graph clustering* [102], where the task is to group the vertices into clusters in such a way that there should be many edges within each cluster and relatively few between the clusters.

The importance of considering clique partitions is that it relates the clustering problems to coloring problems. The most ideal clustering problem would be formulated on graphs made of disjoint cliques, where each clique is a cluster. What is less obvious is the relationship of approximations of clique partition to those of coloring and cut covers, and in turn their relationship to continuous network dynamical systems.

7.1.2 *Vector relaxations*

The coloring problem can be relaxed by assigning vectors instead of colors to each node. This is called vector coloring. The notion of distinct colors is captured by inner prodcts, where two vector colors are considered different if they have low inner product. Finally, the last step is to convert a vector coloring to a coloring, i.e. partition the vectors $\{\mathbf{v}_i\}$ into k clusters, which can be done by any usual clustering algorithm like the K-means algorithm.

As such, we arrive at the well-known semidefinite relaxation of max-k-cut [103]:

$$\begin{aligned} \min_{\mathbf{v}_i \in \mathbb{R}^n} \quad & \sum w_{ij} \mathbf{v}_i \cdot \mathbf{v}_j \\ \text{s.t.} \quad & \langle \mathbf{v}_i, \mathbf{v}_i \rangle = 1 \quad \forall i \in V \end{aligned} \tag{7.4}$$

Although this process converts a coloring problem, which itself is a form of clustering, to another clustering problem, the preprocessing with the inner product based *semidefinite program* helps cluster the vertices more closely. To see this, lets consider coloring as a connectivity based clustering problem without the above inner product preprocessing. This can be done by assigning the i^{th} column of the $\{1,-1\}$-adjacency matrix of the graph as the vector-color of the i^{th} node and then perform the same clustering. Consider two adjacent nodes i and j and their respective vectors (columns) $\mathbf{w}_i$ and $\mathbf{w}_j$ from the adjacency matrix. Their inner product can be as high as $(n-4)/n$ which is much larger than $-1/(k-1)$ which is targeted by the kind of preprocessing mentioned above.

The other comon vector relaxation of graph coloring is the spectral relaxation [89] which aims to find a coloring using eigenvectors of $W = \{w_{ij}\}$ (the adjacency matrix) which have the most negative eigenvalue(s). For instance, to 3 color a graph, this method finds two eigenvectors of the adjacency matrix with the most negative eigenvalues and uses their components to assign a 2D vector to each node which is used for coloring. Similar spectral relaxation for clustering also exists [104].

7.1.3 *Continuous network dynamics*

Many continuous dynamical systems for computing have been proposed, some of which are a model of a physical system and some aren't. A majority of these systems are proposed for graph partitioning. In this section we review the common properties of some of these dynamical systems and their connection with the relaxations described in the previous sections.

7.1.3.1 *Linear Dynamics - Raleigh Quotient Gradient Flow*

A gradient descent dynamical system for the spectral relaxation can be easily created to find the eigenvectors $\mathbf{v}_i$ of W by minimizing the function:

$$\mathbf{v}_i = \arg\min_{\mathbf{x}} \frac{\mathbf{x}^T W \mathbf{x}}{\mathbf{x}^T \mathbf{x}}$$

which yields various $\mathbf{v}_i$ as local minima. Here, $\mathbf{x}^T W \mathbf{x}/\mathbf{x}^T \mathbf{x}$ is also called the **Rayleigh Quotient**, and the corresponding gradient descent the **Raleigh Quotient Gradient Flow.** Although simple to write, this gradient descent dynamical system is very difficult to construct in a hardware mainly because of the normalization $\mathbf{x}^T \mathbf{x}$ in the denominator which is a global function.

It is important to note here that for clustering, usually the eigenvectors of the Laplacian matrix are used instead of the Adjacency matrix. This is because usually the interpretation of clustering is not the *minimum clique partition* which uses $\sum w_{ij} \mathbf{v}_i \cdot \mathbf{v}_j$ as the objective function, but instead another interpretation which uses $(1/2)\sum w_{ij}(\mathbf{v}_i - \mathbf{v}_j)^2$ as the objective function. It can be easily seen that:

$$\frac{1}{2}\sum w_{ij}(\mathbf{v}_i - \mathbf{v}_j)^2 = \sum l_{ij} \mathbf{v}_i \cdot \mathbf{v}_j$$

where $L = \{l_{ij}\}$ is the Laplacian matrix. As such, in this interpretation of clustering, the spectral properties of the laplacian matrix are the solutions for clustering. Due to this importance of eigenvector of Laplacian matrix, the second eigenvector of the Laplacian matrix is called the Fiedler vector [104].

7.1.3.2 *Lattice Models*

Lattice models are models about solid state lattices, which assume some simplistic interaction behavior between neighboring atoms or molecules to explain macroscopic phenomena. Although the graphs involved in these lattice models are only neighborhood lattice graphs,

we will be considering these models over general graphs. This also highlights that the kinds of models used in various fields are very similar, but vary only in few characteristics, like the connectivity graphs. Such simplistic assumptions in the initial works on lattices were justified because the major objective was to find some "mean" critical properties at the macroscopic level arising from the microscopic interactions. The details of nature of interactions at the microscopic level does not have significant effects on the mean macroscopic properties. It should be noted that when the focus is shifted from the mean macroscopic properties to computing behavior, we are looking for complex details even at the macroscopic level, and as such, simplifying assumptions about interactions and universality may no longer be justified.

One particular example of a lattice model which will be used here is the XY model. The XY lattice model is a 2D lattice model, which means each lattice point is associated with a 2D vector, say $\mathbf{v}_i$ and the overall energy of the physical system is assumed to be $\sum w_{ij}\mathbf{v}_i \cdot \mathbf{v}_j$. The ground state is the stable state of the lattice when the energy is minimized. As such, this model is equivalent to the relaxation model of 7.4 as discussed above with he additional constraint that the number of partitions is 3 (because the dimension of $\mathbf{v}_i$ is constrained 2). As such, it is exactly a **Rank-2 constrained Semidefinite Program**.

7.1.3.3 *Coupled oscillators*

As we are discussing coupled oscillators, it is imperative to consider already existing coupled oscillator models. Also, there have been some incomplete studies indicating some coloring capabilities in the phase dynamics of these models. Here, it is shown why they are incomplete, how can they be made complete, and how these models are essentially equivalent to the XY models discussed above. The most commonly known model is the Kuramoto model. This model assigns a single scalar θ_i to each node (or oscillator) which is the phase of the oscillator. As such, the complete state of the coupled oscillator system can be described by the phases θ_i. The time evolution of the phases of each oscillator is

given by:

$$\frac{\partial \theta_i}{\partial t} = f_i + \sum_j w_{ij} \sin(\theta_i - \theta_j)$$

where w_{ij} is the connection between i^{th} and j^{th} nodes as before and f_i is the intrinsic frequency of i^{th} oscillator. With some transformations, it can be seen that this model is exactly the gradient descent of the XY model, as shown below. The frequencies f_i are assumed equal for all i, i.e. $f_i = f, \forall i$.

As $\mathbf{v}_i$ are 2 dimensional unit vectors in the XY model, they can be written as $\mathbf{v}_i := (\cos\phi_i, \sin\phi_i)$. Also, $\mathbf{v}_i \cdot \mathbf{v}_j = \cos(\phi_i - \phi_j)$. Hence, the energy function for the XY models is

$$E_{XY} = \sum_i \sum_{j<i} w_{ij} \mathbf{v}_i \cdot \mathbf{v}_j = \sum_i \sum_{j<i} w_{ij} \cos(\phi_i - \phi_j)$$

and the gradient descent for this energy is

$$\frac{\partial \phi_k}{\partial t} = -\frac{\partial E_{XY}}{\partial \phi_k} = \sum_i w_{ki} \sin(\phi_k - \phi_i)$$

It can be easily seen that this gradient descent is equivalent to the Kuramoto model with a simple change of variables - $\theta_i(t) = ft + \phi_i(t)$.

7.2 THIS WORK

7.2.1 *Characterizing IMT coupled oscillators as a network model*

As discussed in the above section, there are two simplest dynamical system network models whose steady states correspond to some kind of graph partitioning. As the circuit for the IMT coupled oscillator system is also a very simple circuit with elements of linear dynamics, it would be useful to compare the above discussed two models - Linear, and XY (Kuramoto) model, with the IMT coupled oscillator model in terms of their similarity of

Table 7.1: Comparison of various dynamical systems, their analogous algorithms and their energy landscape

Dynamical System	**Algorithm**	**Vector output**	**Energy landscape**
Raleigh Quotient Gradient Flow	Gradient descent of Spectral relaxation	Eigenvector closest to initial vector	Non-Convex, but with fixed (<=n) number of local minima
Kuramoto (XY)	Gradient descent of Rank-2 constrained SDP	Ground state of XY converted to polar form as single vector of oscillator phases	Non-Convex
Hysteresis + R	-	Steady state spike times with reference to the first spike in the limit cycle	Non-Convex

local minima, basins of attraction, and performance of coloring. This comparison also highlights whether the basic elements present in the simplest network models are present in the IMT coupled oscillator model which impart coloring capabilities to its steady state. These models are summarized below. All these models have non-convex energy landscapes, and as such for comparison the direction of the initial vector for simulations is chosen the same - $[1, 1, 1, ...]$. This initial vector also represents the bias, or prior information we have about coloring the given graph, and a vector of 1s represent no bias. As they all produce a vector output, with one scalar associated with each node, the post-processing of this vector output for coloring is exactly the same for all models.

7.2.1.1 *Similarity of local minima*

To compare the similarity of solutions, we first create random graphs using the same random graph model as in previous chapter $G(n,k,i)$ to generate instances of colorable k-partite graphs with total n nodes. The graphs are generated by first choosing a random k-partition of n nodes, then creating a complete k-partite graph with this k-partition and finally removing random i number of edges from this complete graph. *Average connectivity* p is defined as the ratio of total number of edges in the generated graph $G(n,k,i)$ to the total number of edges in the complete k-partite graph with the same partition. For this comparison, we generate graphs with $n = \{50,100,150,200\}$, $c = \{3,5,7,9\}$, $p = \{0.5,0.6,...,1.0\}$, 50 random partitions for each c and 5 initial conditions for each graph. For each graph, we run the 3 models using 5 initial conditions chosen at random $x_0 \in [0.4,0.6]^n$.

BASED ON PLANTED PARAMETERS Figures 7.1 and 7.2 show the inner products between the models and how the distributions of these inner products change as the structure of the adjacency matrix varies. The adjacency matrix derives its stucture from the planted partition model, and hence its structure inherits 2 basic parameters from the generation model - the number of planted partitions (colors) and the edge density. As can be seen, for 3 partitions, the inner products of the 3 models are high (angles are low) and as the number of partitions increase, the angles increase. Also, the edge density affects the inner products, where complete partite graphs have higher inner products which decrease as the edge density reduces.

BASED ON THE ADJACENCY MATRIX The analysis using planted parameters are based on prior information about the random generating model. Here we restrict to posterior information of the given adjacency matrix, which is to say restricting to some function of the adjacency matrix A itself, without considering the planted parameters. The previous observation about the dependence on the planted parameters imply that rank of A would be

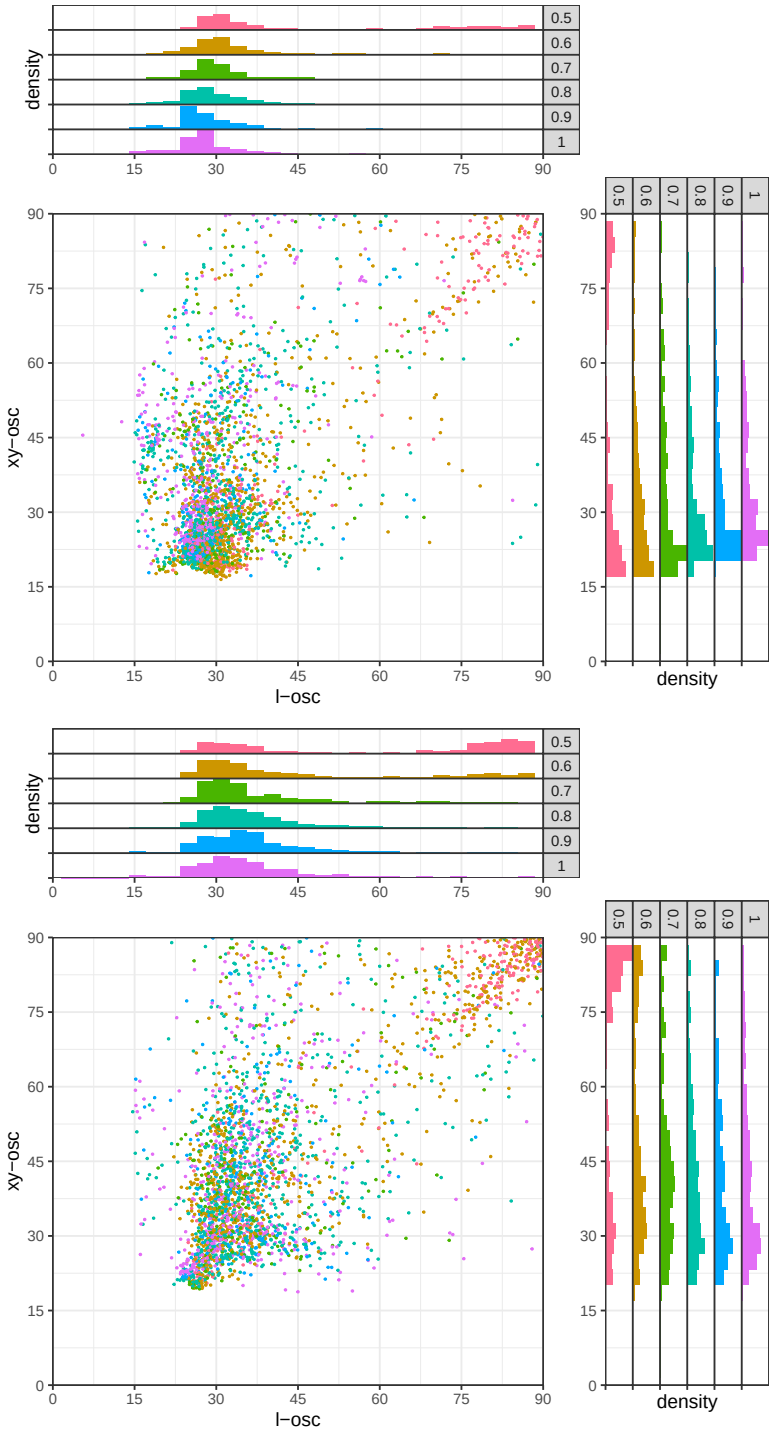

Figure 7.1: Scatter plots with marginal histograms of inner products of IMT oscillator model with linear and XY models for 200 nodes with (top) 3 colors and (bottom) 5 colors in the planted partition model.

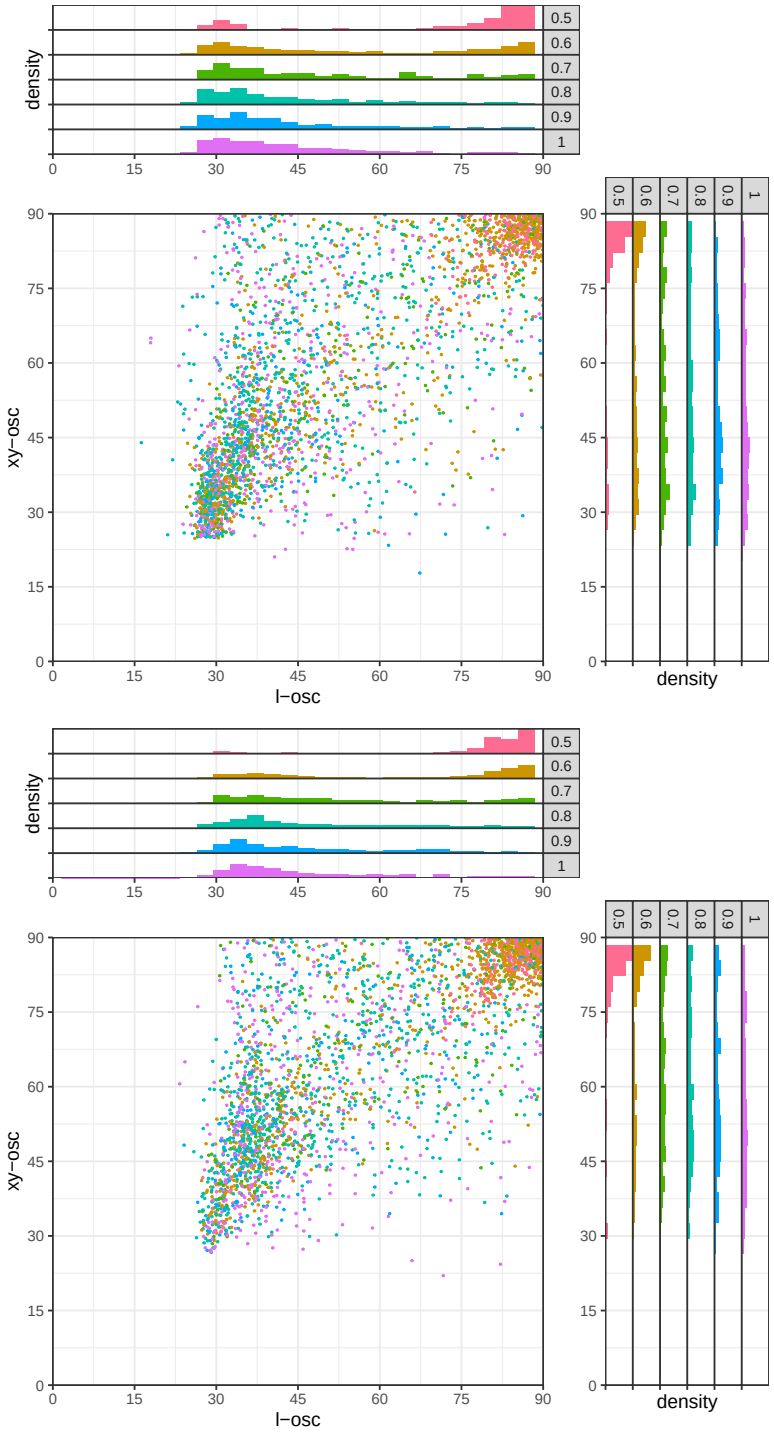

Figure 7.2: Scatter plots with marginal histograms of inner products of IMT oscillator model with linear and XY models for 200 nodes with (top) 7 colors and (bottom) 9 colors in the planted partition model.

a good metric for characterizing the inner products. But the rank of a matrix is a discrete function which is also very sensitive to matrix elements.

Instead of rank, we can look at some relaxations of rank like the nuclear norm $||A||_*$. Figure 7.3 shows $\mathbf{v}_{osc} \cdot \mathbf{v}_l$ plotted against the nuclear norm $||A||_*$. We define another kind of norm of the adjacency matrix $||A||_{tre}$ which gives better predictability as shown in the same figure. These norms are defined as

$$||A||_{tre} = \log(\mathrm{tr}(e^{-A})) = \sum_i e^{-\lambda_i}$$
$$||A||_* = \mathrm{tr}(\sqrt{A^T A}) = \sum_i |\lambda_i|$$

where λ_i are the eigenvalues of the adjacency matrix.

7.2.1.2 *Coloring performance*

We can also compare the coloring performance of the three models. We find the number of colors detected for each graph and x_0 for the three models. These graphs are grouped into classes of $\{n, c, p\}$. For each class, we note the number of instances when IMT oscillator system achieves minimum colors as min_{osc}. Similarly min_l and min_{xy} are defined. For ties between 2 models, 1/2 points are counted for each model, and for 3-way ties 1/3 points are counted. As such, we arrive at a triplet $\{min_{osc}, min_l, min_{xy}\}$ for each class. Note that $min_{osc} + min_l + min_{xy} = k$ for a constant k which is same across all classes. As such, we can make a ternary plot of the these points as shown in Figure 7.4 where each point denotes a class, colored by the edge density p. An interesting observation here is that if we find the quantity $\log_c n$ for each class, then as this quantity decreases, the points shift more towards min_{osc}, i.e. for larger $\log_c n$ the IMT oscillator model performs better. This is shown as arrows on the lines joining the classes with the same p.

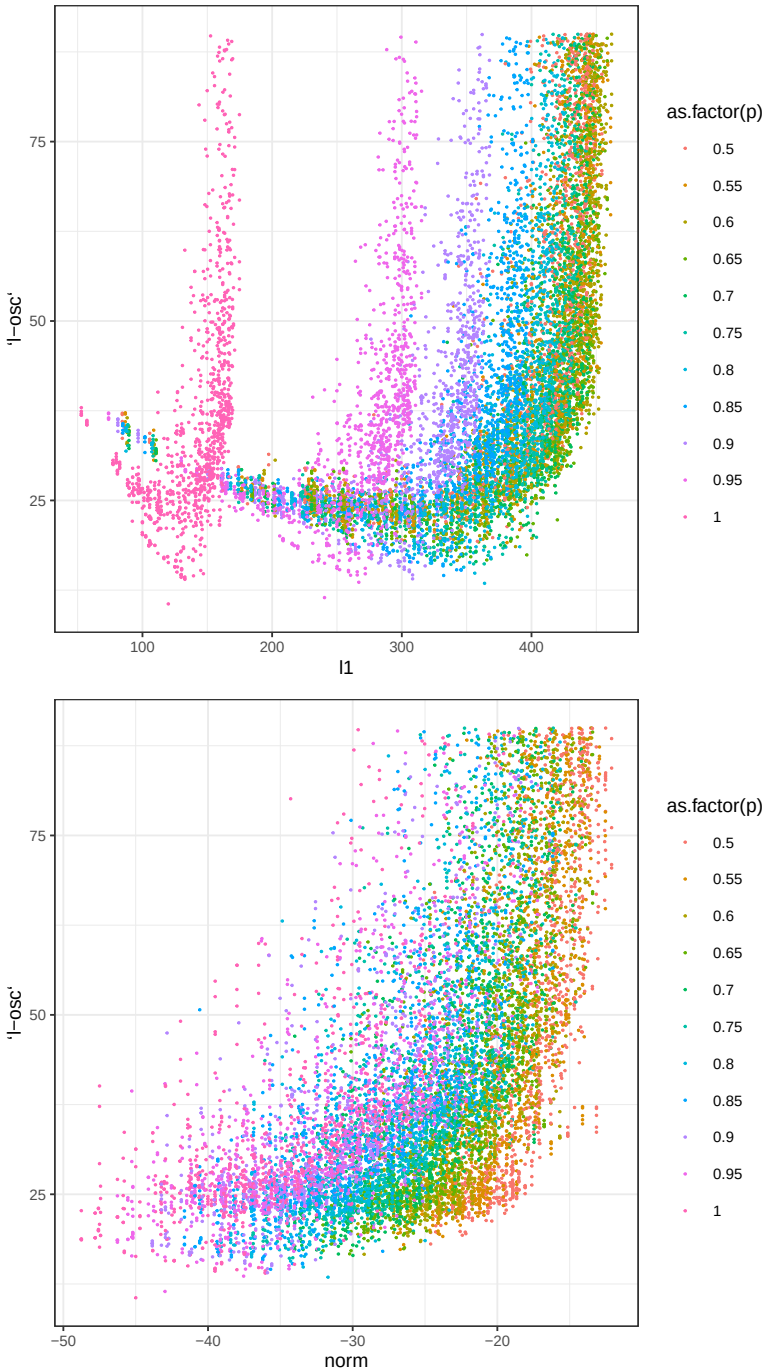

Figure 7.3: Inner products $\mathbf{v}_{osc} \cdot \mathbf{v}_l$ as a function of (Top) $||A||_*$ and (Bottom) $||A||_{tre}$

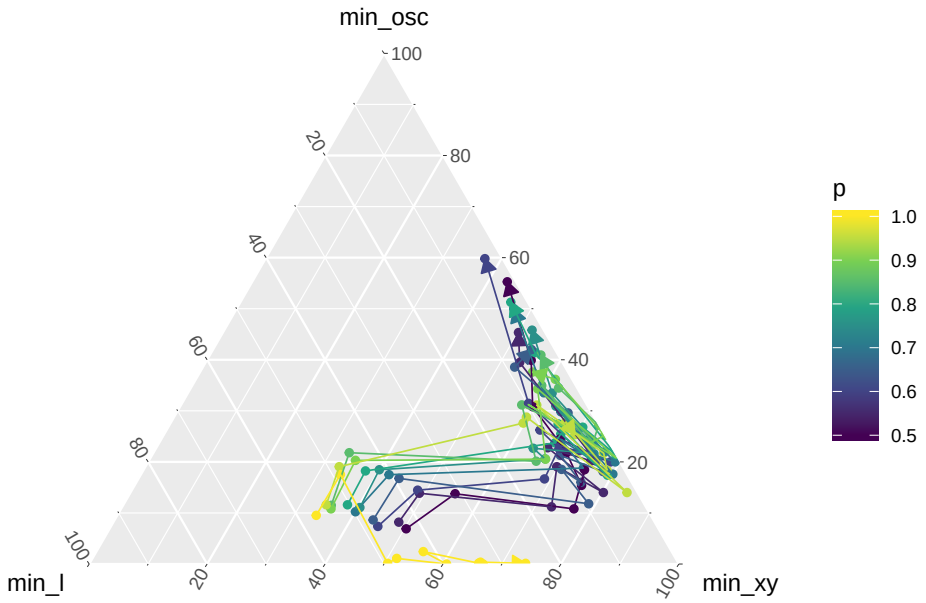

Figure 7.4: Ternary plot of the proportion of instances in each class for which each model finds the minimum colors.

Chapter 8

TOWARDS A CMOS IMPLEMENTATION

This chapter deals with the challenges in designing a CMOS coupled oscillator chip. The major objectives of this design are:

1. **100 Oscillators** - Schmitt trigger oscillators which resemble the D-D kind os oscillators discussed earlier.

2. **All-to-all connectivity** - Each oscillator is capacitively coupled to all other oscillators.

3. **Programmable connections** - Each connection is programmable, i.e. the capacitive coupling can be switched on/off.

8.1 DESIGN CHALLENGES

This kind of design has following challenges:

1. This is an *analog-on-top* design, which means the whole circuit is a big analog block, as opposed to different analog blocks interacting digitally. The current EDA tools cannot automate the placement and routing of the number of analog blocks in a 100 coupled oscillator chip. For instance, the number of coupling blocks in a 100 all-to-all connected coupled oscillator circuit is $1/2 \times 100 \times 99 = 4950$.

2. All-to-all connectivity for 100 oscillators with 4950 connections can be very hard to implement physically on a 2D chip with limited number of metal layers. Also ensuring symmetry, like the length of connection wires between the oscillators can be very challenging.

3. As the circuit involves switching, the simulation complexity and time increases a lot with the number of oscillators. Also, the number or test instances (adjacency matrices) are too many to run simulations for verification.

4. The parameter space (coupling capacitances, oscillator frequencies, oscillator internal capacitances and resistances etc.) have to be explored with respect to the final computational outcome of either graph coloring, or eigenvector computation, using the synchronized phases. It can be hard to exactly define the metric that distinguishes better parameters from the worse ones.

5. Characterizing the effect of noise on the steady state synchronization of oscillators can be very hard.

8.2 OSCILLATOR DESIGN

A schmitt trigger oscillator was chosen as the oscillator design because it resembled the D-D oscillator configuration, and hence would show similar switched linear network dynamics as the IMT coupled oscillators analysed before. The usual schmitt trigger oscillator was modified to increase the oscillation amplitude as shown in Figure 8.1.

8.3 LOADER CIRCUIT

As mentioned in Chapter 6, loading capacitances are needed at each oscillator node to convert the Laplacian coefficient matrix to Adjacency matrix. This loader circuit is shown in Figure 8.2, which is a programmable bank of capacitors and is programmed based on the input Adjacency matrix.

8.4 PHASE MEASUREMENT

The phase measurement is done by using a fast clock and counting the number of clock cycles it takes from a reference time point (specified by a step signal M) to the first edge

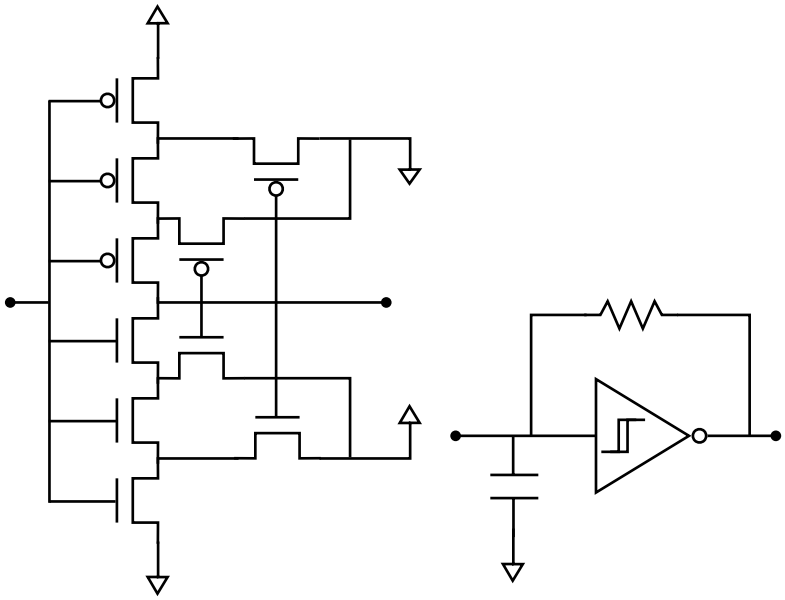

Figure 8.1: Modified schmitt trigger and corresponding oscillator schematic

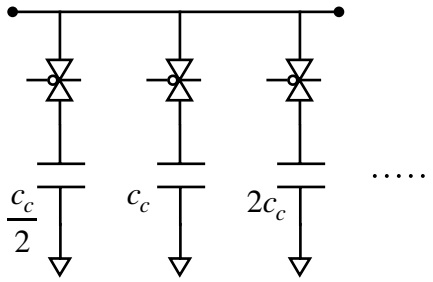

Figure 8.2: The loader circuit is a programmable bank of capacitors

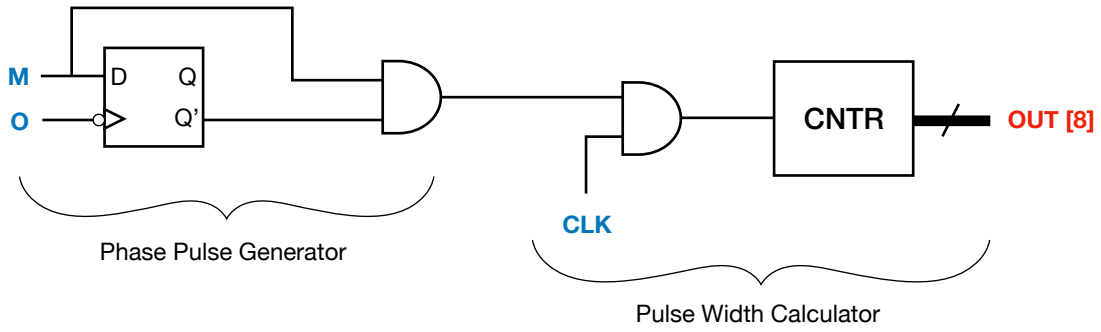

Figure 8.3: Phase measurement using a reference signal M

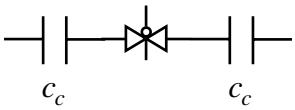

Figure 8.4: The programmable capacitive coupling block

of the square wave output of each oscillator. The circuit of this phase read out is shown in Figure 8.3.

8.5 CONNECTIVITY ARRAY

The connectivity array is the most challenging part of this design because connecting all 100 oscillators to all other 100 oscillators is challenging on a 2D chip with limited number of metal layers available for routing. The programmable coupling circuit is shown in Figure 8.4. To achieve all-to-all connectivity, instead of arranging oscillators in a grid, they need to be arranged in a line as shown in Figure 8.5. This makes it possible to place the connectivity blocks in a triangle pattern which resemble the lower triangle of the adjacency matrix as well. After the placement, the routing can be done by connecting the oscillator outputs to the loader circuit as well as the corresponding rows of the connectivity array.

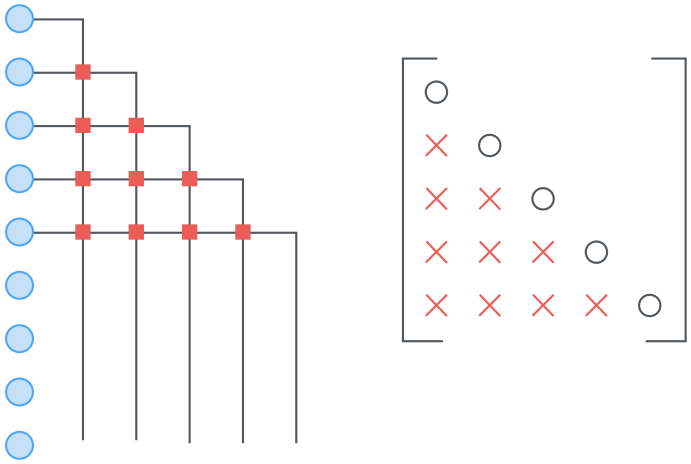

Figure 8.5: The conectivity array designed by placing the oscillators in a line

8.6 COUPLED OSCILLATOR NETWORK

The overall floorplan and architecture of the complete coupled oscillator circuit is shown in Figure 8.6. The final chip layout is shown in Figure 8.7, and the die shot is shown in Figure 8.8. At the time of writing this thesis, the measurement data was not available.

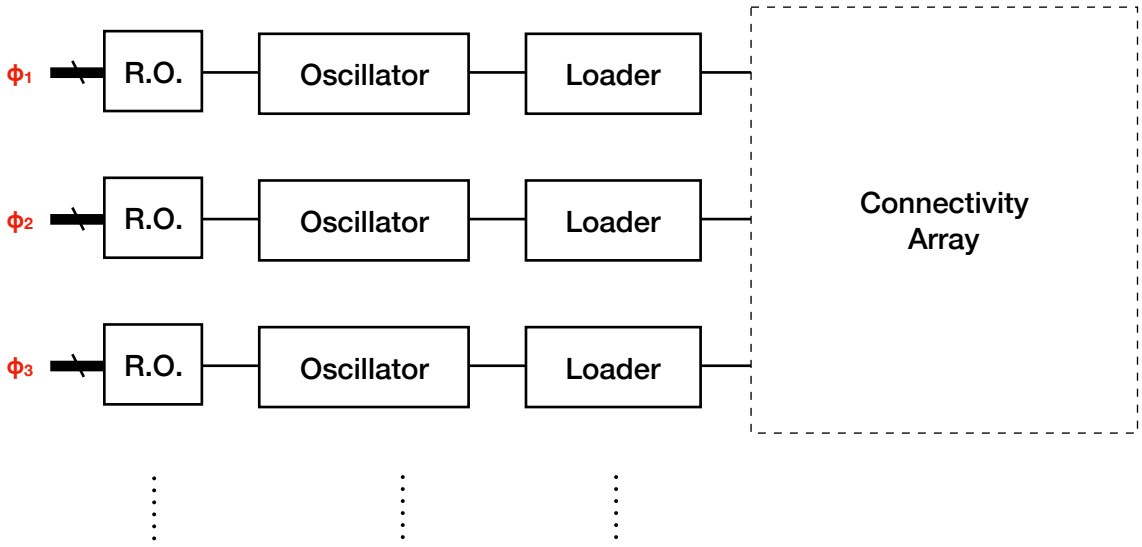

Figure 8.6: Floorplan of the coupled oscillator network

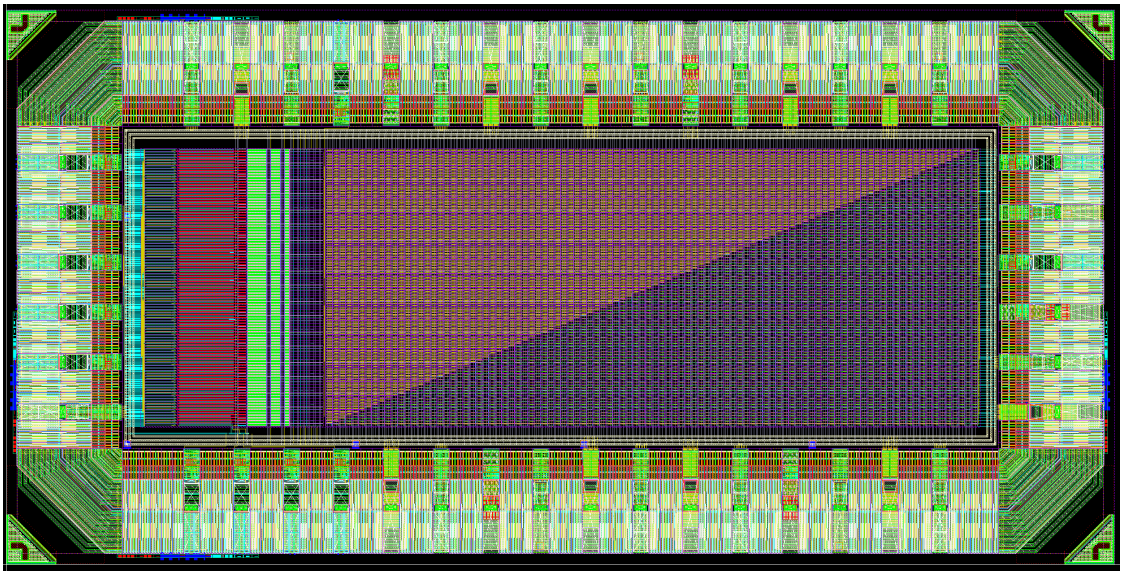

Figure 8.7: Physical design layout of the coupled oscillator chip

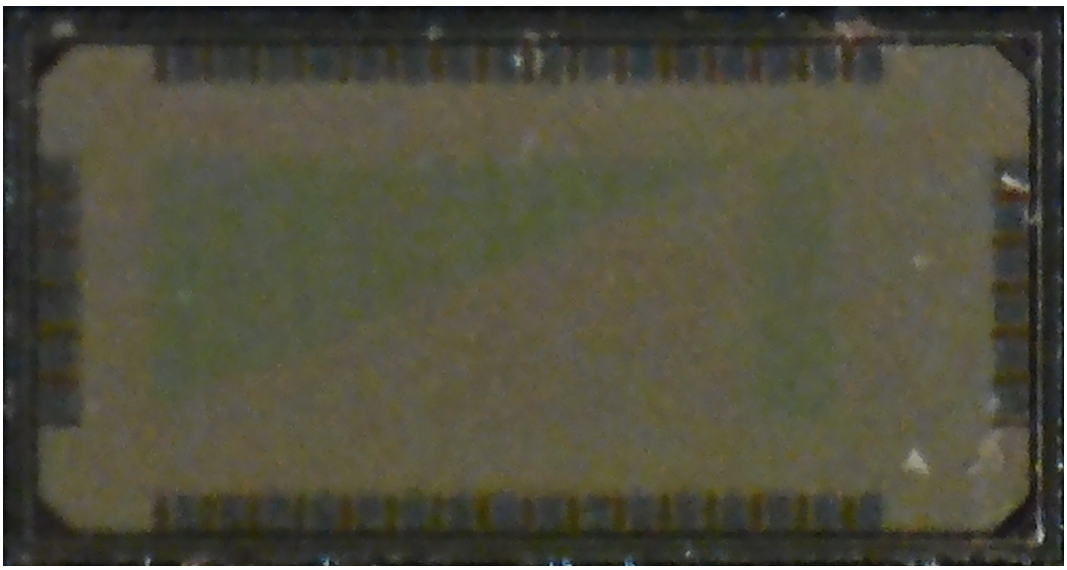

Figure 8.8: Die shot of the coupled oscillator chip

Appendix A

MATHEMATICAL RESULTS

A.1 THE COEFFICIENT MATRIX IN PROTOTYPICAL CASE

In this section we give an analytical treatment of the structure of the coefficient matrix and its eigen spectrum in the prototypical case. We consider the prototypical case where the graph is complete and the number of nodes in each color class is equal. When n identical oscillators with internal capacitances c_i are connected in a k-partite graph, and the coupling is purely capacitive with same coupling capacitances c_c used for all pairs, then the system evolution is described as in equation 6.2. In the simple case when each partition has equal number of nodes $m = n/k$, then more can be said about the coefficient matrix $B = (c_i I - c_c A + c_c nI)^{-1}$. Let $F = (c_i I - c_c A + c_c nI)^{-1}$ so that $B = F^{-1}$. Then F can be written as a repeated partitioned matrix as

$$F = U \otimes G + V \otimes E$$

where $\otimes$ is the kronecker product of matrices, U and V are $k \times k$ matrices, G and E are $m \times m$ matrices, and the matrices are given by

$$\begin{aligned} U &= c_{ic} I_k \\ G &= I_m \\ V &= I_k - J_k \\ E &= c_c J_m \end{aligned}$$

with I_m being the $m \times m$ identity matrix, J_m the $m \times m$ matrix with all ones, and $c_{ic} = (c_i + nc_c)$.

A.1.1 *Eigenvectors of B in prototypical case*

For n nodes and k color classes, let U be a $n \times m$ matrix where each column vector corresponds to one color class where the components of that particular class are k/n and rest are 0. As such, U^TAU is a $k \times k$ matrix with each entry equal to the average of entries of the corresponding block in A. In the simple case of complete graph with equal number of nodes in each class, $U^TAU = J - I$ where J is a square matrix of all ones and I is the identity matrix. If x is an eigenvector of U^TAU then

$$\begin{aligned} U^TAUx &= \lambda x \\ UU^TA(Ux) &= \lambda(Ux) \end{aligned}$$

Now UU^TA is just the scaled version of A and hence,

$$\alpha A(Ux) = \lambda(Ux)$$

Therefore if x is an eigenvector of U^TAU then Ux is an eigenvector of A. Also the number of non-zero eigenvalues of A are k which is equal to the rank of U^TAU which is full-rank. Hence all the eigenvectors of A can be described using the eigenvectors of U^TAU and they have equal components in a single color class. $J - I$ has an eigenvalue -1 with multiplicity $n-1$, and an eigenvalue $n-1$, and so does A. Now the eigenvectors of B with the least negative eigenvalues are same as that of A with most negative eigenvalues (Proposition 1). Hence, the eigenvalues of B with least negative eigenvalues are constant on each color class.

A.1.2 *Structure of the inverse of F in prototypical case*

Proposition 9. *If $F = (c_i I - c_c A + c_c n I)$ is the coefficient matrix of the network, then $B = F^{-1}$ has the same partitioned form as F. More precisely, $B = F^{-1}$ can be written as*

$$F^{-1} = \frac{1}{c_{ic}} \left(\frac{1}{c_{ic}} U \otimes G + D \otimes E \right)$$

where U, G and E are the same matrices that describe F, c_{ic} is as defined above, and D is a $k \times k$ matrix given by

$$D = \frac{1}{c_i + (n+m)c_c} (\beta J_k - I_k)$$

and

$$\beta = \frac{c_i + nc_c}{c_i + mc_c}$$

Proof. As described above, $F = U \otimes G + V \otimes E$. Here G is a identity matrix and E is a rank 1 matrix. Hence, as shown in [105], the inverse for F can be calculated as

$$F^{-1} = U^{-1} \otimes G - [U + (\mathrm{tr}\, E) V]^{-1} V U^{-1} \otimes E$$

Now,

$$\begin{aligned}
\mathrm{tr}\, E &= mc_c \\
U^{-1} &= \frac{1}{c_{ic}} I_k \\
V U^{-1} &= \frac{1}{c_{ic}} (I_k - J_k) \\
[U + (\mathrm{tr} E) V]^{-1} &= [U + mc_c V]^{-1} \\
&= [(c_i + (n+m)c_c) I_k - mc_c J_k]^{-1} \\
&:= [P - Q]^{-1}
\end{aligned}$$

As Q is a rank 1 matrix, we can use another result from [105]:

$$\begin{aligned}
[U+(\mathrm{tr}E)V]^{-1} &= [P-Q]^{-1} \\
&= P^{-1}+\frac{1}{1-\mathrm{tr}QP^{-1}}P^{-1}QP^{-1} \\
&= \frac{1}{c_i+(n+m)c_c}I_k+\frac{1}{1-\frac{nc_c}{c_i+(n+m)c_c}}\frac{1}{(c_i+(n+m)c_c)^2}mc_cJ_k \\
&= \frac{1}{c_i+(n+m)c_c}\left(I_k+\frac{mc_c}{c_i+mc_c}J_k\right)
\end{aligned}$$

Combining the parts, and noting that $J_k^2 = kJ_k$, we get

$$\begin{aligned}
[U+(\mathrm{tr}E)V]^{-1}VU^{-1} &= \frac{1}{c_i+(n+m)c_c}\left(I_k+\frac{mc_c}{c_i+mc_c}J_k\right)\frac{1}{c_{ic}}(I_k-J_k) \\
&= \frac{1}{c_{ic}(c_i+(n+m)c_c)}(I_k-\beta J_k)
\end{aligned}$$

where,

$$\beta = \frac{c_i+nc_c}{c_i+mc_c}$$

Finally,

$$F^{-1} = \frac{1}{c_{ic}}\left[I_k\otimes I_m+\frac{1}{c_i+(n+m)c_c}(\beta J_k-I_k)\otimes c_cJ_m\right]$$

and hence,

$$B = F^{-1} = \frac{1}{c_{ic}}\left(\frac{1}{c_{ic}}U\otimes G+D\otimes E\right) \tag{A.1}$$

□

A.1.3 *Column vector of B in prototypical case*

Using equation A.1 we can deduce properties of the column vector of B.

Proposition 10. *Let B_k be the k^{th} column vector of B and B_{kl} be the $(k,l)^{th}$ element of B. For the components of B_k there are only 3 kinds of values.*

1. *For the k^{th} component,*

$$B_{kk} = \frac{1}{c_{ic}}\left(1+\alpha(\beta-1)\right)$$

2. *For all other components in the same class as the k^{th} component, i.e. when k^{th} and l^{th} node are in the same color class*

$$B_{kl} = \frac{1}{c_{ic}}\alpha(\beta-1)$$

3. *For all other components of B_k which are not in the same partition/color class as the k^{th} node, i.e. when k^{th} and j^{th} node are not in the same class*

$$B_{kj} = \frac{1}{c_{ic}}\alpha\beta$$

where

$$\alpha = \frac{c_c}{c_i+(n+m)c_c}$$

4. *The difference between B_{kl} and B_{kj} w.r.t. B_{kk} is given by:*

$$\frac{B_{kj}-B_{kl}}{B_{kk}} = \frac{1}{r+n+m+\frac{n-m}{r+m}}$$

where $r = c_i/c_c$. As can be seen, this difference can be made very small by weak coupling, i.e. $c_c \ll c_i$, but more importantly for increasing n and m this difference reduces

BIBLIOGRAPHY

1. Toffoli, T. *What Are Nature's natural Ways Of Computing?* in *Workshop on Physics and Computation* (1992), 5–9.

2. Vergis, A., Steiglitz, K. & Dickinson, B. The complexity of analog computation. *Mathematics and Computers in Simulation* **28,** 91 –113 (1986).

3. Li, Y. *et al.* Probing Phase Coupling Between Two Spin-Torque Nano-Oscillators with an External Source. *Physical Review Letters* **118,** 247202 (June 2017).

4. Lebrun, R. *et al.* Mutual synchronization of spin torque nano-oscillators through a long-range and tunable electrical coupling scheme. en. *Nature Communications* **8,** ncomms15825 (June 2017).

5. McMahon, P. L. *et al.* A fully-programmable 100-spin coherent Ising machine with all-to-all connections. en. *Science,* aah5178 (Oct. 2016).

6. Pufall, M. R. *et al.* Physical Implementation of Coherently Coupled Oscillator Networks. *IEEE Journal on Exploratory Solid-State Computational Devices and Circuits* **1,** 76–84 (Dec. 2015).

7. Shukla, N. *et al.* Synchronized charge oscillations in correlated electron systems. *Scientific Reports* **4,** 4964 (May 2014).

8. Tang, C. L., Bosenberg, W. R., Ukachi, T., Lane, R. J. & Cheng, L. K. Optical parametric oscillators. *Proceedings of the IEEE* **80,** 365–374 (1992).

9. Barends, R. *et al.* Digitized adiabatic quantum computing with a superconducting circuit. en. *Nature* **534,** 222–226 (June 2016).

10. Dörfler, F. & Bullo, F. Exploring synchronization in complex oscillator networks. *arXiv preprint arXiv:1209.1335* (2012).

11. Winfree, A. T. Biological rhythms and the behavior of populations of coupled oscillators. *Journal of theoretical biology* **16,** 15–42 (1967).

12. Kuramoto, Y. *Self-entrainment of a population of coupled non-linear oscillators* in *International symposium on mathematical problems in theoretical physics* (1975), 420–422.

13. Kuramoto, Y. *Chemical oscillations, waves, and turbulence* (Courier Dover Publications, 2003).

14. Nikonov, D. E. *et al.* Coupled-Oscillator Associative Memory Array Operation for Pattern Recognition. *IEEE Journal on Exploratory Solid-State Computational Devices and Circuits* **1,** 85–93 (Dec. 2015).

15. Hoppensteadt, F. C. & Izhikevich, E. M. Oscillatory neurocomputers with dynamic connectivity. *Physical Review Letters* **82,** 2983 (1999).

16. Mallada, E. & Tang, A. Synchronization of weakly coupled oscillators: coupling, delay and topology. *Journal of Physics A: Mathematical and Theoretical* **46,** 505101 (2013).

17. Acebrón, J. A., Bonilla, L. L., Vicente, C. J. P., Ritort, F. & Spigler, R. The Kuramoto model: A simple paradigm for synchronization phenomena. *Reviews of modern physics* **77,** 137 (2005).

18. Van Der Pol, B. The Nonlinear Theory of Electric Oscillations. *Proceedings of the Institute of Radio Engineers* **22,** 1051–1086 (1934).

19. Kopell, N. & Somers, D. Anti-phase solutions in relaxation oscillators coupled through excitatory interactions. en. *Journal of Mathematical Biology* **33,** 261–280 (Dec. 1995).

20. Storti, D. & Rand, R. Dynamics of two strongly coupled van der Pol oscillators. *International Journal of Non-Linear Mechanics* **17,** 143–152 (1982).

21. Kouda, A & Mori, S. Mode analysis of a system of mutually coupled van der Pol oscillators with coupling delay. *International Journal of Non-Linear Mechanics* **17,** 267–276 (1982).

22. Chakraborty, T. & Rand, R. H. The transition from phase locking to drift in a system of two weakly coupled van der Pol oscillators. *International Journal of Non-Linear Mechanics* **23,** 369–376 (1988).

23. Ermentrout, G. Stable Periodic Solutions to Discrete and Continuum Arrays of Weakly Coupled Nonlinear Oscillators. *SIAM Journal on Applied Mathematics* **52,** 1665–1687 (Dec. 1992).

24. Izhikevich, E. Weakly pulse-coupled oscillators, FM interactions, synchronization, and oscillatory associative memory. *IEEE Transactions on Neural Networks* **10,** 508–526 (May 1999).

25. Mirollo, R. & Strogatz, S. Synchronization of Pulse-Coupled Biological Oscillators. *SIAM Journal on Applied Mathematics* **50,** 1645–1662 (Dec. 1990).

26. Adler, R. A Study of Locking Phenomena in Oscillators. *Proceedings of the IRE* **34,** 351–357 (1946).

27. Razavi, B. A study of injection locking and pulling in oscillators. *IEEE Journal of Solid-State Circuits* **39,** 1415–1424 (2004).

28. Saito, T. On a coupled relaxation oscillator. *IEEE Transactions on Circuits and Systems* **35,** 1147–1155 (1988).

29. Hu, C.-L. Self-sustained oscillation in an Rh-C or Rh-L circuit containing a hysteresis resistor Rh. *IEEE Transactions on Circuits and Systems* **33,** 636–641 (1986).

30. Yogendra, K., Fan, D. & Roy, K. Coupled Spin Torque Nano Oscillators for Low Power Neural Computation. *IEEE Transactions on Magnetics* **51,** 1–9 (Oct. 2015).

31. Sengupta, A., Panda, P., Wijesinghe, P., Kim, Y. & Roy, K. Magnetic Tunnel Junction Mimics Stochastic Cortical Spiking Neurons. en. *Scientific Reports* **6,** srep30039 (July 2016).

32. Kaka, S. *et al.* Mutual phase-locking of microwave spin torque nano-oscillators. *Nature* **437,** 389–392 (Sept. 2005).

33. Maleki, L. Sources: The optoelectronic oscillator. *Nature Photonics* **5,** 728–730 (2011).

34. Vitale, W. A., Moldovan, C. F., Paone, A., Schüler, A. & Ionescu, A. M. Fabrication of CMOS-compatible abrupt electronic switches based on vanadium dioxide. *Microelectronic Engineering. Micro/Nano Devices and Systems 2014 An open focused special thematic issue of Microelectronic Engineering* **145,** 117–119 (Sept. 2015).

35. Kim, H.-T. *et al.* Mechanism and observation of Mott transition in VO_2-based two- and three-terminal devices. en. *New Journal of Physics* **6,** 52 (2004).

36. Li, C., Wasige, E., Wang, L., Wang, J. & Romeira, B. 28 GHz MMIC resonant tunnelling diode oscillator of around 1mW output power. *Electronics Letters* **49,** 816–818 (June 2013).

37. Feiginov, M., Sydlo, C., Cojocari, O. & Meissner, P. Resonant-tunnelling-diode oscillators operating at frequencies above 1.1 THz. *Applied Physics Letters* **99,** 233506 (2011).

38. Suzuki, S., Asada, M., Teranishi, A., Sugiyama, H. & Yokoyama, H. Fundamental oscillation of resonant tunneling diodes above 1 THz at room temperature. *Applied Physics Letters* **97,** 242102 (2010).

39. Eisele, H. State of the art and future of electronic sources at terahertz frequencies. *Electronics Letters* **46,** S8 (2010).

40. Silva, T. & Rippard, W. Developments in nano-oscillators based upon spin-transfer point-contact devices. *Journal of Magnetism and Magnetic Materials* **320,** 1260–1271 (Apr. 2008).

41. Pickett, M. D. & Williams, R. S. Sub-100 fJ and sub-nanosecond thermally driven threshold switching in niobium oxide crosspoint nanodevices. *Nanotechnology* **23,** 215202 (2012).

42. Sharma, A. *et al. Low-power, high-performance S-NDR oscillators for stereo (3D) vision using directly-coupled oscillator networks* in *VLSI Technology, 2016 IEEE Symposium on* (2016), 1–2.

43. Hoppensteadt, F. C. & Izhikevich, E. M. Pattern recognition via synchronization in phase-locked loop neural networks. *IEEE Transactions on Neural Networks* **11,** 734–738 (2000).

44. Levitan, S. *et al. Non-Boolean associative architectures based on nano-oscillators* in *2012 13th International Workshop on Cellular Nanoscale Networks and Their Applications (CNNA)* (Aug. 2012), 1–6.

45. Csaba, G. *et al. Spin torque oscillator models for applications in associative memories* in *2012 13th International Workshop on Cellular Nanoscale Networks and Their Applications (CNNA)* (Aug. 2012), 1–2.

46. Wu, J., Jiao, L., Li, R. & Chen, W. Clustering dynamics of nonlinear oscillator network: Application to graph coloring problem. *Physica D: Nonlinear Phenomena* **240,** 1972–1978 (Dec. 2011).

47. Wu, C. Graph coloring via synchronization of coupled oscillators. *IEEE Transactions on Circuits and Systems I: Fundamental Theory and Applications* **45,** 974–978 (1998).

48. Hopfield, J. J. Neural networks and physical systems with emergent collective computational abilities. en. *Proceedings of the National Academy of Sciences* **79,** 2554–2558 (Apr. 1982).

49. Hopfield, J. J. & Tank, D. W. "Neural" computation of decisions in optimization problems. en. *Biological Cybernetics* **52,** 141–152 (July 1985).

50. Chua, L. O. & Yang, L. Cellular neural networks: theory. *IEEE Transactions on Circuits and Systems* **35,** 1257–1272 (Oct. 1988).

51. Lucas, A. Ising formulations of many NP problems. *Interdisciplinary Physics* **2,** 5 (2014).

52. Wang, Z., Marandi, A., Wen, K., Byer, R. L. & Yamamoto, Y. Coherent Ising machine based on degenerate optical parametric oscillators. *Physical Review A* **88,** 063853 (Dec. 2013).

53. Ercsey-Ravasz, M. & Toroczkai, Z. Optimization hardness as transient chaos in an analog approach to constraint satisfaction. en. *Nature Physics* **7,** 966–970 (Dec. 2011).

54. Mostafa, H., Müller, L. K. & Indiveri, G. An event-based architecture for solving constraint satisfaction problems. en. *Nature Communications* **6,** 8941 (Dec. 2015).

55. Traversa, F. L., Ramella, C., Bonani, F. & Di Ventra, M. Memcomputing NP-complete problems in polynomial time using polynomial resources and collective states. en. *Science Advances* **1,** e1500031–e1500031 (July 2015).

56. Elser, V., Rankenburg, I. & Thibault, P. Searching with iterated maps. en. *Proceedings of the National Academy of Sciences* **104,** 418–423 (Jan. 2007).

57. Vichniac, G. Y. Simulating physics with cellular automata. *Physica D: Nonlinear Phenomena* **10,** 96–116 (Jan. 1984).

58. Toffoli, T. Cellular automata as an alternative to (rather than an approximation of) differential equations in modeling physics. *Physica D: Nonlinear Phenomena* **10,** 117–127 (Jan. 1984).

59. Toffoli, T. CAM: A high-performance cellular-automaton machine. *Physica D: Nonlinear Phenomena* **10,** 195–204 (Jan. 1984).

60. *Handbook on modelling for discrete optimization* (eds Appa, G., Pitsoulis, L. S. & Williams, H. P.) *International series in operations research & management science* **v. 88** (Springer, New York, 2006).

61. Kar, A. *et al.* Intrinsic electronic switching time in ultrathin epitaxial vanadium dioxide thin film. *Applied Physics Letters* **102,** – (2013).

62. Shukla, N. *et al. Pairwise coupled hybrid vanadium dioxide-MOSFET (HVFET) oscillators for non-boolean associative computing* in *2014 IEEE International Electron Devices Meeting* (Dec. 2014), 28.7.1–28.7.4.

63. Shukla, N. *et al.* Synchronized charge oscillations in correlated electron systems. *Scientific reports* **4** (2014).

64. Hu, C.-L. Self-sustained oscillation in an R_H - C or R_H - L circuit containing a hysteresis resistor R_H. *Circuits and Systems, IEEE Transactions on* **33,** 636–641 (1986).

65. Haykin, S. S. *Neural Networks and Learning Machines* (Prentice Hall, 2009).

66. Gerstner, W. & Kistler, W. M. *Spiking Neuron Models: Single Neurons, Populations, Plasticity* (Cambridge university press, 2002).

67. Buesing, L., Bill, J., Nessler, B. & Maass, W. Neural Dynamics as Sampling: A Model for Stochastic Computation in Recurrent Networks of Spiking Neurons. *PLOS Comput Biol* **7,** e1002211 (Nov. 2011).

68. Mehonic, A. & Kenyon, A. J. Emulating the electrical activity of the neuron using a silicon oxide RRAM cell. *Frontiers in neuroscience* **10** (2016).

69. Tuma, T., Pantazi, A., Le Gallo, M., Sebastian, A. & Eleftheriou, E. Stochastic phase-change neurons. *Nature nanotechnology* **11,** 693–699 (2016).

70. Pickett, M. D., Medeiros-Ribeiro, G. & Williams, R. S. A scalable neuristor built with Mott memristors. *Nature materials* **12,** 114–117 (2013).

71. Indiveri, G., Chicca, E. & Douglas, R. A VLSI array of low-power spiking neurons and bistable synapses with spike-timing dependent plasticity. *IEEE transactions on neural networks* **17,** 211–221 (2006).

72. Sengupta, A., Panda, P., Wijesinghe, P., Kim, Y. & Roy, K. Magnetic tunnel junction mimics stochastic cortical spiking neurons. *Scientific reports* **6,** 30039 (2016).

73. Jerry, M., Parihar, A., Grisafe, B., Raychowdhury, A. & Datta, S. *Ultra-low power probabilistic IMT neurons for stochastic sampling machines* in *Proc. Symp. VLSI Technology* (June 2017), T186–T187.

74. Parihar, A., Shukla, N., Datta, S. & Raychowdhury, A. Synchronization of pairwise-coupled, identical, relaxation oscillators based on metal-insulator phase transition devices: A model study. *Journal of Applied Physics* **117,** 054902 (Feb. 2015).

75. Kar, A. *et al.* Intrinsic Electronic Switching Time in Ultrathin Epitaxial Vanadium Dioxide Thin Film. *Applied Physics Letters* **102,** 072106 (2013).

76. Jerry, M., Shukla, N., Paik, H., Schlom, D. G. & Datta, S. *Dynamics of electrically driven sub-nanosecond switching in Vanadium dioxide* in *Silicon Nanoelectronics Workshop (SNW), 2016 IEEE* (2016), 26–27.

77. Cocker, T. *et al.* Phase diagram of the ultrafast photoinduced insulator-metal transition in vanadium dioxide. *Physical Review B* **85,** 155120 (2012).

78. Tonnelier, A. The McKean's Caricature of the Fitzhugh–Nagumo Model I. The Space-Clamped System. *SIAM Journal on Applied Mathematics* **63,** 459–484 (Jan. 2003).

79. McKean, H. P. Nagumo's Equation. *Advances in Mathematics* **4,** 209–223 (June 1970).

80. Jerry, M., Parihar, A., Raychowdhury, A. & Datta, S. *A random number generator based on insulator-to-metal electronic phase transitions* in *Device Research Conference (DRC), 2017 75th Annual* (2017), 1–2.

81. Zhang, K. *et al.* VO 2-Based Selection Device for Passive Resistive Random Access Memory Application. *IEEE Electron Device Letters* **37,** 978–981 (2016).

82. Ricciardi, L. M. & Sato, S. First-Passage-Time Density and Moments of the Ornstein-Uhlenbeck Process. *Journal of Applied Probability* **25,** 43–57 (1988).

83. Tashman, J. *et al.* Epitaxial growth of VO2 by periodic annealing. *Applied Physics Letters* **104,** 063104 (2014).

84. Saito, T. On a coupled relaxation oscillator. *Circuits and Systems, IEEE Transactions on* **35,** 1147–1155 (1988).

85. Datta, S., Shukla, N., Cotter, M., Parihar, A. & Raychowdhury, A. *Neuro Inspired Computing with Coupled Relaxation Oscillators* in *Proceedings of the The 51st Annual Design Automation Conference on Design Automation Conference* (2014), 1–6.

86. Ladd, L. A. & Paul, W. Optical and transport properties of high quality crystals of {V2O4} near the metallic transition temperature. *Solid State Communications* **7,** 425–428 (1969).

87. Freeman, E. *et al.* Nanoscale structural evolution of electrically driven insulator to metal transition in vanadium dioxide. *Applied Physics Letters* **103,** 263109 (2013).

88. Aspvall, B. & Gilbert, J. Graph Coloring Using Eigenvalue Decomposition. *SIAM Journal on Algebraic Discrete Methods* **5,** 526–538 (Dec. 1984).

89. Alon, N. & Kahale, N. A Spectral Technique for Coloring Random 3-Colorable Graphs. *SIAM Journal on Computing* **26,** 1733–1748 (Dec. 1997).

90. McSherry, F. *Spectral partitioning of random graphs* in *42nd IEEE Symposium on Foundations of Computer Science, 2001. Proceedings* (Oct. 2001), 529–537.

91. Horn, R. A. & Johnson, C. R. *Matrix Analysis* en (Cambridge University Press, Oct. 2012).

92. Davis, C. The rotation of eigenvectors by a perturbation. *Journal of Mathematical Analysis and Applications* **6,** 159–173 (1963).

93. Wolpert, D. H., Macready, W. G., *et al.* No free lunch theorems for optimization. *IEEE transactions on evolutionary computation* **1,** 67–82 (1997).

94. Culberson, J. & Gent, I. Frozen development in graph coloring. *Theoretical computer science* **265,** 227–264 (2001).

95. Mammen, D. L. & Hogg, T. A new look at the easy-hard-easy pattern of combinatorial search difficulty. *Journal of Artificial Intelligence Research* **7,** 47–66 (1997).

96. Vlasie, R. D. *Systematic generation of very hard cases for graph 3-colorability* in *Proceedings of 7th IEEE International Conference on Tools with Artificial Intelligence* (1995), 114–119.

97. Cheeseman, P. C., Kanefsky, B. & Taylor, W. M. *Where the really hard problems are.* in *IJCAI* **91** (1991), 331–337.

98. Brélaz, D. New methods to color the vertices of a graph. *Communications of the ACM* **22,** 251–256 (1979).

99. Johnson, D. S. & Trick, M. A. *Cliques, coloring, and satisfiability: second DIMACS implementation challenge, October 11-13, 1993* (American Mathematical Soc., 1996).

100. Garey, M. R. & Johnson, D. S. *Computers and Intractability: A Guide to the Theory of NP-Completeness* (W. H. Freeman & Co., New York, NY, USA, 1979).

101. Motwani, R. & Naor, J. S. On Exact and Approximate Cut Covers of Graphs (1994).

102. Schaeffer, S. E. Graph clustering. *Computer science review* **1,** 27–64 (2007).

103. Goemans, M. X. & Williamson, D. P. Improved approximation algorithms for maximum cut and satisfiability problems using semidefinite programming. *Journal of the ACM* **42,** 1115–1145 (1995).

104. Fiedler, M. Algebraic connectivity of graphs. eng. *Czechoslovak Mathematical Journal* **23,** 298–305 (1973).

105. Miller, K. S. On the Inverse of the Sum of Matrices. English. *Mathematics Magazine* **54,** pp. 67–72 (1981).